2007

Numerical analysis of heat transfer during jet impingement on curved surfaces

Cesar F. Hernandez-Ontiveros
University of South Florida

Numerical Analysis of Heat Transfer During Jet Impingement on Curved Surfaces

by

Cesar F. Hernandez-Ontiveros

A thesis submitted in partial fulfillment
of the requirements for the degree of
Master of Science in Mechanical Engineering
Department of Mechanical Engineering
College of Engineering
University of South Florida

Major Professor: Muhammad Mustafizur Rahman, Ph.D.
Frank Pyrtle III, Ph.D.
Autar Kaw, Ph.D.

Date of Approval:
March 30, 2007

Keywords: steady state, transient analysis, hemispherical plate, cylindrical plate, heat flux

Dedication

To

God

My Father and Mother

Without them this could not have been possible

To

My Advisor Professor Muhammad Mustafizur Rahman

Thank you for your immense patience and guidance

Acknowledgments

To

My Friends: Son H. Ho, Jorge C. Lallave, and Phaninder Injeti

for their help and support throughout this very long journey!

Table of Contents

List of Figures

List of Symbols

b	Plate thickness, r_o- r_i, R_o- R_i, [m]
d_n	Diameter of the nozzle [m]
F_o	Fourier number, α_f t/ d_n^2
g	Acceleration due to gravity [m/s^2]
h	Heat transfer coefficient [W/m^{2}K], $q_{int}/(T_{int}-T_j)$
h_{av}	Average heat transfer coefficient [W/m^{2}K], defined by Eqn.(14)
H_n	Distance of the nozzle from the point of impingement [m]
k	Thermal conductivity [W/m K]
Nu	Nusselt number, $(h \cdot d_n)/k_f$
Nu_{av}	Average Nusselt number for the entire surface, $(h_{av} \cdot d_n)/k_f$
Nu_{max}	Maximum Nusselt number for the entire surface, $(h_{max} \cdot d_n)/k_f$
n	Coordinate normal to the surface
p	Pressure [Pa]
Pr	Prandtl number, ν_f/α_f
q	Heat flux [W/m^2]
Q	Fluid flow rate [m^3/s]
r	Radial coordinate [m]
r_i	Inner radius of hemisphere [m]
r_o	Outer radius of hemisphere [m]

R	Radius of curvature [m]
Re	Reynolds number, $(V_J \cdot d_n)/\nu_f$
R_i	Inner radius of curvature of the plate [m]
R_o	Outer radius of curvature of the plate [m]
s	Coordinate along the arc length, $R_o \Phi$, $r_o \Phi$ [m]
T	Temperature [K]
T_o	Constant Temperature at the inner surface of hemisphere (isothermal case) [K]
t	Time [s]
V_J	Jet velocity [m/s]
$V_{r, z}$	Velocity component in the r, z-direction [m/s]
$V_{x, y}$	Velocity component in the x, y-direction [m/s]
x	coordinate along x-axis [m]
y	coordinate along y-axis [m]
z	Axial coordinate [m]

Greek Symbols:

α	Thermal diffusivity [m^2/s]
β	Dimensionless nozzle to target spacing, H_n/d_n
δ	Liquid film thickness [m]
ν	Kinematic viscosity [m^2/s]
θ	Angular coordinate [rad]
Θ	Dimensionless temperature (constant heat flux boundary condition), $2 \cdot k_f \cdot (T_{int} - T_J)/ (q \cdot d_n)$

Φ Angular coordinate for curved plate [rad]

Φ Azimuthal coordinate for hemisphere [rad]

ρ Density [kg/m^3]

σ Surface tension [N/m]

Ω Dimensionless temperature (isothermal boundary condition), $(T_{int}-T_J)/ (T_o-T_J)$

Subscripts:

atm Ambient

av Average

f Fluid

i Initial Condition

int Solid-fluid Interface

j Jet or inlet

max Maximum

n Nozzle

s solid

SS Steady State

w Inner surface of hemisphere

Numerical Analysis of Heat Transfer During Jet Impingement on Curved Surfaces

Cesar F. Hernandez-Ontiveros

ABSTRACT

The flow structure and convective heat transfer behavior of a free liquid jet ejecting from a round nozzle impinging vertically on a hemispherical solid plate and a slot nozzle impinging vertically on a cylindrical curved plate have been studied using a numerical analysis approach. The simulation model incorporated the entire fluid region and the solid hemisphere or curved plate.

Solution was done for both isothermal and constant heat flux boundary conditions at the inner surface of the hemispherical plate and the constant heat flux boundary condition at the inner surface of the cylindrical shaped plate. Computations for the round nozzle impinging jet on the hemispherical plate and cylindrical plate were done for jet Reynolds number (Re_J) ranging from 500 to 2000, dimensionless nozzle to target spacing ratio (β) from 0.75 to 3, and for various dimensionless plate thicknesses to diameter nozzle ratio (b/d_n) from 0.083-1.5. Also, computations for the slot nozzle impinging jet on the cylindrical plate were done for inner plate radius of curvature to nozzle diameter ratio (R_i/d_n) of 4.16-16.66, plate thickness to nozzle diameter ratio (b/d_n) of 0.08-1.0, and different nozzle diameters (d_n), Results are presented for dimensionless solid-fluid interface temperature, dimensionless maximum temperature in the solid,

local and average Nusselt numbers using the following fluids: water (H_2O), flouroinert (FC-77), and oil (MIL-7808) and the following solid materials: aluminum, copper, Constantan, silver, and silicon.

Materials with higher thermal conductivity maintained a more uniform temperature distribution at the solid-fluid interface. A higher Reynolds number increased the Nusselt number over the entire solid-fluid interface. Local and average Nusselt number and heat transfer coefficient distributions showed a strong dependence on the impingement velocity or Reynolds number. As the velocity increases, the local Nusselt number increases over the entire solid-fluid interface. Decreasing the nozzle to target spacing favors the increasing of the Nusselt number. Increasing the nozzle diameter decreases the temperature at the curved plate outer surface and increases the local Nusselt number. Similarly, local and average Nusselt number was enhanced by decreasing plate thickness. Numerical simulation results are validated by comparing with experimental measurements and related correlations.

Chapter 1 Introduction

The implementation of jet impingement due to its high convective heat transfer rate in mechanical and chemical processes has led to many industry applications. These include cooling and heating of metal plates, cleaning of iced aircraft wings, cooling of turbine blades, drying of wetted surfaces, cleaning of industrial equipment, and cooling of electrical equipment. The advantage of using jets translates into reduced operational cost by improving the cooling efficiency of the system or equipment and reduces early failure of it. Thus, the need for heating/cooling processes able to transfer or remove very high heat fluxes appeals to liquid jet impingement as a choice. Enhancement of such heating/cooling processes will require information on the effects of jet velocity, thermo-physical properties of fluid and solid, thickness of the solid, and height from nozzle to impingement surface. Free-surface jets are created when a liquid discharges into ambient air or other type of gaseous environment [1]. The free surface, then, begins to form instantly at the nozzle exit and remains throughout the impingement section and wall region as the fluid moves downstream along the plate after impingement. The structure of the free surface depends on surface tension, gravitational and pressure forces.

1.1 Literature Review

1.1.1 Round Jet Impingement

An early investigation involving liquid jet impingement using round nozzles was carried out by Stevens and Webb [2] who considered an axisymmetric, single-phase liquid jet impinging on a flat uniformly heated surface. This experimental study investigated the effects of Reynolds number, nozzle to plate spacing, and jet diameter. Garimella and Rice [3] experimentally measured the local heat transfer from a small heat source to a normally impinging, axisymmetric and submerged liquid (FC-77) jet from a round nozzle for a range of Reynolds number of 4,000-23,000 and nozzle to heat source spacing ratios of 1 to 14. They concluded that secondary peaks in the local heat transfer coefficient resulted form increasing nozzle diameters for a given Reynolds number. Gomi and Webb [4] performed an investigation on heat transfer from a vertical heated surface to an obliquely impinging circular free-surface jet of transformer oil for various Reynolds number (235-1,746) with jet angles from 45° to 90°. They concluded that the maximum heat transfer coefficient was found to decrease with increasing jet inclination. Lee et al. [5] studied heat transfer from a convex surface with low curvature using liquid crystals to measure the local surface temperature at Reynolds numbers ranging from 11,000-50,000. The experimental study concluded that the stagnation point Nusselt number increases with increasing surface curvature. Kornblum and Goldstein [6] analyzed the flow of circular jets impinging on semicylindrical surfaces (convex and concave) for relatively small jet to semicylindrical diameter ratios ranging

from 0.0197-0.0394 using a flow visualization technique. Lee et al. [7] employed an apparatus consisting of various components (heat exchanger, flow meter, and air blower) to target a convex hemispherical surface for Re=11,000-87,000 at different dimensionless nozzle-to-surface distance and at constant hemisphere-to-nozzle diameter ratio to obtain information on the stagnation and local Nusselt numbers. Tong [8] numerically studied convective heat transfer of a circular liquid jet impinging onto a substrate to understand the hydrodynamics and heat transfer of the impingement process using the volume-of-fluid method to track the free surface of the jet.

Cornaro et al. [9] visualized fluid flow using a smoke-wire technique on concave and convex surfaces to examine the effects of curvature, nozzle to surface distance, and Reynolds number. The convex surface was examined for jet diameters of 0.0472, 0.0726, and 0.0986 m with Reynolds numbers ranging from 6,000-15,000. In addition, Cornaro et al. [10] showed the effect of increasing Reynolds number on the local Nusselt number for different types of curvature. Fleischer et al. [11] used a smoke-wire flow visualization technique to investigate the behavior of a round jet impinging on a convex surface. They showed the initiation and development of ring vortices and their interaction with the cylindrical surface. The effects of Reynolds number, jet to surface distance, and relative curvature were studied. Baonga et al. [12] experimentally studied the hydrodynamic and thermal characteristics of a free round liquid jet impinging into a heated disk for nozzle to plate spacing of 3-12 times nozzle diameter and for Reynolds number of 600-9,000.

1.1.2 Slot Jet Impingement

A number of past studies have considered liquid jet impingement from a two-dimensional slot nozzle to a heated flat plate. One of the early investigations on jet impingement on a flat plate was conducted by Inada et al. [13] who studied laminar flow between a plane surface and a two-dimensional water jet with constant heat flux using the Runge-Kutta method to obtain solutions for the boundary layer momentum and energy equations. Similar analytical solution to the momentum equation using the first order Cauchy-Euler ordinary differential equation and the integral equation approach to solve for the energy equation was employed by Carper [14]. He attempted to obtain a solution for the ratio of thermal to hydrodynamic boundary layer thickness for a certain range of combinations of jet Prandtl number and jet Reynolds number for an axisymmetric liquid jet impinging on a flat surface. Also, Liu and Lienhard [15] analytically and experimentally investigated convective heat transfer to an impinging liquid jet from a heated flat surface kept at a uniform heat flux. Solutions to the thermal boundary layer and film thickness were approximated using the integral method to obtain information about the local Nusselt number and temperature distribution. They concluded that the average Nusselt number for a constant heat flux is larger than for a constant wall temperature. Also, the average Nusselt number for a plane jet is generally larger than that for an axisymmetric jet. Wadsworth and Mudawar [16] performed an experiment to investigate single phase heat transfer from a smooth simulated chip to a two-dimensional jet of dielectric liquid FC-72 delivered from a very thin rectangular slot jet into a

channel confined between the chip surface and nozzle plate. The experiment studied the effects of jet width, confinement channel height, and impingement velocity for Reynolds number ranging from 1,000-100,000. Gau and Chung [17] reported heat transfer for air jet impingement on semicylindrical curved surfaces at low and high Reynolds numbers (6,000-35,000) by varying slot widths to surface diameter ratios (0.022-0.125) using smoke particles as means to visualize the air flow. The authors observed rotating vortices at the stagnation line on the convex surface which increased the heat transfer characteristics of the flow. Stevens and Webb [18] experimentally characterized the flow structure under an impinging liquid jet hitting a flat surface. However, their research only focused in measuring the velocity of the free surface of the jet. To achieve it, they used a novel laser-Doppler velocimetry technique to capture the fluctuations of the free surface for Reynolds numbers ranging from 16,000 to 47,000.

Teuscher et al. [19] studied jet impingement cooling of an in-line array of discrete heat sources (fins of different configurations) by a submerged slot jet of FC-77. Experimental results of convective heat transfer were obtained for various slot widths (0.254-0.508 mm) and Reynolds number of 10-500. Ma et al. [20] measured heat transfer coefficients resulting from the impingement of transformer oil jet issuing from various slot widths for fluid Prandtl numbers of 200-270 and Reynolds number between 55 and 415. Bartoli and Faggiani [21] experimentally studied heat transfer form a circular cylinder to a slot jet of water at different Prandtl numbers for $3500 \leq Re \leq 20000$ for tests performed at different angles $0° \leq \theta \leq 180°$ in order to obtain the local and average Nusselt number. Slot

jet impingement involving heat transfer from circular cylinders using air as the cooling fluid was experimentally studied by McDaniel and Webb [22] for Reynolds numbers in the range 600-8000 varying cylinder diameter to jet width spacings of 0.66, 1 and 2, and for jet exit to nozzle width spacing from 1 to 11. Gori and Bossi [23] investigated heat transfer for the flow over the surface of a cylinder for Reynolds number (4000-20,000) and determined that the distance between the exit of the slot jet and the cylinder surface affects the local Nusselt number. Kayansayan and Küçüka [24] performed an experimental and numerical study of jet impingement cooling on a concave channel. The results of the experimental investigation concluded that for a range of Reynolds numbers from 200 to 11,000 and slot to surface spacing from 2.2 to 4.2 of the slot width the heat transfer rates at the surface of the concave channel are improved due to the curvature of the channel.

Rahman et al. [1] numerically studied the conjugate heat transfer during impingement of a confined liquid jet. By varying slot width, impingement height, and plate thickness for Reynolds number ranging from 445-1,545. Shi et al. [25] carried out a numerical study to examine the effects of Prandtl number (0.7-71), nozzle to target spacing (2-10) and Reynolds number ranging from 0.01-100 on heat transfer under a semi-confined laminar slot jet. Olsson et al. [26] simulated heat transfer from a slot air jet impinging on a cylinder at various Reynolds numbers ranging from 23,000-100,000 and varying jet to cylinder distances and cylinder curvatures. They stated that the flow characteristics and the heat

transfer distribution around cylinders are found to be dependent on the distance and the opening between the jets.

Chan et al. [27] employed a liquid crystal thermographic system to experimentally determine the effects of jet Reynolds number, dimensionless slot nozzle width to impingement surface distance ratio, and slot nozzle width to circumferential distance on the local heat transfer for an air impinging slot jet on a semi-circular convex surface. Chan et al. [28] measured the mean flow and turbulence of a turbulent air slot jet impinging on two different semi-circular convex surfaces at Reynolds number 12,000 using a hot-wire X-probe anemometer. Gori and Bossi [29] experimentally determined the optimal height in the jet cooling of an electrically heated circular cylinder for various Reynolds numbers measuring mean and local Nusselt numbers. Rahimi et al. [30] investigated an under-expanded jet impinging on a heated cylindrical surface varying the nozzle to surface spacing (3-10) for various Reynolds numbers. Yang and Hwang [31] carried out a numerical simulation of flow of a turbulent slot jet impinging on a semicylindrical convex surface for Reynolds number (6,000-20,000) of the inlet flow and by varying slot jet width to jet to surface distance ratio.

Chen et al. [32] performed a theoretical analysis to characterize heat transfer from horizontal surfaces to single phase free surface laminar slot jets using a heat flux condition for different working fluids and different nozzle sizes. Zuckerman and Lior [33] employed numerical models to understand the heat transfer behavior on circular cylinders cooled by radial slot jets. These models

attempted to simulate a cylinder exposed to a radial array of slot jets (2-8) for Reynolds number ranged from 5,000 to 80,000 and different target diameter to nozzle hydraulic diameter. They concluded that the highest average Nusselt number would occur when having a lower number of jets.

1.2 Overview of Literature

The literature mentioned above describes most studies to date on jet impingement over a curved or flat surface using air or liquid as the working fluid and most of them have considered the steady state condition only. A few attempted to obtain local heat transfer distribution of concave, convex, or flat surfaces taking into account the transient nature of the problem. Therefore, a through study of liquid jet impingement on a curved surface is needed as this is encountered in many industrial processes.

1.3 Thesis Aim

The present study attempts to carry out a comprehensive numerical investigation of steady and transient local conjugate heat transfer for laminar free surface jet impingement over a hollow hemisphere and a curved cylindrical shaped plate. Computations using water (H_2O), flouroinert (FC-77), oil (MIL-7808), and ammonia (NH_3) as working fluids were carried out for different flow configurations, plate configurations, and different plate materials. The computations were carried out using the finite element method using FIDAP version 8.6. software package focused in computational fluid dynamics (CFD) of

the FLUENT corporation. The finite element method (FEM) is used for finding approximate solution of complex partial differential equations (PDE) as well as of integral equations. The solution method uses a mesh domain (elements grid) to solve the differential equation completely by applying to each element a system of simultaneous equations. The system of equations is solved for unknown values using the techniques of linear algebra or non-linear numerical schemes, as appropriate, or rendering the PDE into an equivalent ordinary differential equation, which is then, solved using finite difference. This approach differs from the finite element method (FEM) such that it uses finite differences schemes (forward, backward, and central) to approximate derivatives, being the central difference the one that provides the more accurate approximation. Also, the finite difference method is an approximation to the differential equation whereas the finite element method is an approximation to its solution. One of the most attractive features of the FEM over the FDM is its ability to handle complex geometries and boundaries (moving boundaries) with relative ease. That is the reason why the FEM was chosen as the preferred method to solve for the mathematical model presented in this study.

Chapter 2 Mathematical Models and Computation

2.1 Hemispherical Model

The physical hemispherical model studied here is three-dimensional (3-D) by nature as depicted in Figure 2.1. However, the problem can be greatly simplified into an axisymmetric liquid jet model that impinges on the outer surface of a hollow hemisphere subjected to an isothermal or constant heat flux boundary condition at its inner surface. Thus, the free jet discharges from the round nozzle and impinges perpendicularly at the top center of the hemisphere while the hemisphere is dissipating heat from within. Figure 2.2 shows a 2-D cross-sectional view of the system including the origin and axes used to write the boundary conditions. The fluid is Newtonian and the flow is incompressible and axisymmetric.

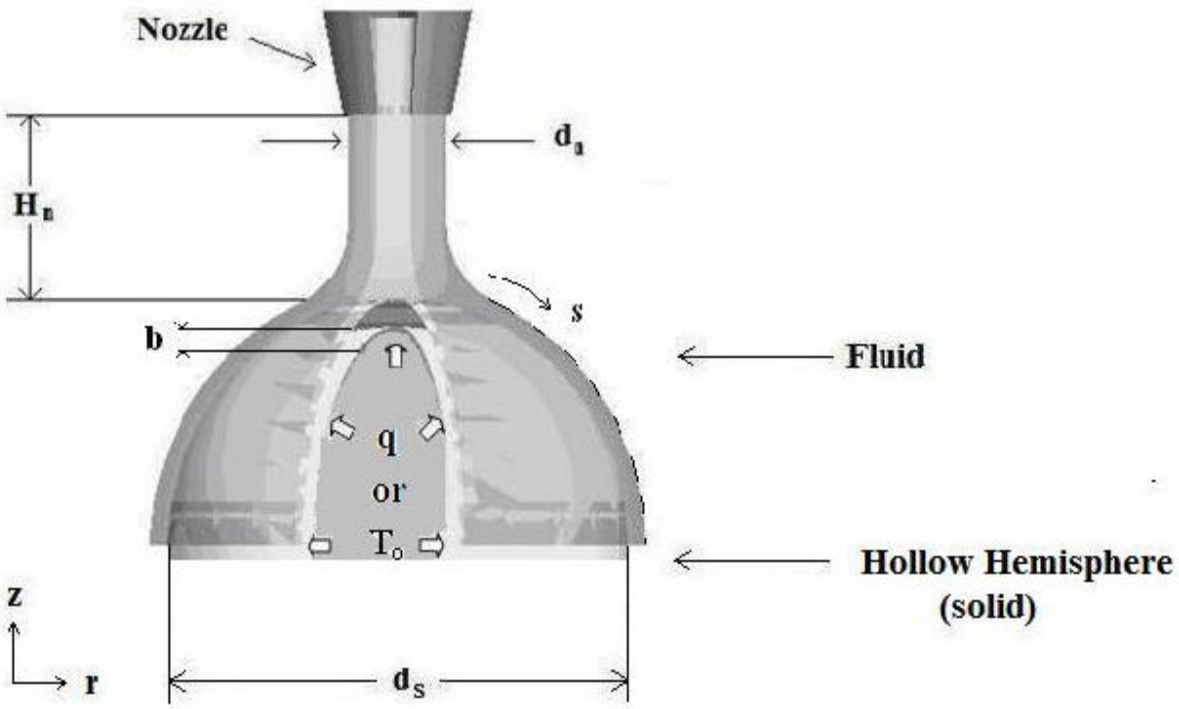

Figure 2.1 Three Dimensional Schematic of a Hollow Hemisphere During an Axisymmetric Liquid Jet Impingement

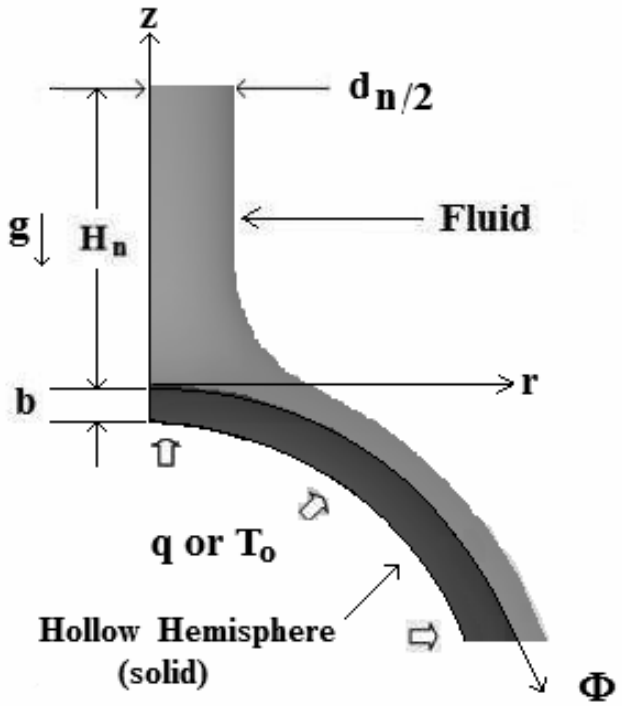

Figure 2.2 Cross-Sectional View of a Hollow Hemisphere During an Axisymetric Jet Impingement

2.1.1 Governing Equations: Steady State Heating

The equations describing the conservation of mass, momentum (r and z directions respectively), and energy can be written as [34]:

$$\nabla \cdot \vec{V} = 0 \tag{2.1.1}$$

$$\left(\vec{V} \cdot \nabla\right) V_r = -\frac{1}{\rho_f}\frac{\partial p}{\partial r} + v\left[\nabla^2 V_r - \frac{V_r}{r^2}\right] \tag{2.1.2}$$

$$\left(\vec{V} \cdot \nabla\right) V_z = -g - \frac{1}{\rho_f}\frac{\partial p}{\partial z} + v\nabla^2 V_z \tag{2.1.3}$$

$$\left(\vec{V} \cdot \nabla\right) T_f = \alpha_f \nabla^2 T_f \tag{2.1.4}$$

The conservation of energy inside the solid can be characterized by the following equation:

$$\nabla^2 T_s = 0 \tag{2.1.5}$$

2.1.2 Boundary Conditions: Steady State Heating

The following boundary conditions were used:

$$\text{At } r = 0,\ -b \le z \le 0 : \frac{\partial T_s}{\partial r} = 0 \tag{2.1.6}$$

$$\text{At } r = 0,\ 0 \le z \le H_n : V_r = 0, \frac{\partial V_Z}{\partial r} = 0, \frac{\partial T_f}{\partial r} = 0 \tag{2.1.7}$$

$$\text{At } r_i \le r \le r_o,\ z = -r_o : \frac{\partial T_S}{\partial z} = 0 \tag{2.1.8}$$

$$\text{At } r_o \le r \le (r_o + \delta),\ z = -r_o : p = p_{atm} \tag{2.1.9}$$

$$\text{At } z = H_n, 0 \le r \le \frac{d_n}{2} : V_Z = -V_J, V_r = 0, T_f = T_J \tag{2.1.10}$$

At inner surface of hemisphere:

$$0 \le \Phi \le \frac{\pi}{2} : -k_s \frac{\partial T_S}{\partial r} = q \quad \text{or} \quad T = T_o \tag{2.1.11}$$

At outer surface of hemisphere:

$$0 \le \Phi \le \frac{\pi}{2} : V_r = V_Z = 0, T_f = T_S, k_s \frac{\partial T_S}{\partial n} = k_f \frac{\partial T_f}{\partial n} \tag{2.1.12}$$

The boundary condition at the free surface $\left(\frac{d_n}{2} \le \Phi \le \frac{\pi}{2} \right)$ included the kinematic condition and balance of normal and shear stresses. The kinematic condition related velocity components to local slope of the free surface. The normal stress balance took into account the effects of surface tension. In the absence of any significant resistance from the ambient gas, the shear stress encountered at the free surface is essentially zero. Similarly, a negligible heat transfer at the free surface results in zero temperature gradient.

The local and average heat transfer coefficients can be defined as:

$$h = \frac{q}{(T_{int} - T_J)} \tag{2.1.13}$$

$$h_{av} = \frac{1}{(\overline{T}_{int} - T_J)} \int_0^{\frac{\pi}{2}} h(T_{int} - T_J) \cdot \sin\Phi d\Phi \tag{2.1.14}$$

where $\overline{T}_{int}$ is the average temperature at the solid-liquid interface. The local and average Nusselt numbers are calculated according to the following expressions.

$$Nu = \frac{h \cdot d_n}{k_f} \tag{2.1.15}$$

$$Nu_{av} = \frac{h_{av} \cdot d_n}{k_f} \tag{2.1.16}$$

2.1.3 Governing Equations: Transient Heating

A liquid jet axially discharging from a round nozzle impinges on the outer surface of a hollow hemisphere subjected to a constant heat flux boundary condition at its inner surface. At t=0 the power source is turned on and heat begins to flow only after an initially isothermal fluid flow has been established on the hemisphere. The fluid is Newtonian and the flow is incompressible and axisymmetric. Therefore, the equations describing the conservation of mass, momentum (r and z directions respectively), and energy [34]:

$$\nabla \cdot \vec{V} = 0 \tag{2.1.17}$$

$$\left(\vec{V} \cdot \nabla\right) V_r = -\frac{1}{\rho_f}\frac{\partial p}{\partial r} + \nu\left[\nabla^2 V_r - \frac{V_r}{r^2}\right] \tag{2.1.18}$$

$$\left(\vec{V} \cdot \nabla\right) V_z = -g - \frac{1}{\rho_f}\frac{\partial p}{\partial z} + \nu\nabla^2 V_z \tag{2.1.19}$$

$$\frac{\partial T_f}{\partial t} + \left(\vec{V} \cdot \nabla\right) T_f = \alpha_f \nabla^2 T_f \tag{2.1.20}$$

The conservation of energy inside the solid can be characterized by the following heat conduction equation:

$$\alpha\nabla^2 T_s = \frac{\partial T_s}{\partial t} \tag{2.1.21}$$

2.1.4 Boundary Conditions: Transient Heating

The following boundary conditions were used:

$$\text{At } r = 0,\ -b \le z \le 0 : \frac{\partial T_s}{\partial r} = 0 \tag{2.1.22}$$

$$\text{At } r = 0,\ 0 \le z \le H_n : V_r = 0, \frac{\partial V_Z}{\partial r} = 0, \frac{\partial T_f}{\partial r} = 0 \tag{2.1.23}$$

$$\text{At } r_i \le r \le r_o,\ z = -r_o \ : \ \frac{\partial T_S}{\partial z} = 0 \tag{2.1.24}$$

$$\text{At } r_o \le r \le (r_o + \delta),\ z = -r_o \ : \ p = p_{atm} \tag{2.1.25}$$

$$\text{At } z = H_n, 0 \le r \le \frac{d_n}{2} : V_Z = -V_J, V_r = 0, T_f = T_J \tag{2.1.26}$$

At inner surface of hemisphere:

$$0 \le \Phi \le \frac{\pi}{2} : -k_S \frac{\partial T_S}{\partial r} = q\ , t \ge 0 \tag{2.1.27}$$

At outer surface of hemisphere:

$$0 \le \Phi \le \frac{\pi}{2} : V_r = V_Z = 0, T_f = T_S, k_S \frac{\partial T_S}{\partial n} = k_f \frac{\partial T_f}{\partial n} \tag{2.1.28}$$

The plate was assumed to be at thermal equilibrium with jet fluid before the transient heating of the plate was turned on. The velocity field at this condition was determined by solving only the continuity and momentum equations in the fluid region. Thus,

At t = 0:

$$T_f = T_s = T_j\ , V_i = V_{r,\,z} \tag{2.1.29}$$

2.2 Cylindrical Plate Model

The physical model corresponds to a two-dimensional symmetric liquid jet that impinges on the outer surface of a curved hollow cylindrical shaped plate subjected to a uniform heat flux boundary condition at the inner surface as shown in Figure 2.3. The fluid is Newtonian and the flow is incompressible and symmetric about the mid-plane. Figure 2.3 also shows the origin and axes used to write the boundary conditions.

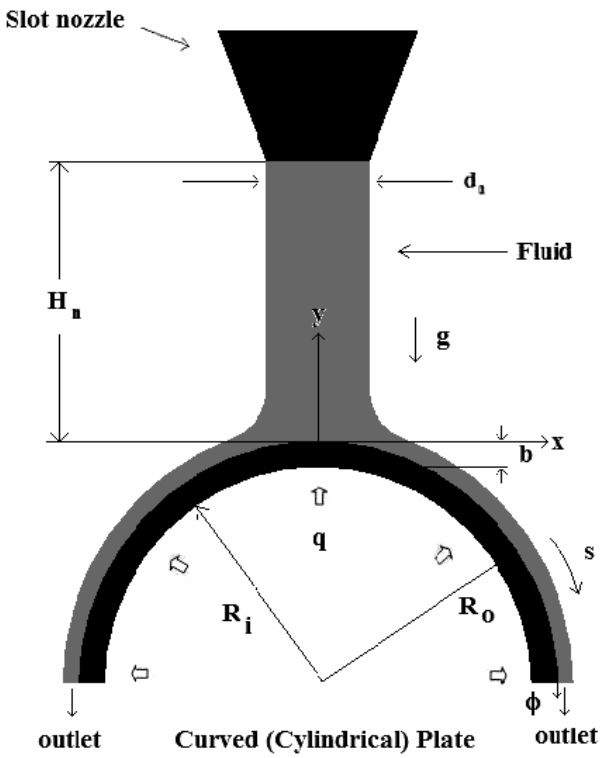

Figure 2.3 Schematic View of a Curved Plate During a 2-D Symmetric Liquid Jet Impingement

2.2.1 Governing Equations: Steady State Heating

The equations describing the conservation of mass, momentum (x and y directions respectively), and energy using a 2-D coordinate system can be written as [34]:

$$\nabla \cdot \vec{V} = 0 \tag{2.2.1}$$

$$\left(\vec{V} \cdot \nabla\right) \cdot V_y = -g_y - \frac{1}{\rho_f}\frac{\partial p}{\partial y} + \mu \nabla^2 V_y \tag{2.2.2}$$

$$\left(\vec{V} \cdot \nabla\right) \cdot V_x = -\frac{1}{\rho_f}\frac{\partial p}{\partial x} + \mu \nabla^2 V_x \tag{2.2.3}$$

$$\left(\vec{V} \cdot \nabla\right) \cdot T_f = \alpha_f \nabla^2 T_f \tag{2.2.4}$$

The conservation of energy inside the solid can be characterized by the following equation:

$$\nabla^2 T_s = 0 \tag{2.2.5}$$

2.2.2 Boundary Conditions: Steady State Heating

The following boundary conditions were used:

$$\text{At } x = 0,\ -b \le y \le 0 : \frac{\partial T_s}{\partial x} = 0 \tag{2.2.6}$$

$$\text{At } x = 0,\ 0 \le y \le H_n : V_x = 0, \frac{\partial V_y}{\partial x} = 0, \frac{\partial T_f}{\partial x} = 0 \tag{2.2.7}$$

$$\text{At } R_i \le x \le R_o,\ y = -x_o \ : \ \frac{\partial T_s}{\partial y} = 0 \tag{2.2.8}$$

$$\text{At } R_o \le x \le (R_o + \delta),\ y = -x_o : p = p_{atm} \tag{2.2.9}$$

$$\text{At } \; y = H_n, \; 0 \le x \le \frac{d_n}{2} : V_y = -V_J, V_x = 0, \; T_f = T_J \tag{2.2.10}$$

At inner surface of plate:

$$0 \le s \le R_i \phi_{max} : -k_s \frac{\partial T_s}{\partial n} = q \tag{2.2.11}$$

At outer surface of plate:

$$0 \le s \le R_o \phi_{max} : V_x = V_y = 0, T_s = T_f, k_s \frac{\partial T_s}{\partial n} = k_f \frac{\partial T_f}{\partial n} \tag{2.2.12}$$

The boundary condition at the free surface included the kinematic condition and balance of normal and shear stresses. The kinematic condition related velocity components to local slope of the free surface. The normal stress balance took into account the effects of surface tension. In the absence of any significant resistance from the ambient gas, the shear stress encountered at the free surface is essentially zero. Similarly, a negligible heat transfer at the free surface results in zero temperature gradient.

$$h = \frac{q}{(T_{int} - T_J)} \tag{2.2.13}$$

$$h_{av} = \frac{4}{\pi(\overline{T}_{int} - T_J)} \int_0^{\phi_{max}} h(T_{int} - T_J) \cdot \sin\phi d\phi \tag{2.2.14}$$

where $\overline{T}_{int}$ is the average temperature at the solid-liquid interface. The local and average Nusselt numbers are calculated according to the following expressions

$$Nu = \frac{h \cdot d_n}{k_f} \tag{2.2.15}$$

$$Nu_{av} = \frac{h_{av} \cdot d_n}{k_f} \tag{2.2.16}$$

2.2.3 Governing Equations: Transient Heating

The physical model corresponds to a two-dimensional symmetric liquid jet that impinges on the outer surface of a curved hollow cylindrical shaped plate subjected to a uniform heat flux boundary condition at the inner surface. At t=0 the power source is turned on and heat begins to flow only after an initially isothermal fluid flow has been established on the plate. The fluid is Newtonian and the flow is incompressible and symmetric about the mid-plane. The equations describing the conservation of mass, momentum, and energy in the fluid region can be written as [34]:

$$\nabla \cdot \vec{V} = 0 \tag{2.2.17}$$

$$\left(\vec{V} \cdot \nabla\right) \cdot V_y = -g_y - \frac{1}{\rho_f}\frac{\partial p}{\partial y} + \mu \nabla^2 V_y \tag{2.2.18}$$

$$\left(\vec{V} \cdot \nabla\right) \cdot V_x = -\frac{1}{\rho_f}\frac{\partial p}{\partial x} + \mu \nabla^2 V_x \tag{2.2.19}$$

$$\frac{\partial T_f}{\partial t} + \left(\vec{V} \cdot \nabla\right) \cdot T_f = \alpha_f \nabla^2 T_f \tag{2.2.20}$$

The conservation of energy inside the solid can be characterized by the following equation:

$$\alpha_s \nabla^2 T_s = \frac{\partial T_s}{\partial t} \tag{2.2.21}$$

2.2.4 Boundary Conditions: Transient Heating

The following boundary conditions were used:

$$\text{At } x = 0,\ -b \le y \le 0 : \frac{\partial T_s}{\partial x} = 0 \tag{2.2.22}$$

$$\text{At } x=0,\ 0\le y\le H_n : V_x=0, \frac{\partial V_y}{\partial x}=0, \frac{\partial T_f}{\partial x}=0 \tag{2.2.23}$$

$$\text{At } R_i \le x \le R_o,\ y=-x_o : \frac{\partial T_s}{\partial y}=0 \tag{2.2.24}$$

$$\text{At } R_o \le x \le (R_o+\delta),\ y=\text{-}x_o : p=p_{atm} \tag{2.2.25}$$

$$\text{At } y=H_n,\ 0\le x\le \frac{d_n}{2} : V_y=-V_J, V_x=0,\ T_f=T_J \tag{2.2.26}$$

At inner surface of plate:

$$0\le s\le R_i\phi_{max} : -k_s\frac{\partial T_s}{\partial n}=q,\ t\ge 0 \tag{2.2.27}$$

At outer surface of plate:

$$0\le s\le R_o\phi_{max} : V_x=V_y=0,\ T_s=T_f,\ k_s\frac{\partial T_s}{\partial n}=k_f\frac{\partial T_f}{\partial n} \tag{2.2.28}$$

The plate was assumed to be at thermal equilibrium with jet fluid before the transient heating of the plate was turned on. The velocity field at this condition was determined by solving only the continuity and momentum equations in the fluid region. Thus,

At t = 0:

$$T_f = T_s = T_j,\ V_i = V_{x,y} \tag{2.2.29}$$

2.3 Numerical Computation

2.3.1 Steady State Process

The governing equations in conjunction with the boundary conditions described above were solved using the Galerkin finite element method employed by FIDAP. Four node quadrilateral elements were used as shown in Figure 2.4.

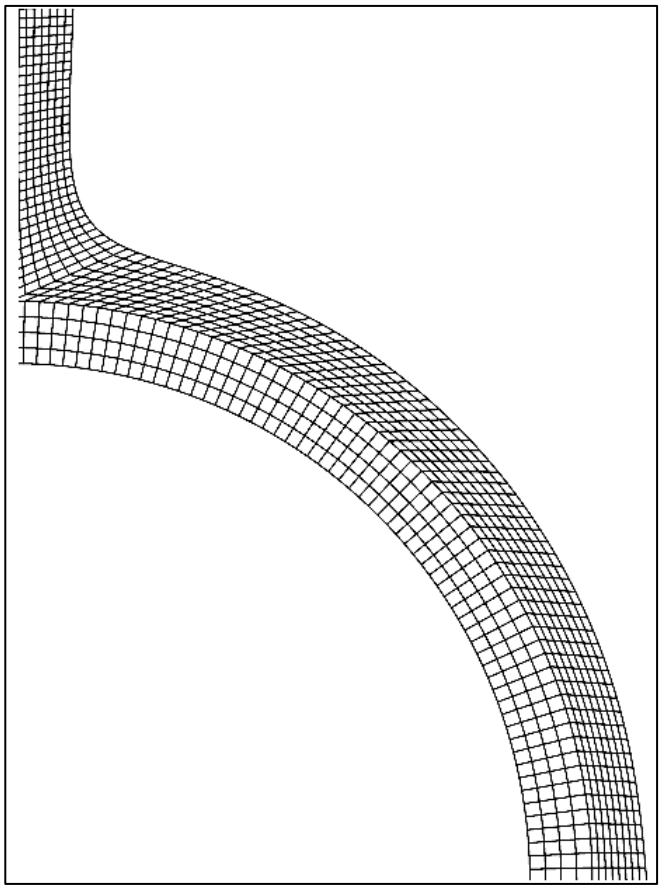

Figure 2.4 Mesh Plot of a Curved Plate During a 2-D Symmetric Liquid Jet Impingement

For every element, the velocity, pressure, and temperature fields were approximated until convergence was achieved. The method to solve the set of the resulting nonlinear equations was the Newton-Raphson algorithm due to its

coupled nature for two dimensional problems and its ability to solve all conservation equations in a simultaneous manner. The approach used to solve the free surface problem described here was to introduce a new degree of freedom representing the position of the free surface. This degree of freedom was introduced as a new unknown into the global system of equations. A scaled dense grid distribution was used to adequately capture large variations near the solid-fluid interface of the meshed domain. Due to non-linear nature of the governing transport equations, an iterative procedure was used to converge at the solution for the velocity and temperature fields. Since the solution of the momentum equation required only two out of the three boundary conditions at the free surface, the third condition was used to upgrade the position of the free surface at the end of each iteration step. The height of the free surface was adjusted after each iteration by satisfying the kinematic condition that relates the slope of the free surface to local velocity components at the free surface. The Newton-Raphson solver employed spines to track the free surface and re-arranged grid distribution with the movement along the free surface. The spines are straight lines passing through the free surface nodes and connect the remaining nodes underneath the free surface. The movement of the free surface affected only the nodes along the spine. The solution was considered converged when relative change in field values from a particular iteration to the next, and the sums of the residuals for each variable became less than 10^{-6}.

2.3.2 Transient Process

In order to determine the initial velocity field (V_i), the equations for the conservation of mass and momentum were solved. Once the initial free surface height distribution and the flowfield for the isothermal equilibrium condition were satisfied, the power of the heat source was turned on and heat began to flow. The computation domain included both solid and fluid regions, and continuity, momentum, and energy were solved simultaneously as a conjugate problem. The height of the free surface was adjusted after each iteration by satisfying the kinematic condition that relates the slope of the free surface to local velocity components at the free surface. The solution was considered converged when relative change in field values from a particular iteration to the next, and the sums of the residuals for each variable became less than 10^{-6}. The computation continued towards the steady state condition; however, because of large changes at the outset of the transient and very small changes when the solution approached the steady-state condition, a variable time step was used for the computation.

2.4 Mesh Independence and Time Step Study

2.4.1 Cylindrical Coordinates

Several grids or combinations of number of elements were used to determine the accuracy of the numerical solution as shown in Figure 2.5. The numerical solution becomes grid independent when the number of divisions equal to 40x119 in the axial (z) (radial in thin film after impingement) and arc (Φ) directions respectively is used. Numerical results for a 40x119 grid gave almost identical results compared to those using 34x79 and 40x87 grids. A quantitative difference in grid independence was calculated using the following expression:

$$T_{int} = C + \frac{D}{N^e} \tag{2.3.1}$$

C, D, and e are constants to be evaluated. N represents the number of divisions along a chosen axis. T_{int} is the solid-fluid interface temperature at a given Φ-location of the hemispherical plate. Thus, equation (2.3.1) has three unknowns at three sets of interface temperatures taken at three different grid sizes. This results in a set of non-linear equations with three variables. The value of e was obtained based on doing a particular number of iterations. At s or Φ=0.001276 m, the value of e was calculated to be 8.554. Once the value of e had been obtained, it was substituted into the system of equations and the values of C and D were calculated to be 318.9112 and 0.72205E19 respectively. In addition, the percentage error is calculated used the following expression:

$$\left|\frac{T_{int} - C}{C}\right| x100 \tag{2.3.2}$$

The error at Φ=0.001276 m was found to be 3.987% for 40x119 grids and 4.26% for 48x87 grids.

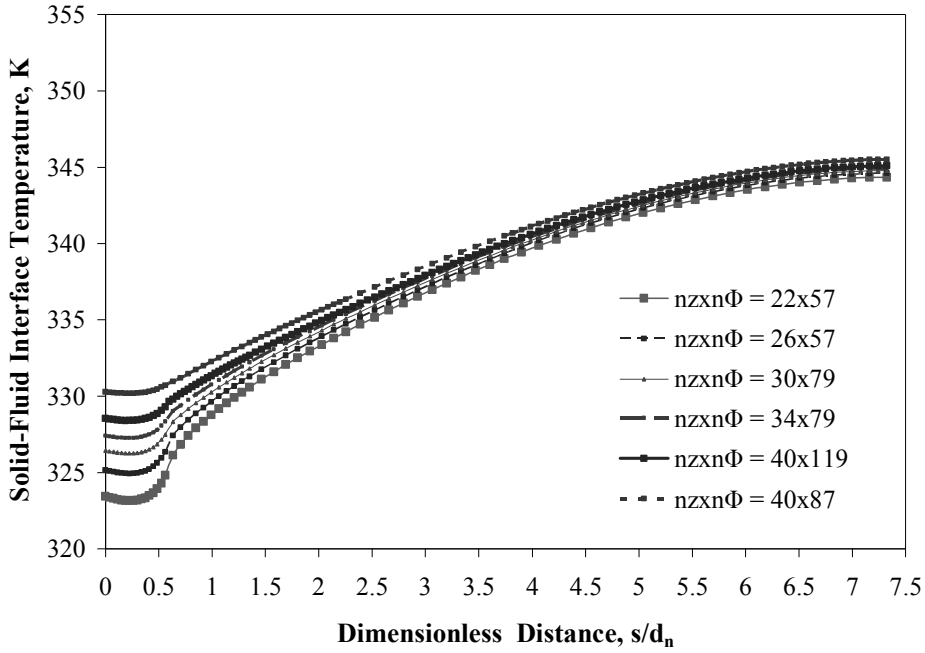

Figure 2.5 Local Dimensionless Interface Temperature for Different Number of Elements in z (or r) and Φ Directions for Water as Fluid and Silicon as Solid (Re=750, b/d_n=0.5, ß=2.0, q=250 kW/m^2)

Figure 2.6 plots the transient variation of the maximum dimensionless temperature encountered at the hemisphere's outer surface (solid-fluid interface) for different time increments as a function of time using the Fourier number (F_o) as a dimensionless number to represent time. Observe that the simulation is not very susceptible to the time increments chosen. However, a very small time increment (0.00001 s) ensures the initial condition to be revealed. For this numerical study, an appropriate time increment of 0.01 s was selected in order to accomplish a smooth variation. Notice how the maximum dimensionless

temperature increases rapidly as the time increases all the way to the steady-state condition.

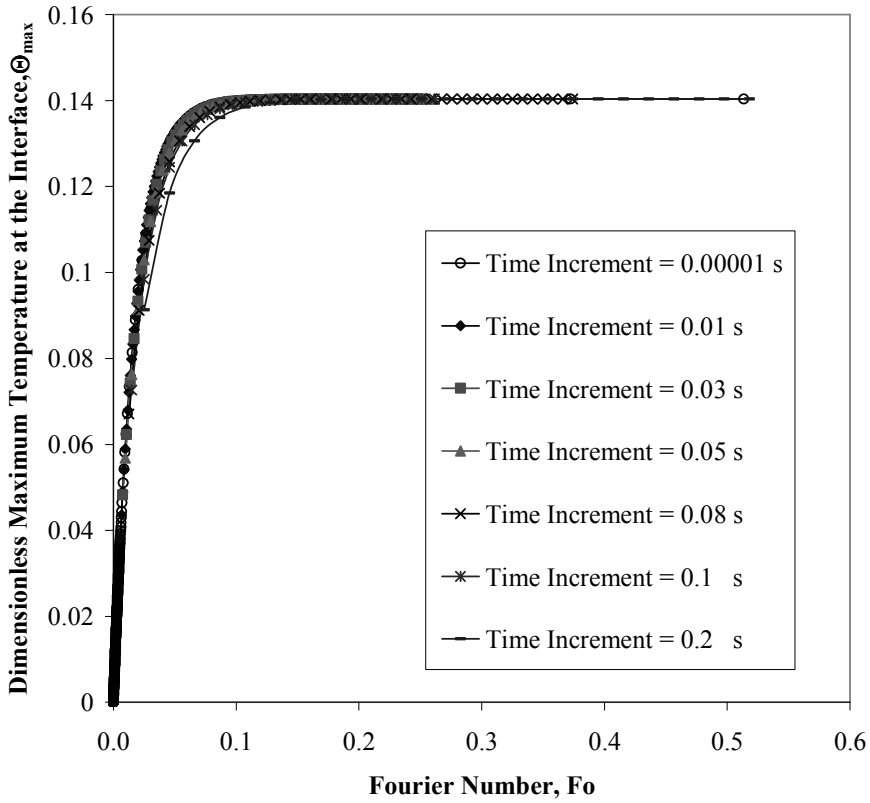

Figure 2.6 Solid-Fluid Interface Dimensionless Maximum Temperature Variation for Silicon Hemisphere at Different Time Increments (Re=750, b/d_n=0.5, ß=2.0, H_n = 0.30 cm, q=250 kW/m^2)

2.4.1 Cartesian Coordinates

Several grids or combinations of number of elements were used to determine the accuracy of the numerical solution as shown in Figure 2.7. The numerical solution becomes grid independent when the number of divisions equal to 30x132 in the y and x or ϕ (in thin film after impingement) directions is

used. Numerical results for a 30x132 grid gave almost identical results compared to those using 32x132 and 26x92 grids. The average difference was 0.0466%. Also, a quantitative difference in grid independence was carried on using equation (2.3.1). At s or ϕ=0.001277 m, the value of e was calculated to be 8.554. Once the value of e had been obtained, it was substituted into the system of equations and the values of C and D were calculated to be 338.2391 and -0.7070E19 respectively. The error percentage is calculated from equation (2.3.2) and found to be 1.51% for 32x132 grids and 1.63% for 26x92 grids at ϕ=0.001277 m.

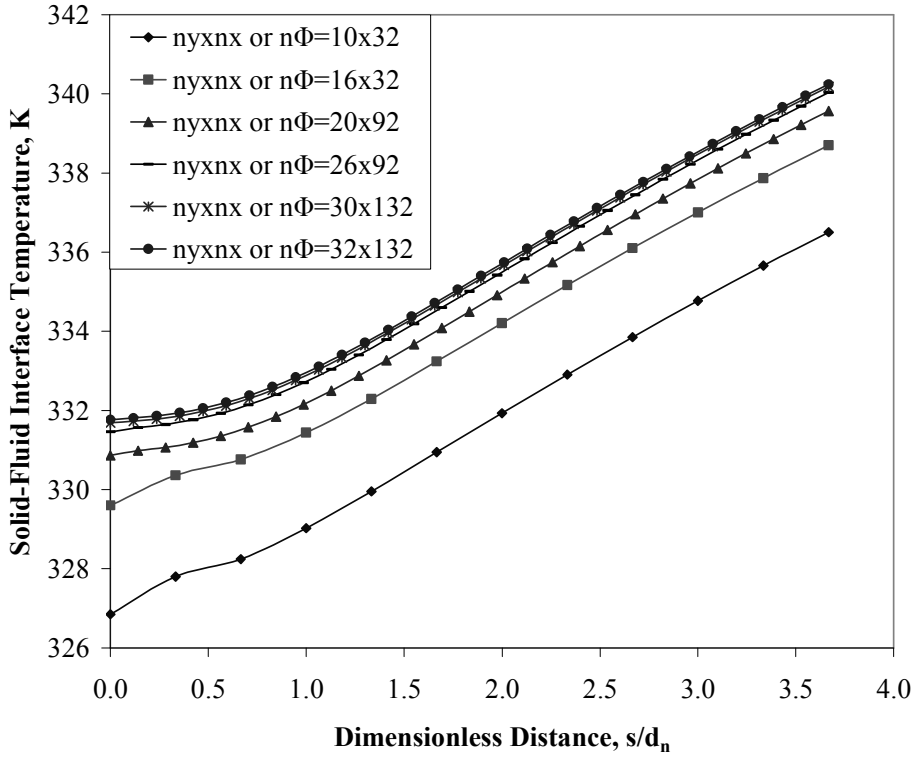

Figure 2.7 Local Dimensionless Interface Temperature for Different Number of Elements in x or ϕ, and y Directions (Re=750, ß=2.5, H_n = 0.30 cm)

Figure 2.8 shows the transient variation of the maximum dimensionless temperature found at the plate's outer surface (solid-fluid interface) for different time increments as a function of time using the Fourier number (F_o) as a dimensionless number to represent time. Note that the numerical simulation is not very susceptible to the time increments chosen. For this study, a time increment of 0.01 s was chosen in order to obtain a smooth variation for temperature. Notice how the maximum dimensionless temperature at the transient increases rapidly all the way to the steady-state condition.

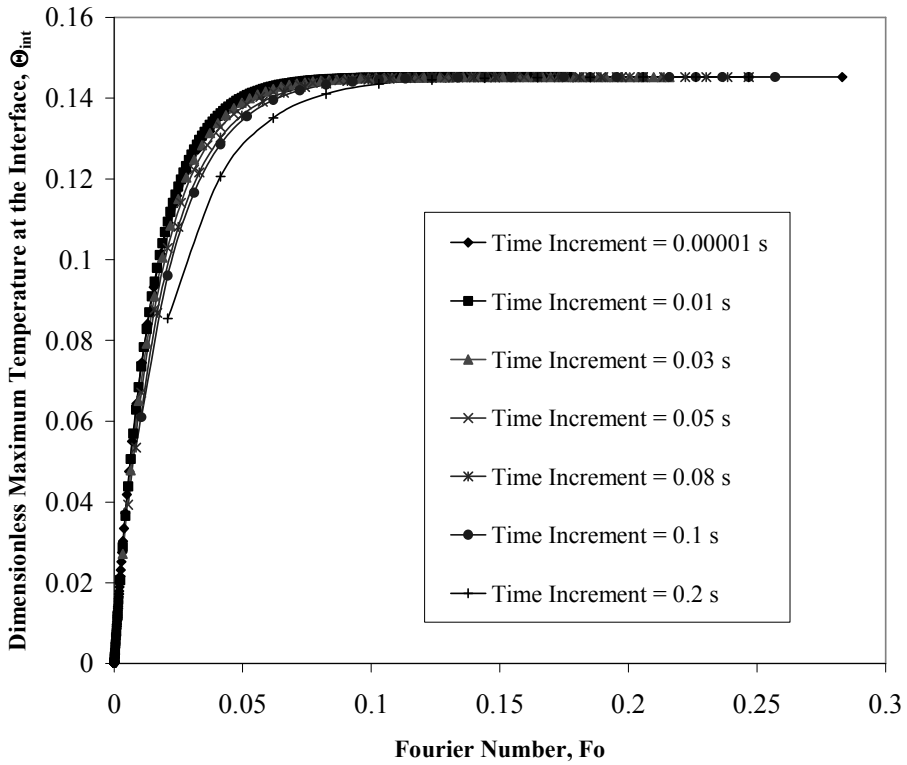

Figure 2.8 Solid-Fluid Interface Dimensionless Maximum Temperature Variation for Silicon Plate at Different Time Increments (Re=750, b/d_n=0.5, ß=2.5, H_n = 0.30 cm, q=250 kW/m^2)

Chapter 3 Hemispherical Model Results

3.1 Steady State Heating

A typical velocity vector distribution is shown in Figure 3.1. It can be observed that the velocity remains almost uniform at the potential core region of the jet. However, the velocity decreases and the fluid jet diameter increases as the fluid gets closer to the surface during the impingement process. The direction of motion of the fluid particles shifts along the angle of curvature, afterwards, the fluid accelerates creating a region of minimum sheet thickness. That is the beginning of the boundary layer zone. It can be noticed that as the fluid moves downstream along the convex surface, the boundary layer thickness increases and the frictional resistance from the wall is eventually transmitted to the entire film thickness where the fully viscous zone develops.

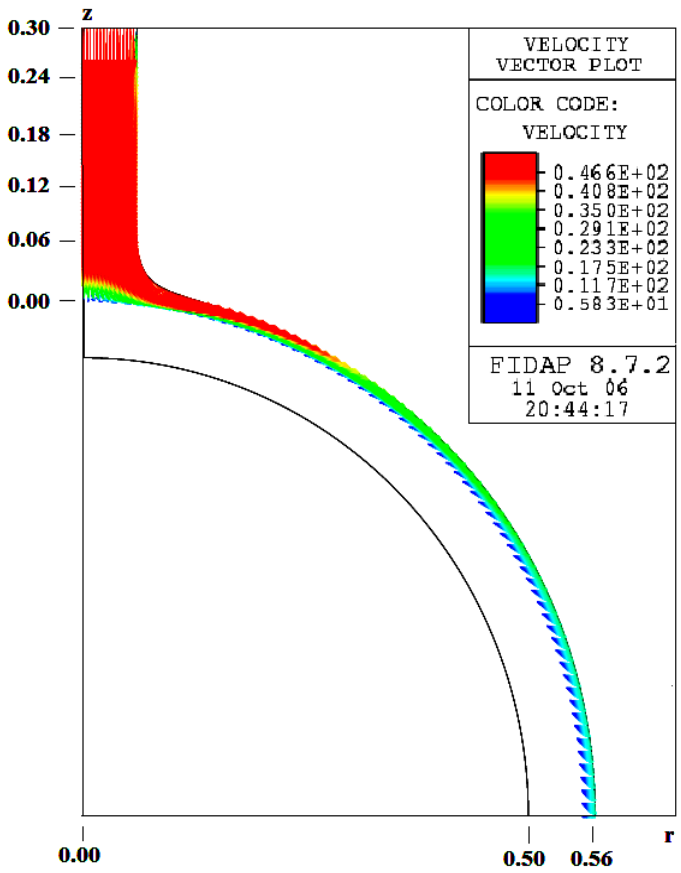

Figure 3.1 Velocity Vector Distribution for Silicon Hemisphere with Water as the Cooling Fluid (Re = 750, b = 0.60 mm, Q = 5.665×10^{-7} m^3/s, $\beta = 2.0$, $H_n = 0.30$ cm, q = 250 kW/m^2)

A pressure distribution plot is shown in Figure 3.2. As it is seen, the pressure at the impingement regions is higher due to the fluid impacting the hemisphere outer surface in comparison with the remaining portion of the hemisphere. A pressure gradient distribution is more uniform, however, along the arc length of the solid.

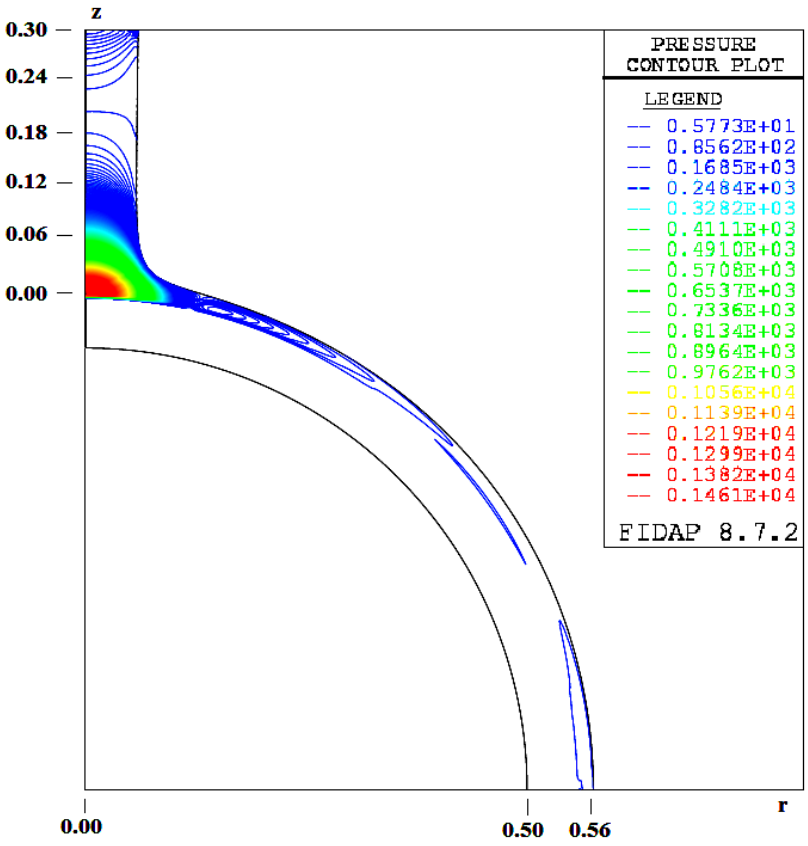

Figure 3.2 Pressure Distribution for Silicon Hemisphere with Water as the Cooling Fluid (Re = 750, b = 0.60 mm, Q = 5.665x10^{-7} m^3/s, β = 2.0, H_n = 0.30 cm, q = 250 kW/m^2)

Figure 3.3 depicts temperature distribution along the solid and fluid region. Higher temperatures are encountered along the end of the arc length of the solid-fluid interface whereas lower temperatures are encountered at the stagnation region. After impact has occurred, the particles start to accelerate towards the remaining portion of the hemisphere, hence, increasing the velocity boundary layer and temperature boundary layer thickness.

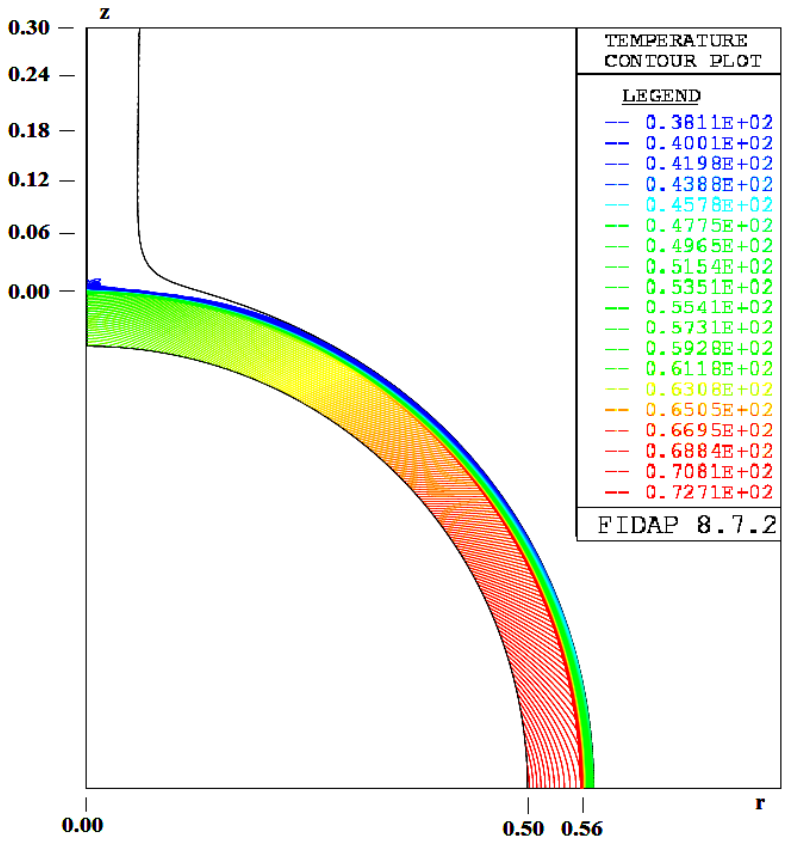

Figure 3.3 Temperature Distribution for Silicon Hemisphere with Water as the Cooling Fluid (Re = 750, b = 0.60 mm, Q = 5.665×10^{-7} m^3/s, $\beta = 2.0$, $H_n = 0.30$ cm, q = 250 kW/m^2)

Figure 3.4 shows the free surface height distribution for different Reynolds numbers when the jet strikes the hemisphere's surface. It can be seen that the fluid spreads out moving along the outer surface of the hemisphere. As the Reynolds number increases, the film diminishes in thickness due to a larger impingement velocity that translates to a higher fluid velocity in the film. For the conditions considered in the present investigation, the flow was supercritical and a hydraulic jump did not occur within the computation domain. These observations concur with the experimental work of Stevens and Webb [35] for free jet impingement on a flat surface. It was observed that the velocity remains

almost uniform at the potential core region of the jet. However, the velocity decreases and the fluid jet diameter increases as the fluid get closer to the surface during the impingement process. The direction of motion of the fluid particles shifted along the angle of curvature, afterwards, the fluid accelerated creating a region of minimum sheet thickness. That was the beginning of the boundary layer zone. It was noticed that as the fluid moves downstream along the convex surface, the boundary layer thickness increases and the frictional resistance from the wall is eventually transmitted to the entire film thickness where the fully viscous zone developed. The three different regions observed in the present investigation agreed with the experiments of Liu et al. [36] for jet impingement over a flat surface.

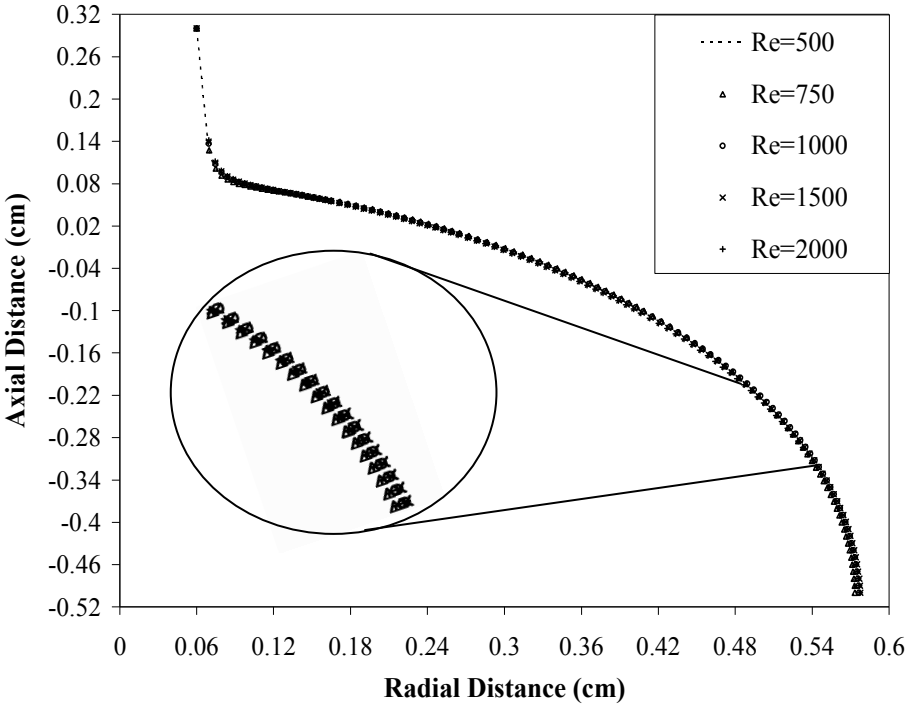

Figure 3.4 Free Surface Height Distribution for Different Reynolds Numbers and Water as the Cooling Fluid (b=0.60 mm, β=2.0, H_n=0.30 cm, q=250 kW/m^2)

Figures 3.5 and 3.6 show dimensionless interface temperature and local Nusselt number distributions as a function of dimensionless distance (s/d_n) along the solid-fluid interface at different Reynolds numbers under an isothermal heating condition. The curves in Figure 3.5 reveal that the dimensionless interface temperature decreases with jet velocity or (Reynolds number). The dimensionless interface temperature has the lowest value at $s/d_n = 0.4$ and increases along the arc length (s) reaching the highest value at the end of it. The local Nusselt number depicted in Figure 3.6 increases rapidly over a small distance (core region) measured from the stagnation point, reaching a maximum around $s/d_n = 0.5$, and then decreases along the radial distance as the boundary layer develops further downstream. The location of the maximum Nusselt number can be associated with the transition of the flow from the vertical impingement to horizontal displacement where the boundary layer starts to develop. Figures 3.5 and 3.6 confirm how an increasing Reynolds number contributes to a more effective cooling by the enhancement of convective heat transfer coefficient.

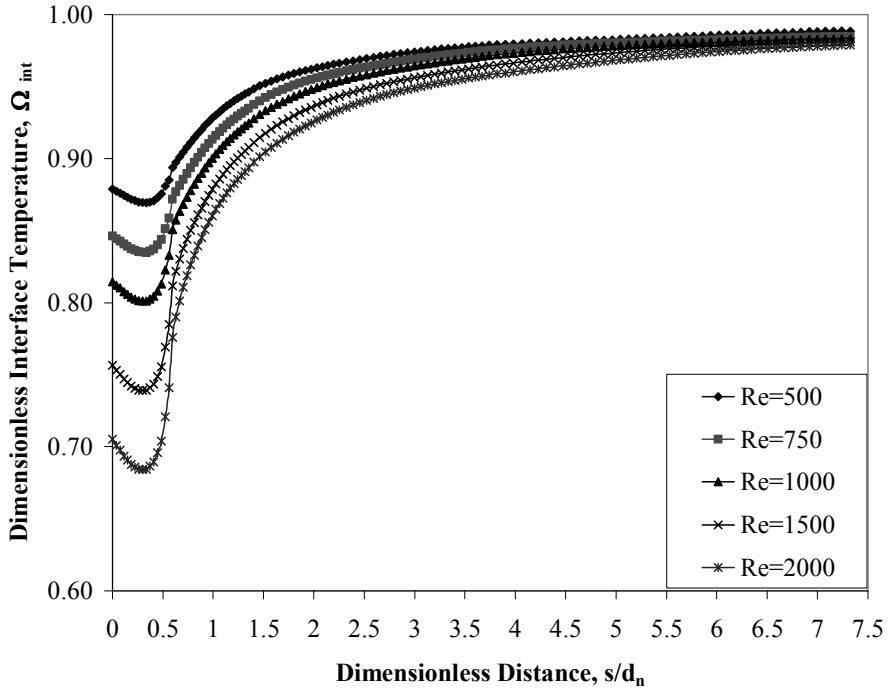

Figure 3.5 Dimensionless Interface Temperature Distribution for a Silicon Hemisphere at Different Reynolds Numbers, and Water as the Cooling Fluid (β=2.0, H_n= 0.30 cm, b=0.60 mm, T_o=373 K)

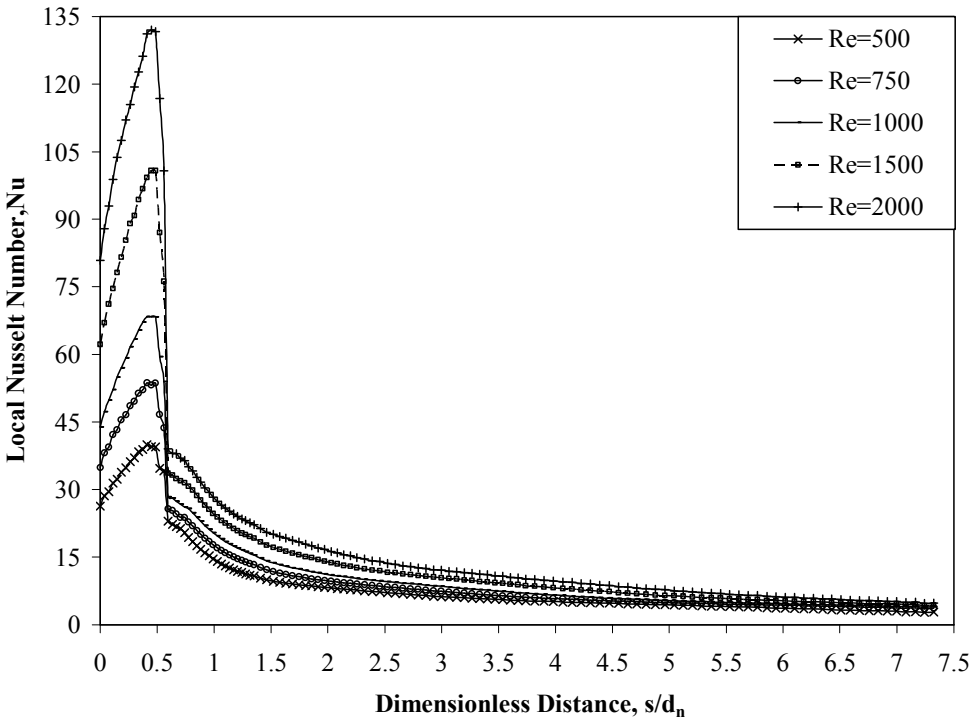

Figure 3.6 Local Nusselt Number Distribution for a Silicon Hemisphere at Different Reynolds Numbers, and Water as the Cooling Fluid (β=2.0, H_n=0.30 cm, b=0.60 mm, T_o=373 K)

Figures 3.7 and 3.8 show dimensionless interface temperature and local Nusselt number distributions as a function of dimensionless distance (s/d_n) along the solid-fluid interface at different Reynolds numbers under a constant heat flux condition. The curves in Figure 3.7 reveal that the dimensionless interface temperature decreases with jet velocity or (Reynolds number). The dimensionless interface temperature has the lowest value at the stagnation point (underneath the center of the axial opening) and increases along the arc length (s) reaching the highest value at the end of it.

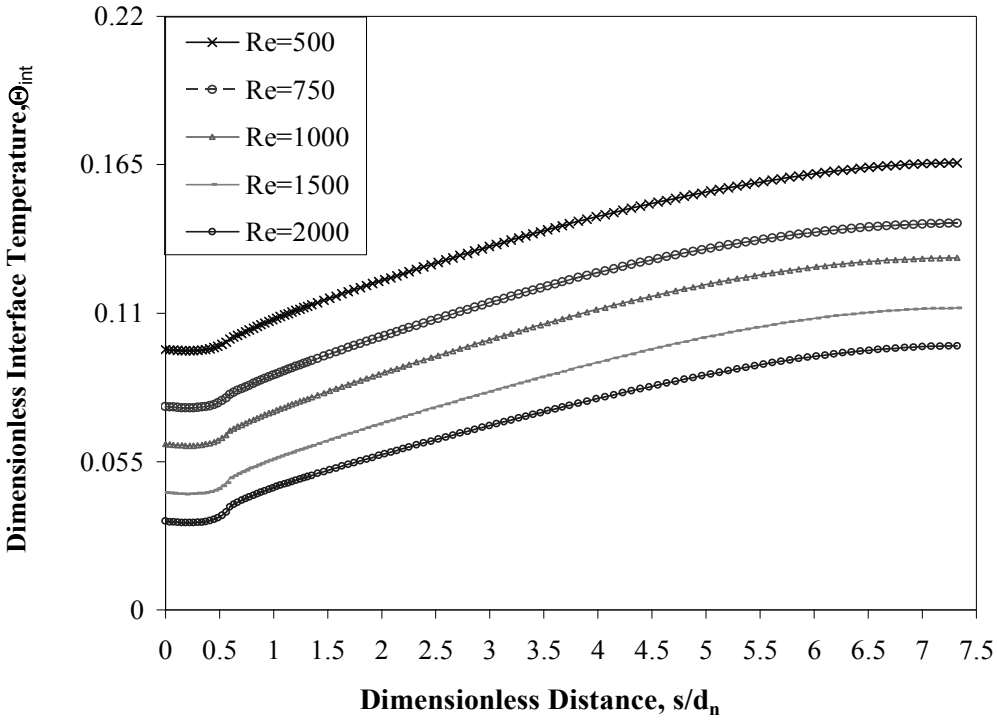

Figure 3.7 Dimensionless Interface Temperature Distribution for a Silicon Hemispherical Plate at Different Reynolds Numbers, and Water as the Cooling Fluid (β=2.0, H_n= 0.30 cm, b=0.60 mm, q=250 kW/m^2)

The local Nusselt number shows a very similar kind of distribution as the case where the bottom surface of the hemispherical plate is kept at an isothermal condition. The values are however different. This also shows that an increasing Reynolds number contributes to a more effective cooling by the enhancement of convective heat transfer coefficient.

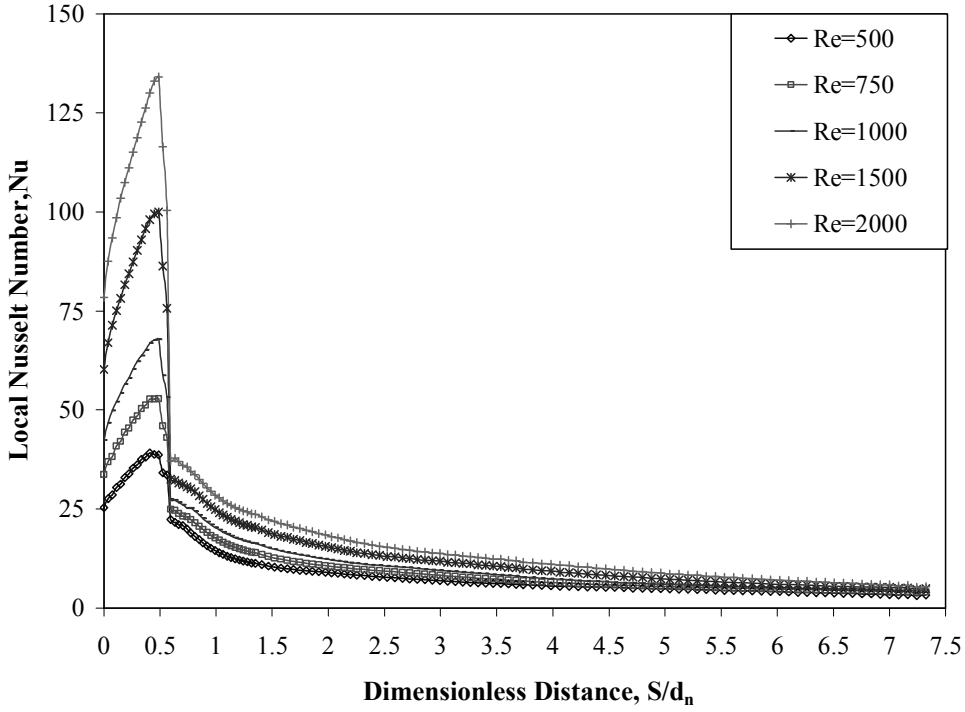

Figure 3.8 Local Nusselt Number Distribution for a Silicon plate at Different Reynolds Numbers, and Water as the Cooling Fluid (β =2.0 , H_n = 0.30 cm, b=0.60 mm, q=250 kW/m^2)

Figure 3.9 plots the average Nusselt number and average heat transfer coefficient as a function of Reynolds number. It may be noted that average Nusselt number increases with Reynolds number. As the flow rate (or Reynolds number) increases, the magnitude of fluid velocity near the solid-fluid interface that controls the convective heat transfer rate increases. It may be also noted

that effects of boundary condition is more at lower Reynolds number and the curves come closer as the Reynolds number increases.

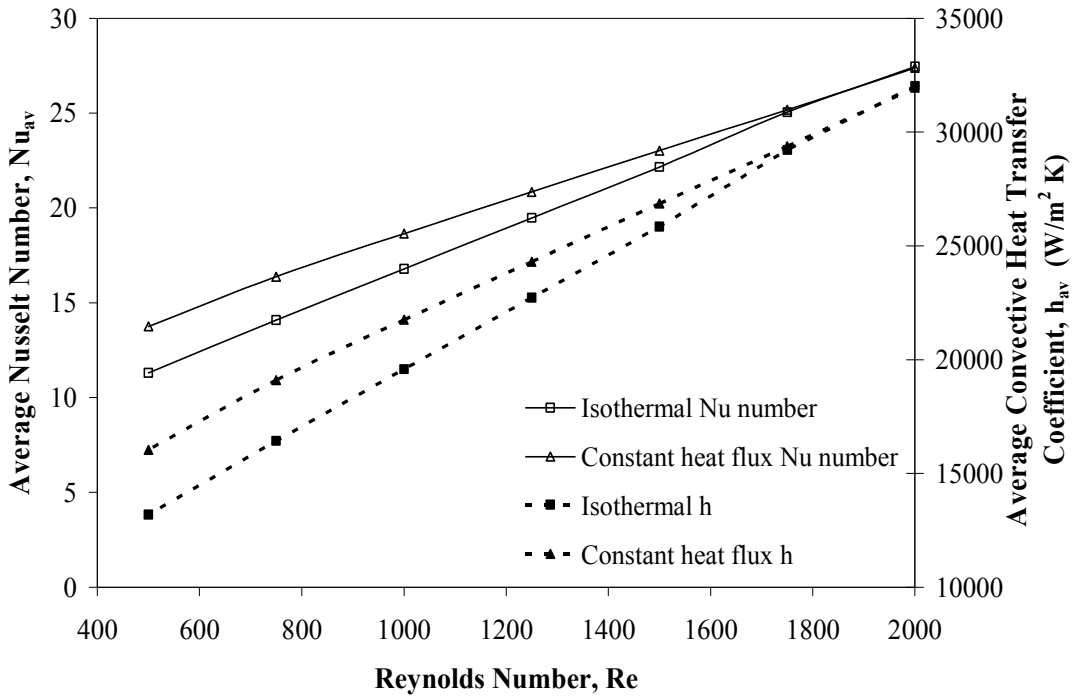

Figure 3.9 Average Nusselt Number and Heat Transfer Coefficient Variation for Different Reynolds Numbers for Constant Heat Flux ($q=250kW/m^2$) and Isothermal ($T_o = 373$ K) Boundary Conditions ($\beta=2.0$, $H_n = 0.30cm$)

The solid-fluid dimensionless interface temperature and local Nusselt number distributions for six different nozzle-to-target spacing for water as the coolant and Reynolds number of 500 are shown in Figures 3.10 and 3.11 respectively.

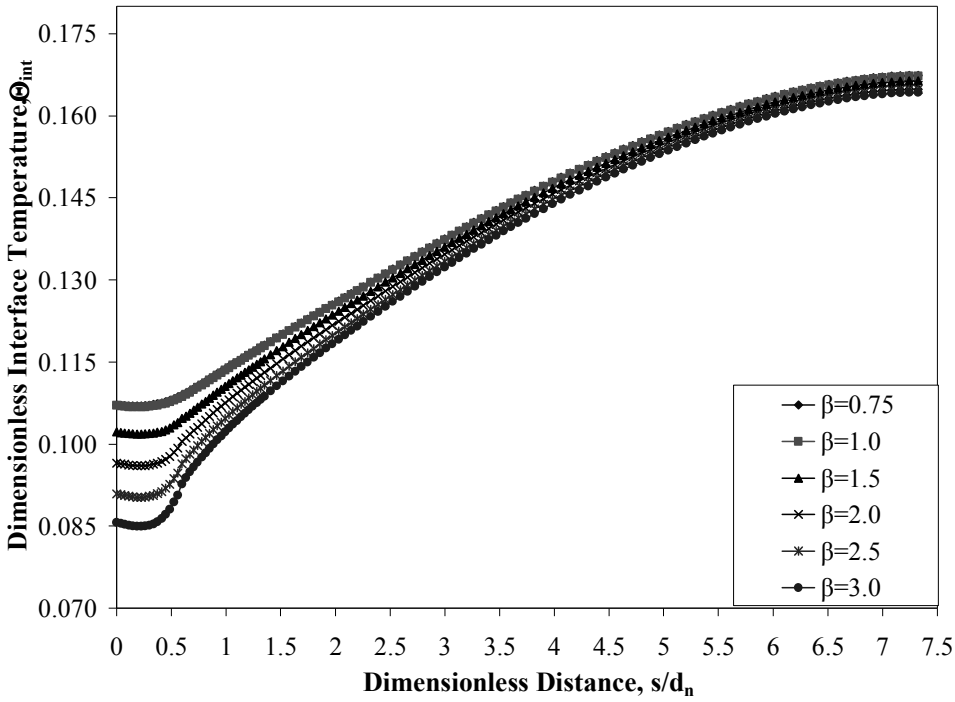

Figure 3.10 Dimensionless Interface Temperature for Silicon Hemisphere at Different Nozzle to Target Spacing Ratio (β) for Water as the Cooling Fluid (Re=500, $Q=3.776\times10^{-7} m^3/s$, $d_n=1.2mm$, b=0.60 mm, $q=250\ kW/m^2$)

It may be noticed that the impingement height quite significantly affects the dimensionless interface temperature as well as the Nusselt number only at the stagnation region and the early part of the boundary layer region.

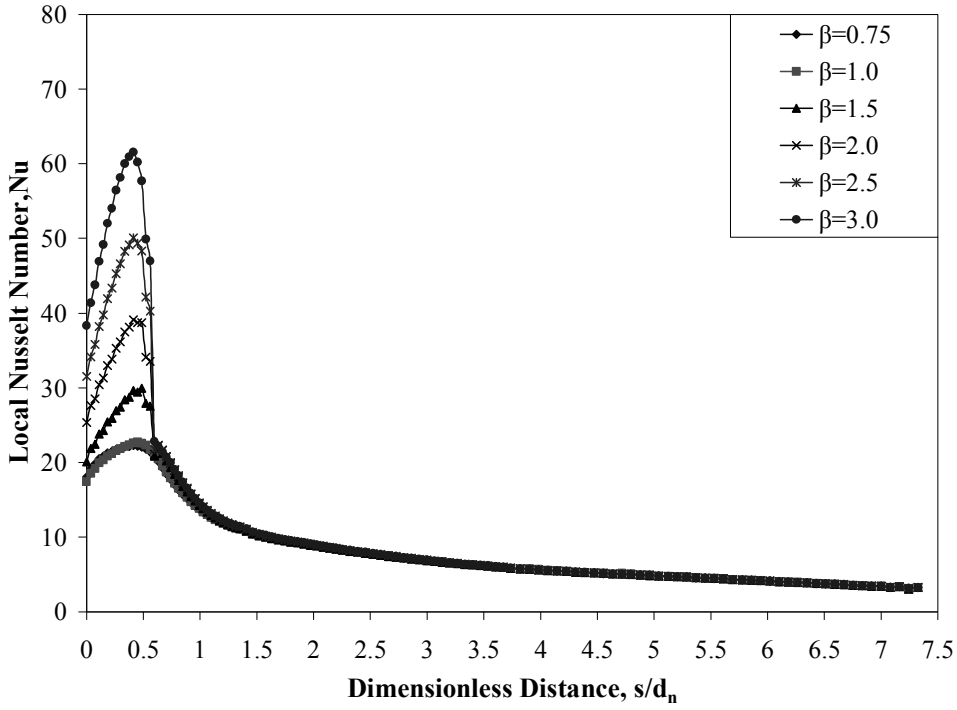

Figure 3.11 Local Nusselt Number for Silicon Hemisphere at Different Nozzle to Target Spacing Ratio (β) for Water as the Cooling Fluid (Re=500, Q=3.776x10^{-7} m^3/s, d_n=1.2mm, b=0.60mm, q=250kW/m^2)

At larger arc length the values get closer for all impingement heights. It is quite expected since the impingement height essentially controls the change in velocity the fluid particles encounter during the free fall from nozzle exit to target hemisphere's surface and therefore affects areas controlled by direct impingement. Figure 3.12 shows dimensionless interface temperature for a constant q. It can be observed that there is a larger variation of interface temperature at a smaller thickness. As the thickness increases, the temperature at the solid-fluid interface becomes more uniform due to higher distribution of heat within the solid by conduction.

It may be also noticed that the average temperature at the solid-fluid interface decreases when the thickness of the solid hemisphere increases. This decrease in temperature is due to lower heat load at increased thickness. In the present investigation, the outer radius of the hemisphere was kept constant (to preserve same β) while the inner radius was varied to get different thicknesses. Since the heat flux imposed in the inner surface of the hemisphere was also kept constant, a smaller inner radius resulted in smaller heat input rate at that boundary. In addition, the resistance of the material to the path of heat flow increases with thickness.

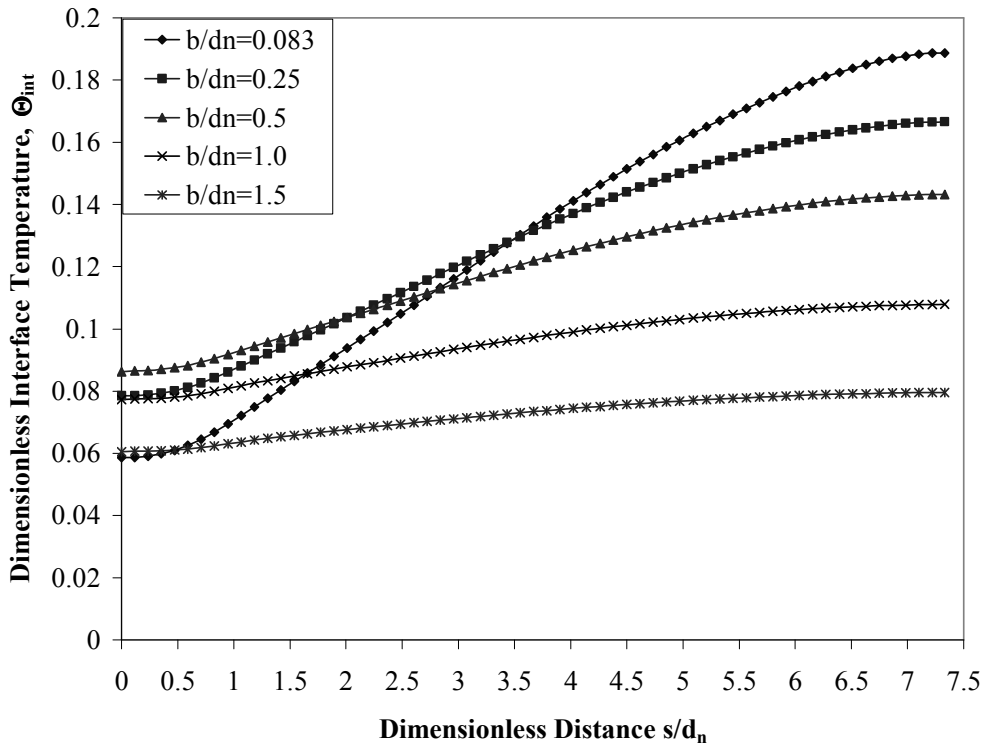

Figure 3.12 Dimensionless Interface Temperature for Silicon Hemisphere at Different Thickness (b) for Water as the Cooling Fluid (Re=750, $Q=5.665\times10^{-7} m^3/s$, $d_n=1.2mm$, b=0.60 mm, $q=250\ kW/m^2$)

Figure 3.13 plots the distribution of local Nusselt number along the surface of the hemisphere for different values of wall thickness. Nusselt number changes by only a small amount over the thicknesses considered in the present investigation when silicon is used as the solid material. A larger peak Nusselt number is obtained at a smaller thickness.

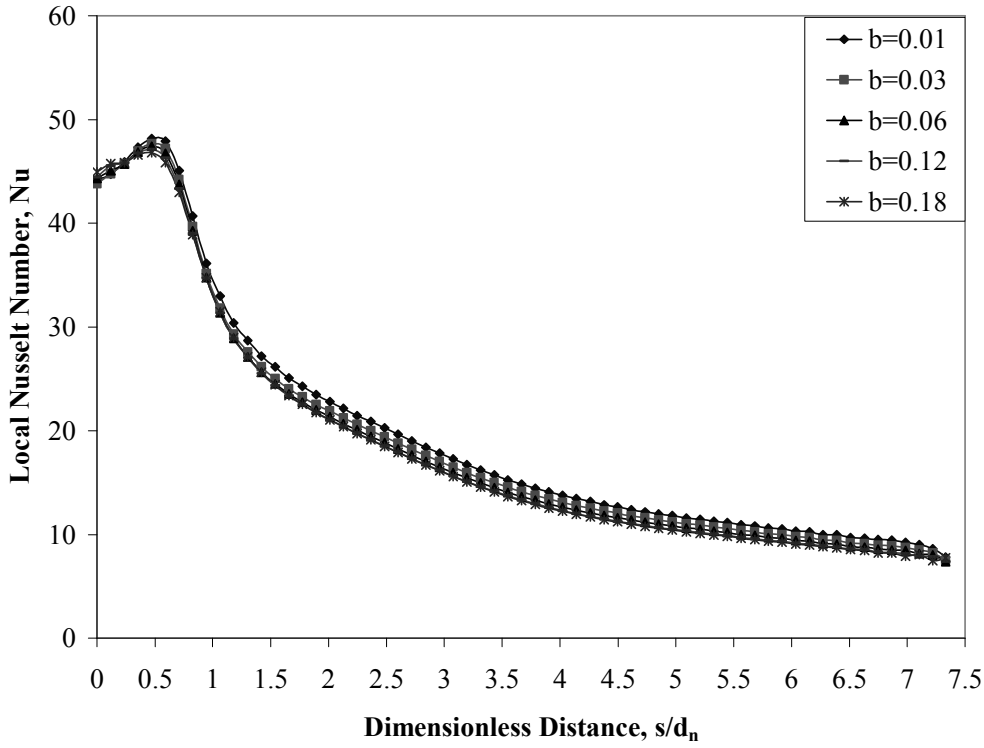

Figure 3.13 Local Nusselt Number for Silicon Hemisphere at Different Thickness (b) for Water as the Cooling Fluid (Re=750, Q=5.665x10^{-7} m^3/s, d_n=1.2mm, b=0.60mm, q=250kW/m^2)

A somewhat similar numerical results were obtained for the isothermal boundary condition of the hemisphere at different thicknesses. Figure 3.14 shows the dimensionless interface temperature for the isothermal case. It can be seen that increasing the thickness contributes to a lower interface temperature at the outer surface of the hemispherical plate. A larger thickness offers a larger

thermal resistance between inner and outer surface of the solid and therefore results in larger temperature drop. Unlike the constant flux case, the variation of interface temperature is more for a thicker plate. It may be also noticed that temperature at the stagnation region is very significantly affected by plate thickness. The local Nusselt number (Figure 3.15) along the plate's interface increased up to s/d_n=0.9 as the plate became thinner. After that, Nusselt number became almost independent of thickness variation and continued decaying along the hemisphere's outer surface.

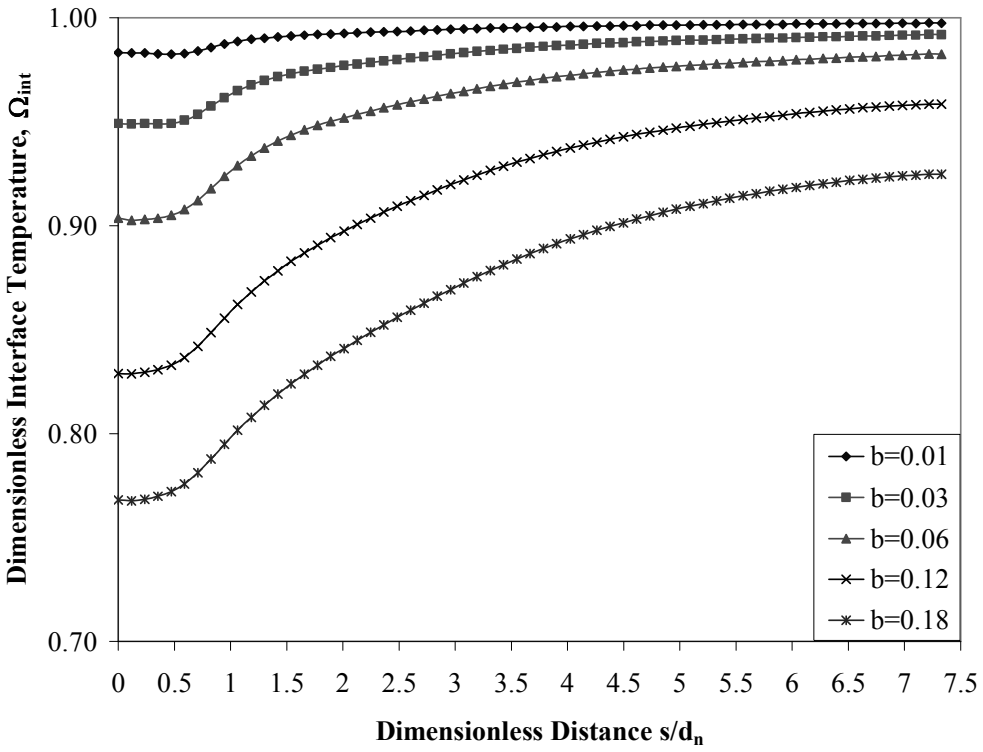

Figure 3.14 Dimensionless Interface Temperature for Silicon Hemisphere at Different Thickness (b) for Water as the Cooling Fluid (Re=750, $Q=5.665\times10^{-7}m^3/s$, d_n=1.2mm, b=0.60 mm, T_o=373 K)

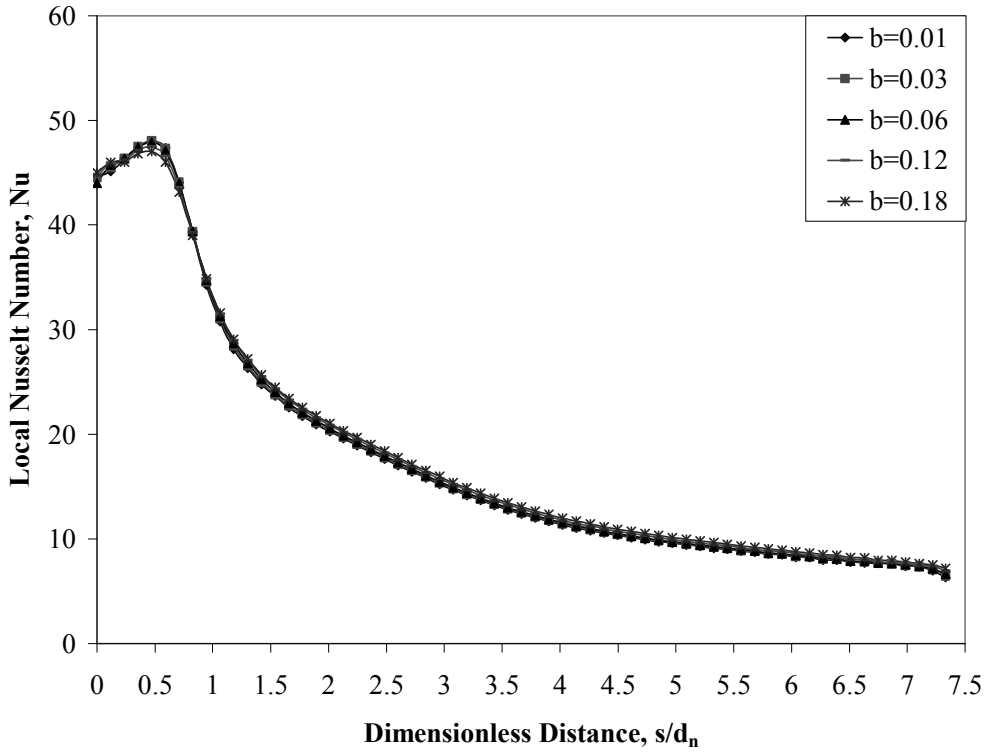

Figure 3.15 Local Nusselt Number for Silicon Hemisphere at Different Thickness (b) for Water as the Cooling Fluid (Re=750, Q=5.665x10^{-7} m^3/s, d_n=1.2mm, b=0.60mm, T_o=373 K)

Figure 3.16 compares the solid-fluid interface temperature for the isothermal boundary condition for the present working fluid (water) with two other coolants that have been considered in previous thermal management studies, namely flouroinert (FC-77) and oil (MIL-7808). It may be noticed that water (T_J=310 K) presents the lowest interface temperature when compared with FC-77 (T_J=273 K) and MIL-7808 (T_J=371 K). The highest Nusselt (Figure 3.17) number is obtained when FC-77 is used as the working fluid (T_j=273.15 K). These results were obtained for a constant Reynolds number of 750.

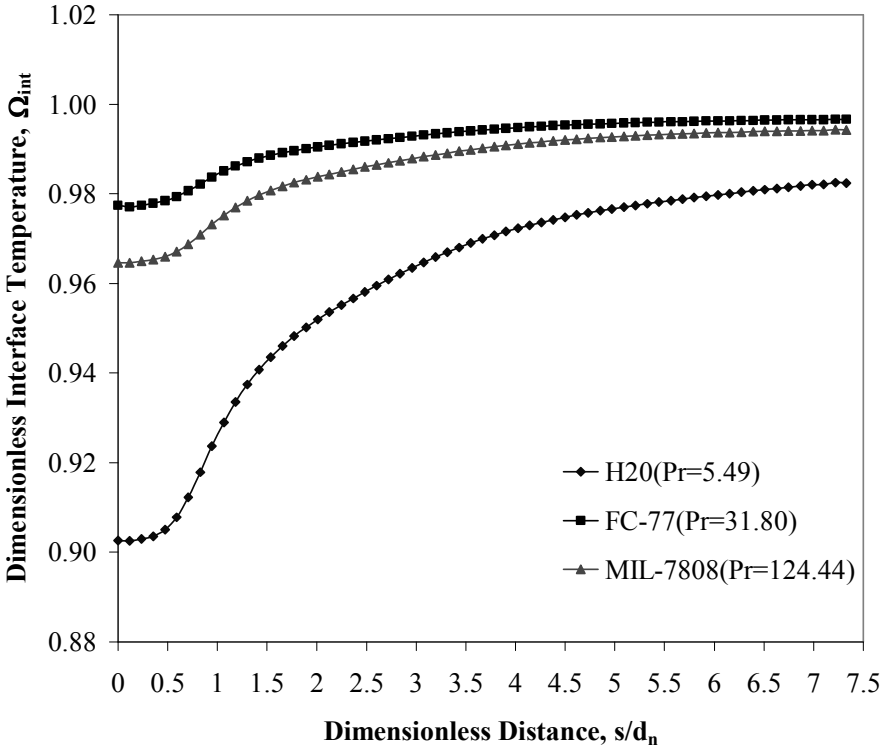

Figure 3.16 Dimensionless Interface Temperature for Silicon Hemispherical Plate for Different Cooling Fluids (Re=750, Q=5.665x10^{-7}m^3/s, d_n=1.2mm, b=0.60 mm, T_o=373 K)

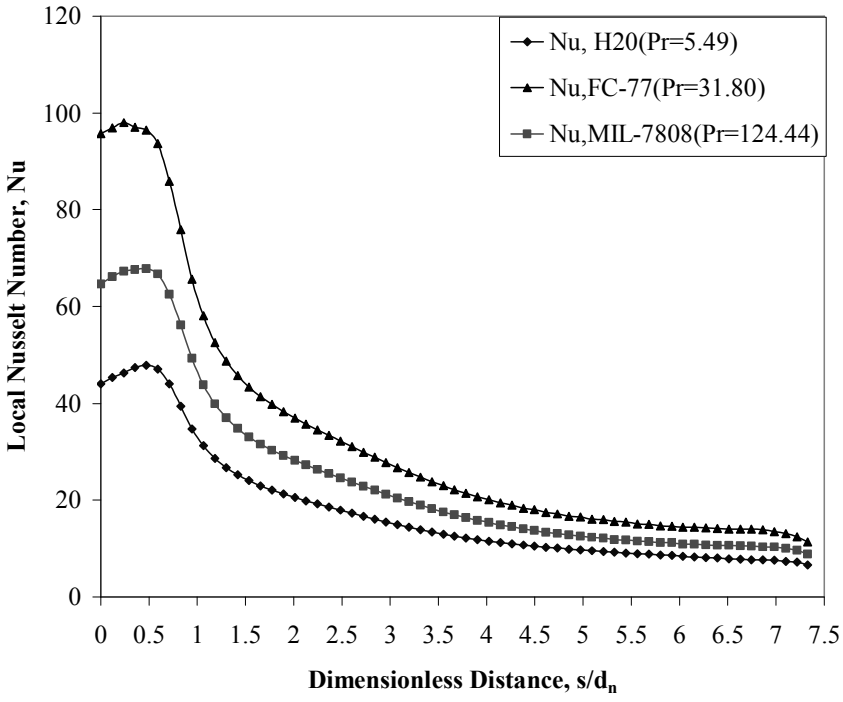

Figure 3.17 Local Nusselt Number for Silicon Hemisphere for Different Cooling Fluids (Re=750, Q=5.665x10^{-7} m^3/s, d_n=1.2mm, b=0.60mm, T_o=373 K)

Figure 3.18 compares the hemisphere's solid-fluid interface temperature and local Nusselt number results of water with flouroinert (FC-77) and oil (MIL-7808) for the constant heat flux boundary condition. It may be noticed that water presents the lowest interface temperature and highest Nusselt number distribution in comparison with FC-77 and MIL-7808. The lowest Nusselt number is obtained when FC-77 is used as the working fluid. These results were obtained for a constant Reynolds number of 1500.

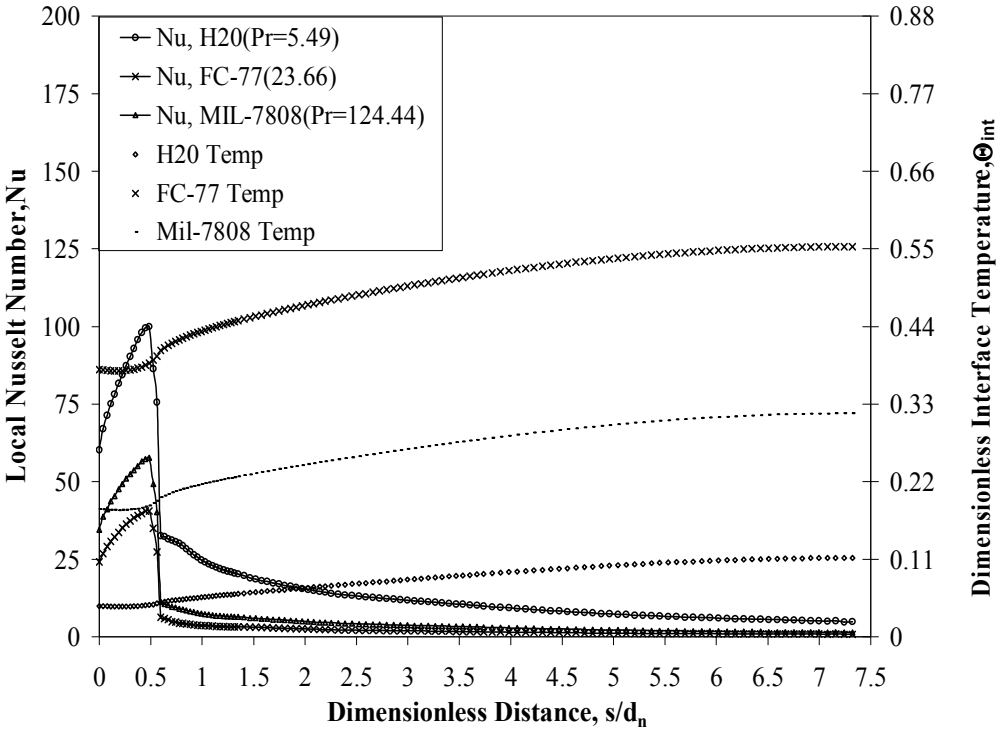

Figure 3.18 Local Nusselt Number and Dimensionless Interface Temperature for Different Cooling Fluids (Re = 1500, Q=1.133x10^{-6}m^3/s, β=2.0, H_n=0.30 cm, b=0.60 mm, q=250 kW/m^2)

Figure 3.19 shows the dimensionless interface temperature and local Nusselt number distribution plots as a function of a dimensionless radial distance (s/d_n) for different solid materials with water as the working fluid. The studied

materials were silicon, silver, aluminum, copper, and Constantan, having different thermo-physical properties. Constantan shows the lowest dimensionless temperature at the impingement zone and the highest at the outlet in comparison with other solid materials. Copper and silver show a more uniform distribution and higher temperature values at the impingement zone due to their higher thermal conductivity. The dimensionless temperature and local Nusselt number distributions of these two materials are almost identical due to their similar thermal conductivity values. The cross-over of curves for all five materials occurred due to a constant fluid flow and heat flux rates that provide a thermal energy balance. Solid materials with lower thermal conductivity show higher maximum local Nusselt number. The choice of material is also crucial in determining the magnitudes of these temperatures. A material with larger thermal conductivity will facilitate a faster rate of heat transfer, and therefore will result in a lower maximum temperature at the solid-fluid interface and within the hemispherical plate. The temperature difference at the interface is an indication of the level of temperature non-uniformity at the impingement surface.

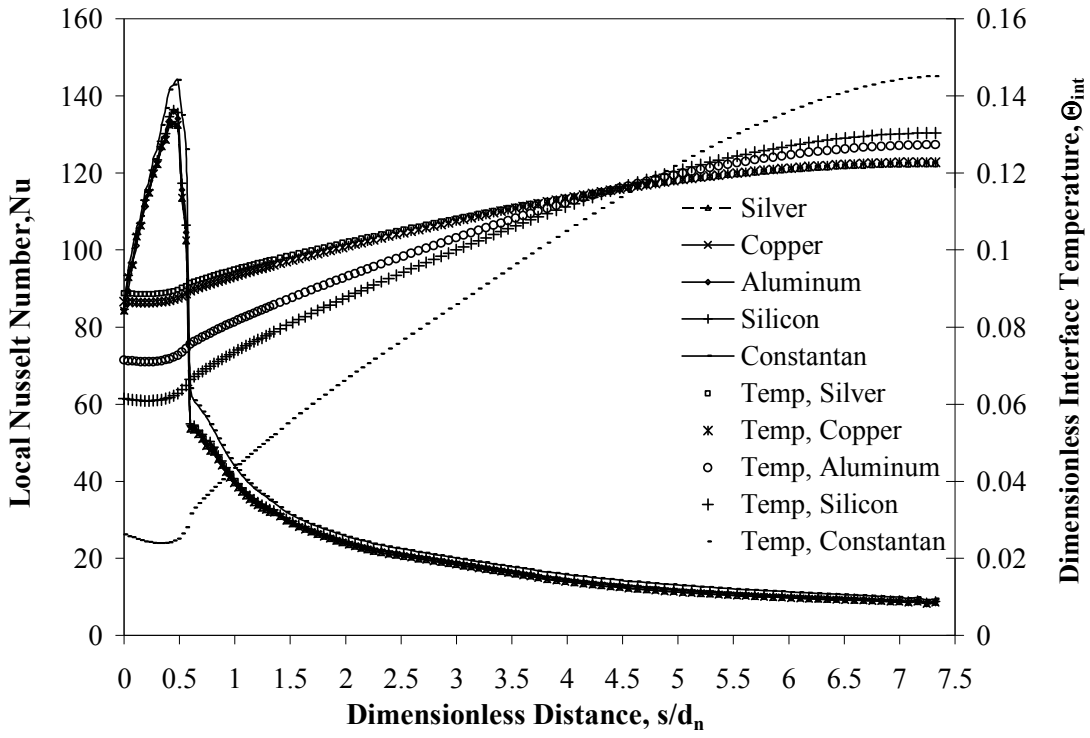

Figure 3.19 Local Nusselt Number and Dimensionless Interface Temperature for Different Hemisphere Materials with Water as the Cooling Fluid (Re=1000, β=2.0, b/d_n=0.5, q=250 kW/m^2)

Dimensionless interface temperature and local Nusselt number were also investigated for various solid plate materials such as silicon, silver, aluminum, copper, and Constantan using the same working fluid (water) for the isothermal boundary condition. Figure 3.20 demonstrates that materials with higher thermal conductivity such as silver and copper maintain a higher and more uniform temperature distribution along the solid-fluid interface transferring heat faster towards the hemisphere's outer surface. Constantan has significantly lower interface temperature due to higher thermal resistance offered by it. Also, the interface temperature varies over a larger range due to lower rate of conduction heat transfer within the solid. In Figure 3.21, it can be observed that the local

Nusselt number changes only slightly with solid properties and curves are very close to each other.

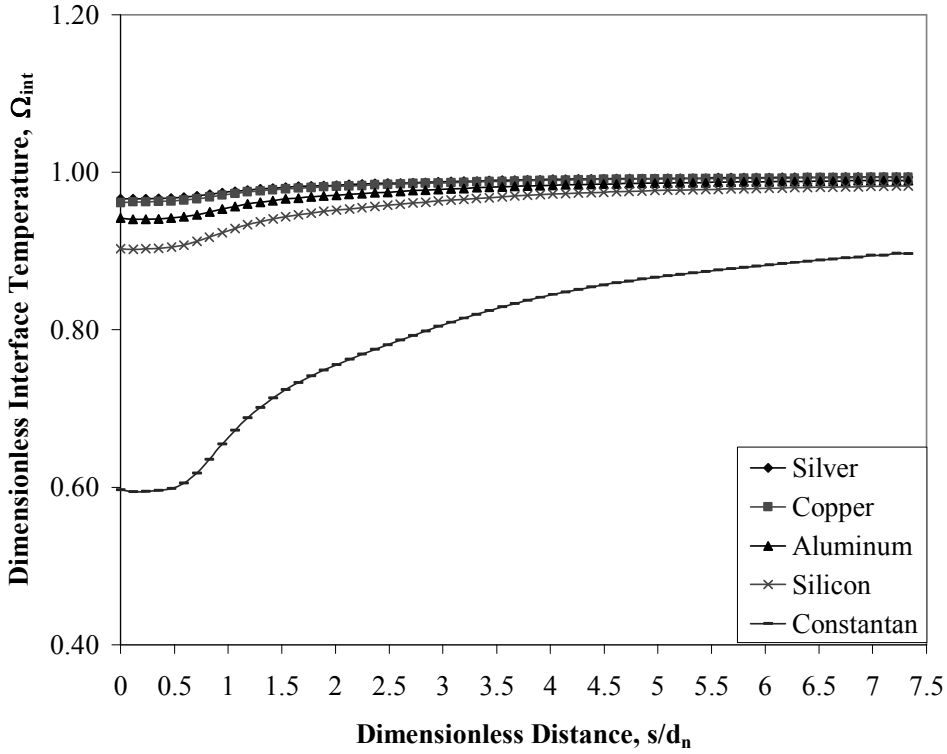

Figure 3.20 Dimensionless Interface Temperature for Silicon Hemispherical Plate for Different Materials (Re=750, Q=5.665x10^{-7}m^3/s, d_n=1.2mm, b=0.60 mm, T_o=373 K)

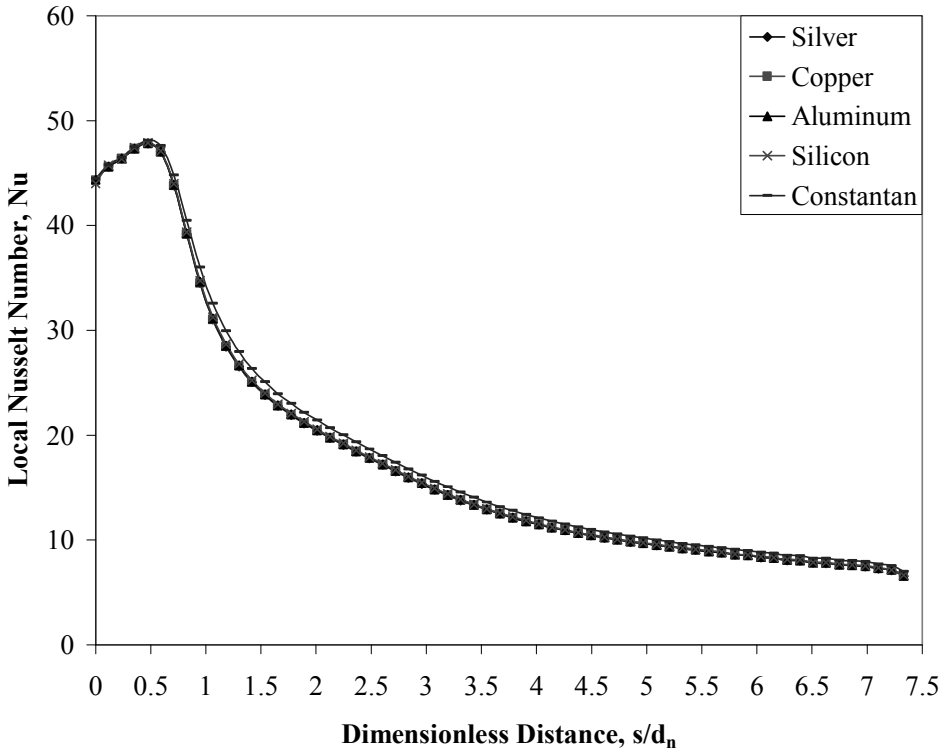

Figure 3.21 Local Nusselt Number Distribution for Silicon Plate for Different Solid Materials (Re=750, Q=5.665x10^{-7} m^3/s, d_n=1.2mm, b=0.60mm, T_o=373 K)

Three of the papers used for the validation of this numerical study were the analytical works carried out by Liu et al. [36], Scholtz and Trass [37], and Nakoryakov et al. [38] using fluid for Prandtl number greater than unity (Pr>1) as coolants. The fluids were tested for heat removal under free liquid jet impingement on a heated flat surface maintained at uniform heat flux. The graphical representation of actual numerical Nusselt number results at the stagnation point at different Reynolds number are shown in Figure 21. The results shown at Figure 21 compared within 7.20% of Scholtz and Trass [37], within 8.48% of Nakoryakov et al. [38], and within 7.76% of Liu et al. [36]. The local Nusselt number under Reynolds number at 500, 750, 1000, 1250 and 1500

correlates with a margin of 12.17%, 5.65%, 3.35%, 6.00%, and 11.85% respectively. Considering the errors inherent in any experimental study as well as discretization and round-off errors in the simulation, this comparison is quite satisfactory. In addition, the surface curvature may have affected the heat transfer characteristics near the impingement region that was not present in experimental studies.

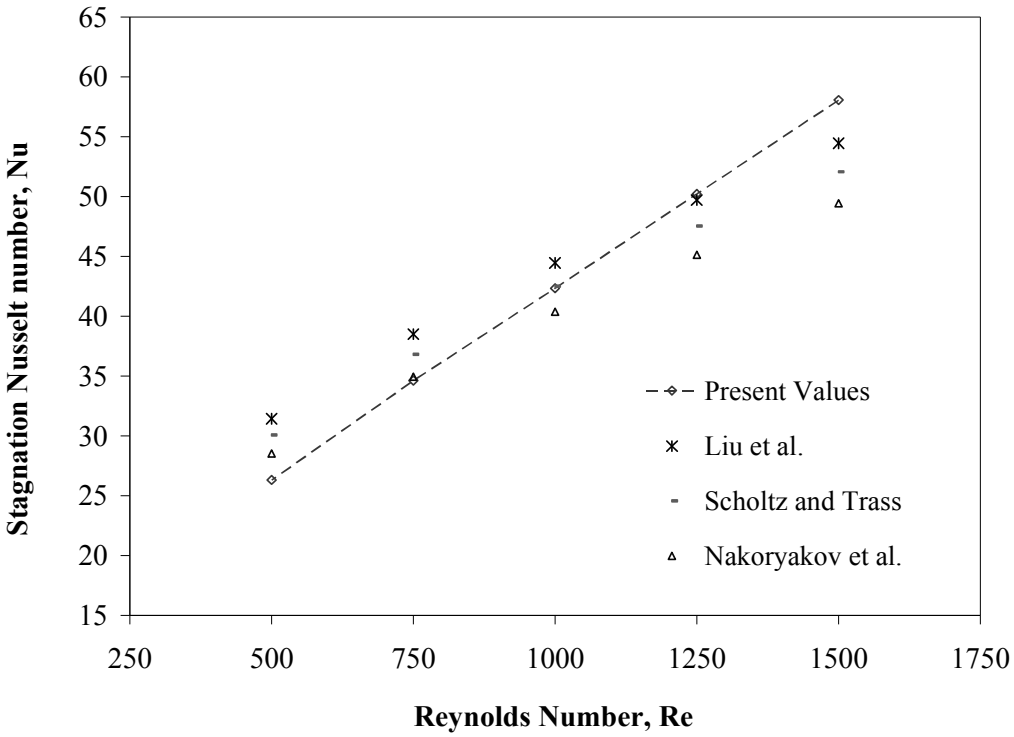

Figure 3.22 Stagnation Nusselt Number Compared with Liu et al. [36], Scholtz and Trass [37], and Nakoryakov et al. [38] with Actual Numerical Results under Different Reynolds Numbers (d_n = 1.2mm, b=0.6mm, q=250kW/m^2)

3.2 Transient Heating

In order to understand the thermal response of solid materials to the flowing of heat when the power source is turned on (t > 0), it is necessary to analyze the transient heat transfer process when a local heat flux travels throughout the entire solid up to its outer surface and to the cooling fluid. The local heat flux variation along the solid-fluid interface for different time intervals is shown in Figure 3.23. Since an initial isothermal condition was assumed at the beginning of the process, the interfacial heat flux is zero at t=0 s. As expected, the heat flux at the solid-fluid interfaces increases with time. A much larger heat flux is seen at the stagnation region since the cold fluid at the jet strikes that region and keeps the minimum temperature at that location. This behavior occurs due to the constant renewal of cold fluid to dissipate the heat. The heat dissipated is utilized to rise the temperature of the solid as well as the fluid and reduces thermal storage within the solid due to convective heat transfer. Another maximum heat flux is encountered around s/d_n=0.5, and then it decreases downstream. This is due to the transition of the fluid from the vertical impingement to a thin film flow along the curved surface where the boundary layer starts to develop. This peak can be associated with the start of the thermal boundary layer in the thin film structure. Figure 3.23 also presents $q_{av,int}\, r_o^2/q_w r_i^2$ which is the ratio of the energy transmitted to the fluid to the energy input at the bottom face of the hemisphere. It may be noticed that a large amount of energy is absorbed by the solid at the early part of the transient and more and more

energy is dissipated to the fluid as the transient progresses. The interfacial heat flux reaches within 1% of the steady-state equilibrium condition at F_o= 0.103.

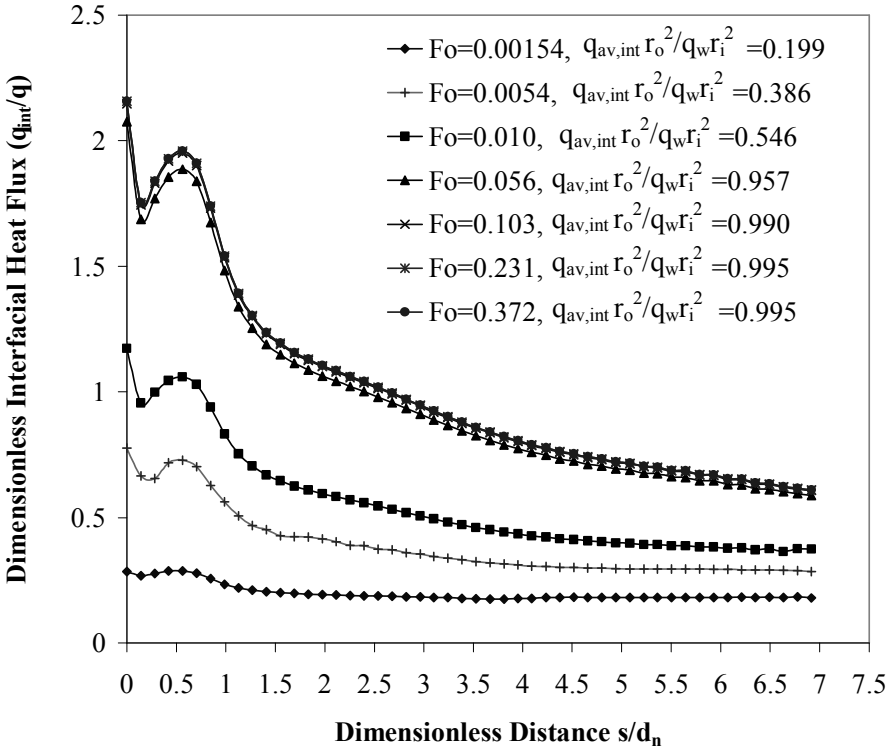

Figure 3.23 Dimensionless Local Heat Flux Variation at the Solid-Fluid Interface for Silicon Hemisphere at Different Time Instants (Re=750, b/d_n=0.5, ß=2.5)

Figure 3.24 illustrates the dimensionless interface temperature for different time instants. As can be observed at the very beginning of the heat transfer process, the solid-fluid interface maintains a uniform temperature compared to that when approaching the steady-state condition. This pattern is due to the thermal storage in the fluid necessary to develop the thermal boundary layer since an isothermal condition was present at the beginning of the problem. As time goes on, the thickness of the thermal boundary layer increases and therefore the temperature rises. Figure 3.24 also illustrates the difference of

maximum-to-minimum temperature at the interface being the maximum located at the outer edge of the hemisphere and the minimum at the stagnation point of the hemisphere due to the constant renewal of cold fluid from the nozzle. Thus, such temperature difference increases with time as more heat flows throughout the hemispherical solid and transmitted to the fluid. The range of temperature encountered at the solid-fluid interface increases with time and reaches a constant value at the steady state.

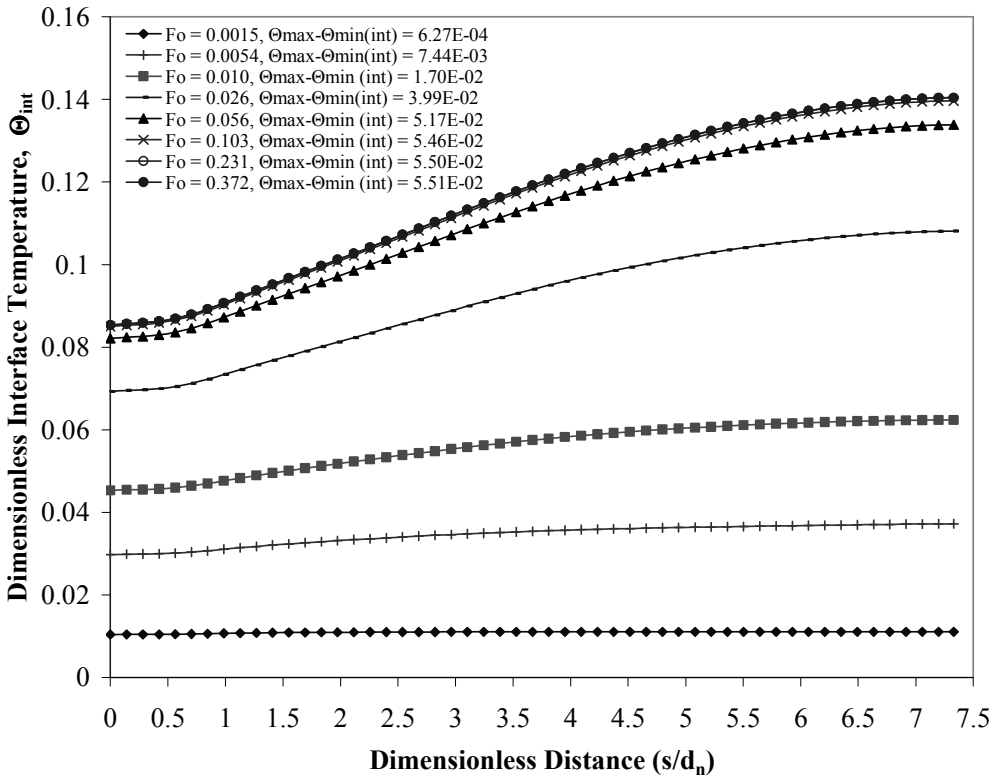

Figure 3.24 Dimensionless Interface Temperature Variation for Silicon Hemisphere at Different Time Instants (Re=750, b/d_n=0.5, ß=2.5)

Fig. 3.25 shows the variation of local Nusselt number along the solid-fluid interface at different time instants. The local Nusselt number is controlled by local temperature and heat flux at the solid-fluid interface. Both of these

quantities increase with time. The local Nusselt number shows a higher value at early stages of the transient process due to smaller temperature difference between the jet and the outer surface of the hemisphere. This essentially means that all heat reaching the solid-fluid interface via conduction through the solid is more efficiently convected out as the local fluid temperature is low everywhere at the interface. The local Nusselt number decreases with time until it reaches the steady-state equilibrium distribution. Figure 3.25 also provides the integrated average Nusselt number for the entire hemispherical surface. As expected, the average Nusselt number is large at the early part of the transient and monotonically decreases with time ultimately reaching the value for the steady state condition.

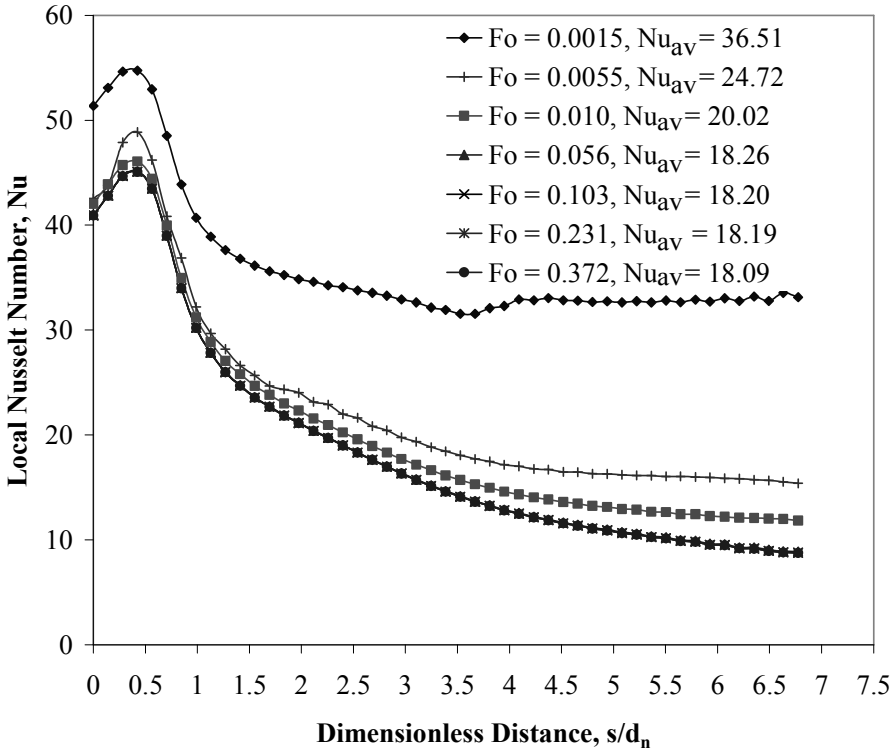

Figure 3.25 Local Nusselt Number Distribution for Silicon Hemisphere at Different Time Instants (Re=750, b/d$_n$=0.5, ß=2.5)

Figure 3.26 presents results for dimensionless maximum temperature at the interface, maximum temperature in the solid, and maximum-to-minimum difference temperature at the interface for two different Reynolds numbers. The maximum temperature within the solid was encountered at the outlet plane next to the heated surface ($z=-r_o$, $r=r_i$). As noticed, the temperature begins to rise with time as the hemispherical solid begins to store heat starting after the specified initial condition (T_J=310 K) showing a rapid response at the earlier part of the heating process until its thermal storage capacity reduces up to its limit (steady-state). It is important to mention that the time necessary to reach steady-state depends strongly on the Reynolds number.

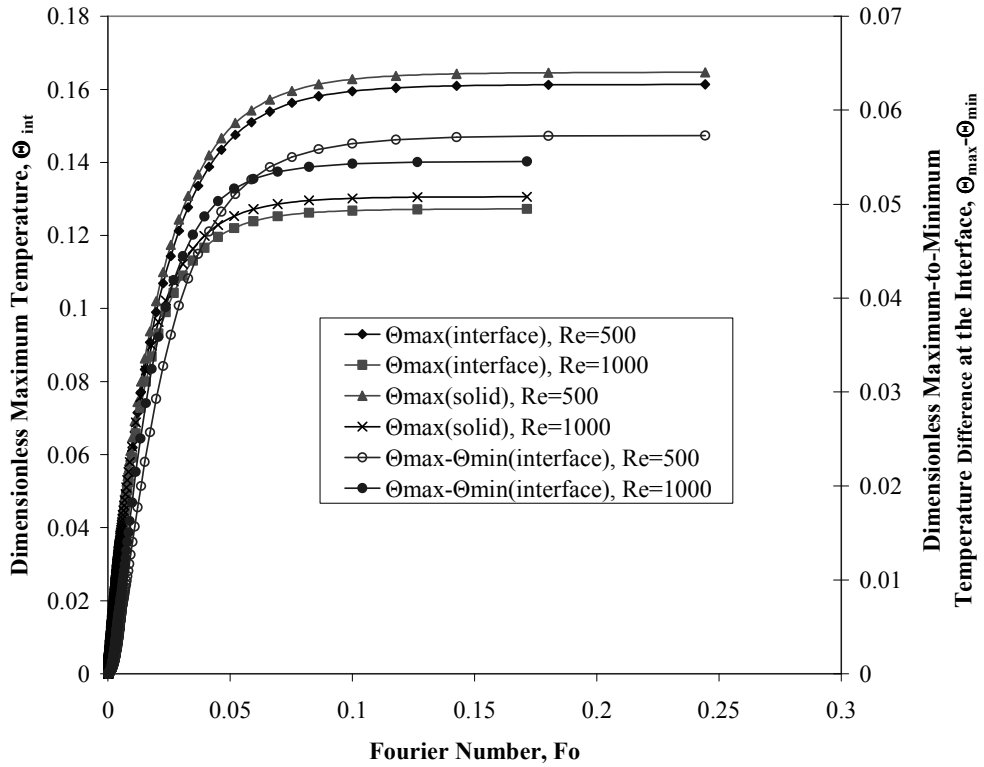

Figure 3.26 Distribution of Dimensionless Maximum Temperature at the Solid-Fluid Interface, within the Solid, and Maximum-to-Minimum Temperature Difference with Time for Two Reynolds Numbers (Silicon Hemisphere, b/d_n=0.5, ß=2.5)

Figure 3.26 also confirms that a higher Reynolds number increases convective heat transfer and therefore lowers the hemisphere's temperature. The control of maximum temperature is important in many critical thermal management applications including electronic packaging.

Figure 3.27 plots the average Nusselt number variation along the solid-fluid interface for two different Reynolds numbers over the entire transient start-up of the heat transfer process. As expected, the average Nusselt number becomes larger as the Reynolds number increases due to higher velocity of the fluid particles moving along the hemisphere's outer surface, hence, increasing the rate of heat transfer.

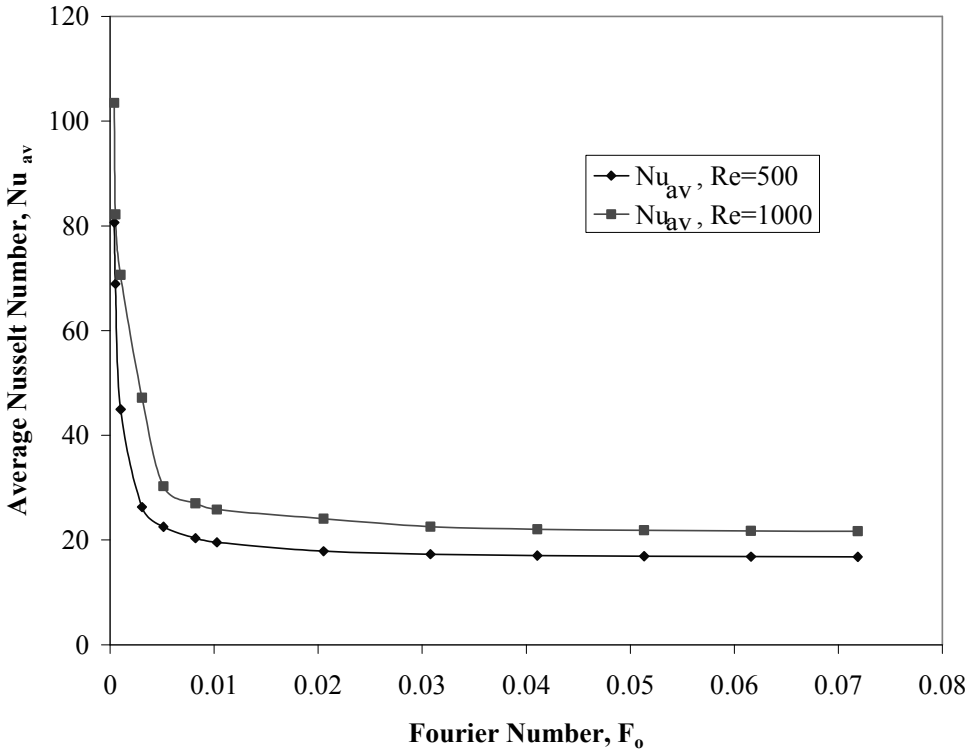

Figure 3.27 Variation of Average Nusselt Number with Time For Silicon Hemisphere at Two Different Reynolds Numbers (b/d_n=0.5, ß=2.5)

The time required to reach steady-state for different Reynolds numbers is presented in Figure 3.28. Fo_{ss} was defined as the Fourier number at which the solid-fluid interface temperature everywhere on the hemispherical plate reached within 0.001% of the steady equilibrium distribution. The time to reach thermal equilibrium condition decreases as the Reynolds number increases in value. This is due to more fluid flow rate available to carry away the heat and faster development of thermal boundary layer that is smaller in thickness.

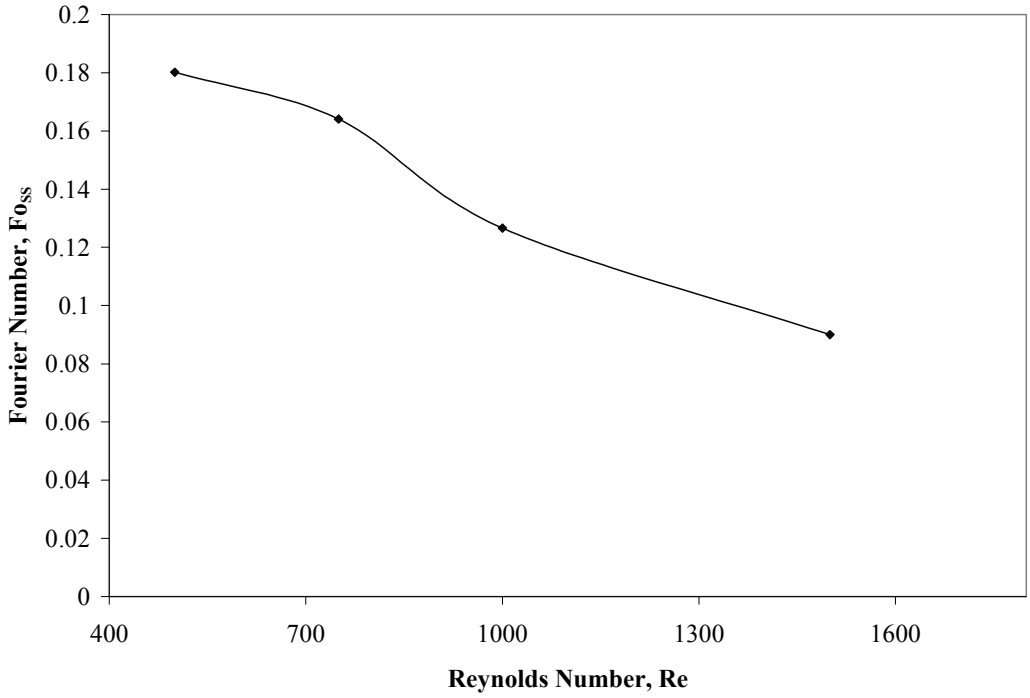

Figure 3.28 Time Required to Reach Steady-State for Silicon Hemisphere at Different Reynolds Numbers (b/d_n=0.5, ß=2.5)

The effects of varying the thickness in the hemispherical plate on maximum temperature at the interface, maximum temperature within the solid, and maximum-to-minimum temperature difference at the interface can be seen

on Figure 3.29. The plate thickness significantly affects the temperature distribution. It may be note that as the thickness of the hemispherical plate increases, the time needed to achieve steady-state conditions increases. This is due to more storage capacity of heat within the solid. Also, the temperature at the solid-fluid interface remains lower due to higher thermal resistance of the solid to the path of heat flow.

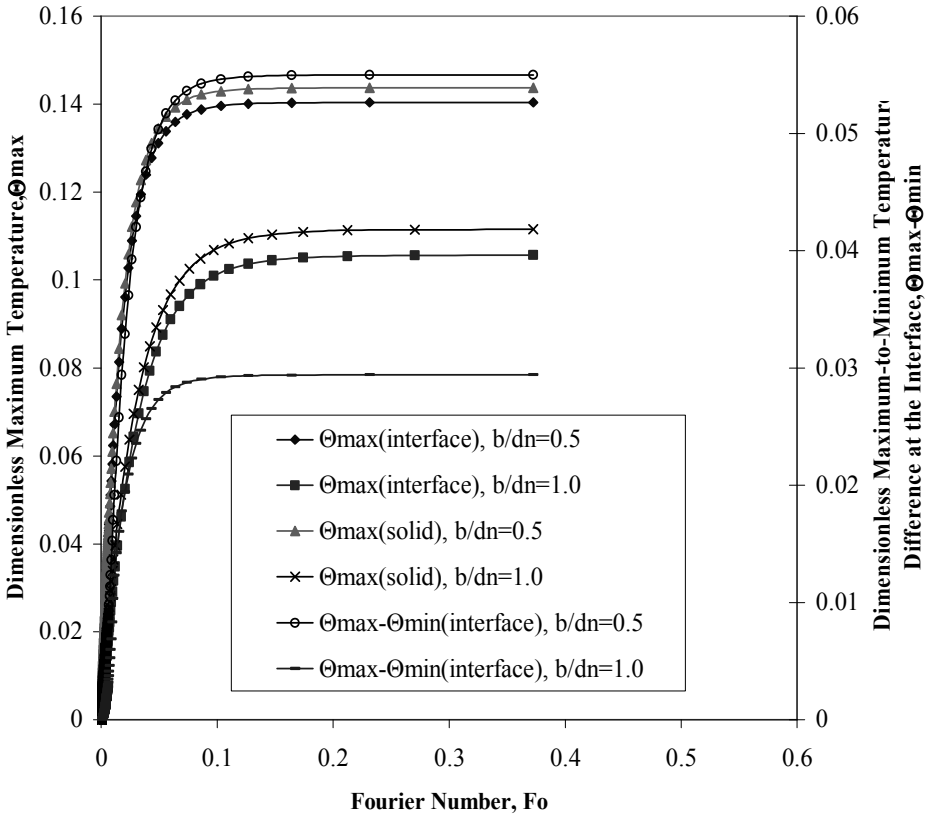

Figure 3.29 Distribution of Dimensionless Maximum Temperature at the Solid-Fluid Interface, within the Solid, and Maximum-to-Minimum Temperature Difference with Time for Different Plate Thicknesses (Silicon Hemisphere Re=750, ß=2.5)

Figure 3.30 shows the average Nusselt number variation as a function of time for three distinct plate thicknesses using Constantan as the solid material. The average Nusselt number is higher for higher plate thickness.

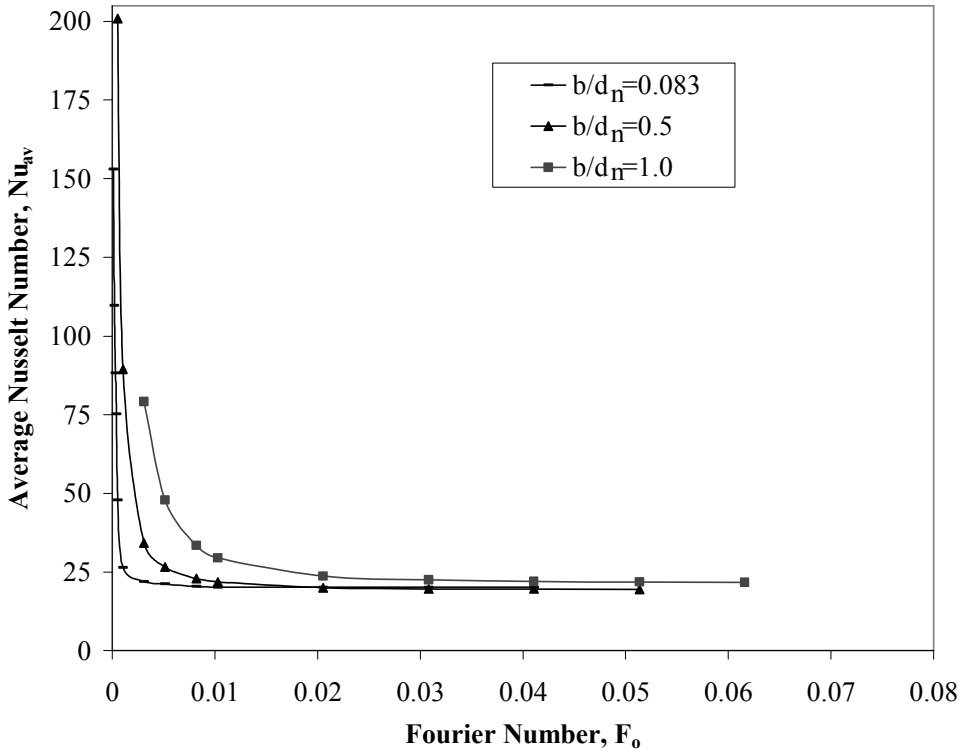

Figure 3.30 Variation of Average Nusselt Number with Time for Constantan Hemisphere at Three Different Thicknesses (Re=750, ß=2.5)

The maximum temperature at the solid-fluid interface, maximum temperature within the solid, and maximum to minimum temperature difference (as a measure for temperature non-uniformity) for different solid materials is presented in Figure 3.31. As expected, the temperature changes occur faster at the beginning of the heating process for all materials and the slope gradually decays when the steady-state approaches. It can be observed that materials

with a very low thermal conductivity such as Constantan maintains a higher temperature at the hemisphere's outer surface and within the solid as the thermal conductivity controls how effective the heat flows and distributes throughout the material. The thermal diffusivity of the material also contributes to the transient behavior of the solid. As noticed, Silicon and Copper reach the steady-state faster than Constantan due to their higher thermal diffusivity, which controls the rate of heat being transferred through the solid material.

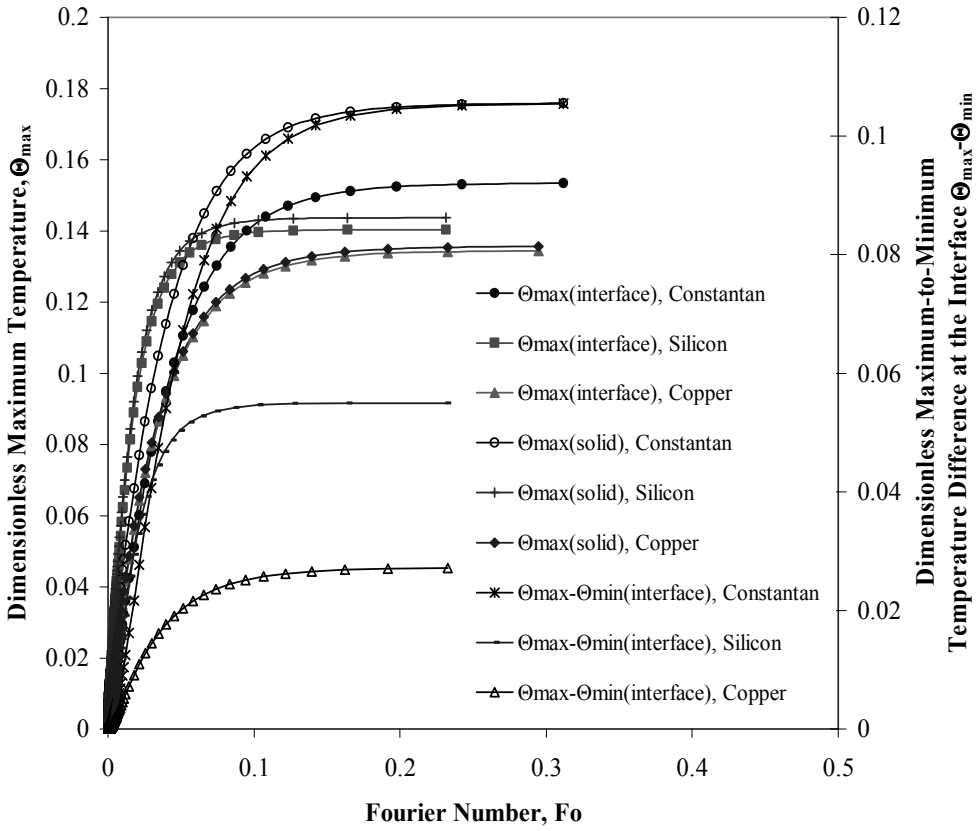

Figure 3.31 Distribution of Dimensionless Maximum Temperature at the Solid-Fluid interface, within the Solid, and Maximum-to-Minimum Temperature Difference with Time for Different Materials (Re=750, ß=2.5)

Figure 3.32 shows the distribution of average Nusselt Number with time for the three materials used in this study. Constantan shows a higher average heat transfer coefficient compared to Silicon or Copper over the entire transient process. A significant difference is seen at the earlier part of the transient and the curves come close together as the steady-state approaches.

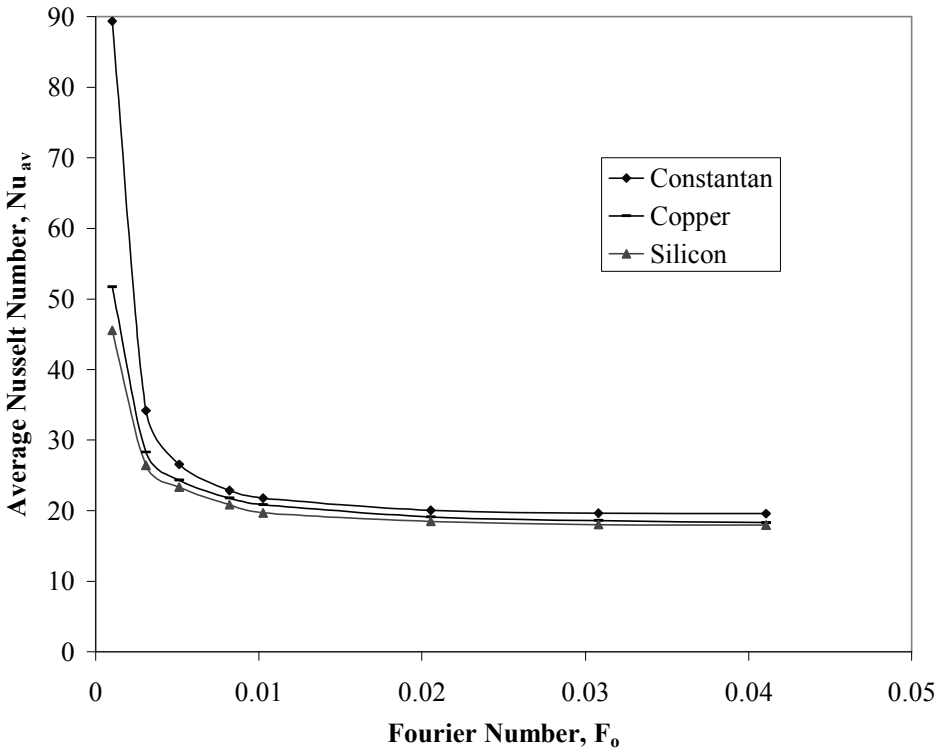

Figure 3.32 Variation of Average Nusselt Number with Time for Different Materials (Re=750, b/d_n,=0.5, ß=2.5)

It will be also important to know how the materials responded in reaching thermal equilibrium based on their thickness. Figure 3.33 presents Fo_{ss} for these materials for different plate thicknesses. As the thickness increases in value, the time to reach steady-state also increases. Constantan takes longer in reaching steady-state due to its lower thermal diffusivity compared to Copper and Silicon.

Also, the property of the solid plays more significant role in determining the duration of the transient heat transfer process when the thickness is increased.

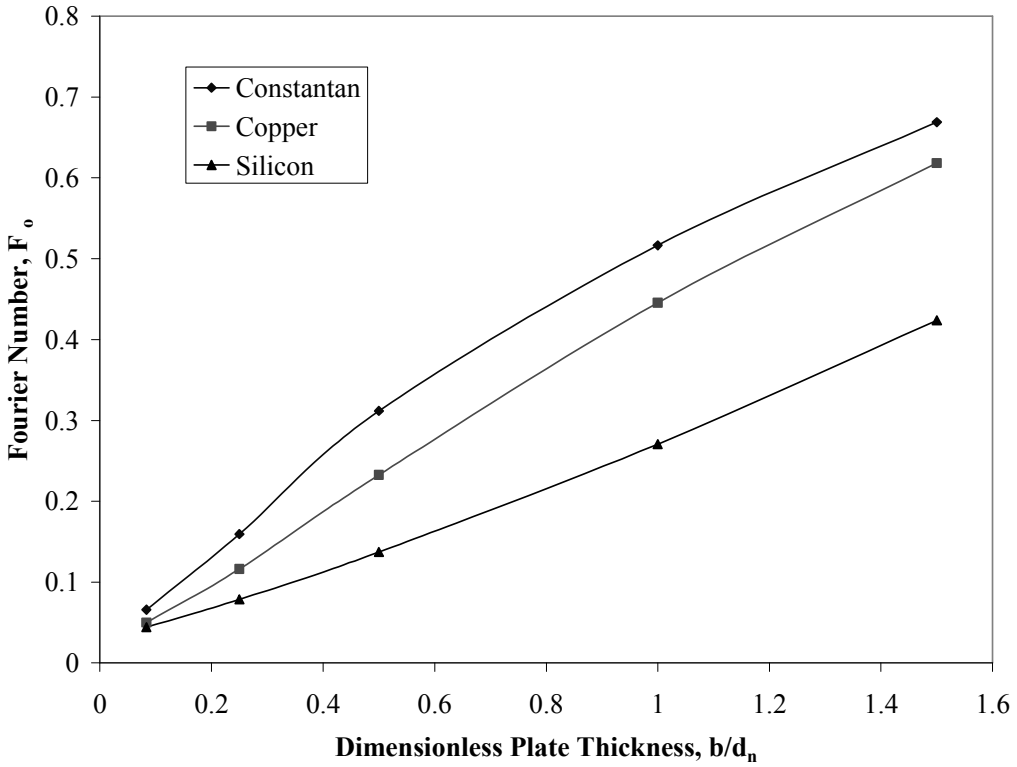

Figure 3.33 Time Needed to Reach Steady-State for Different Hemispherical Plate Thicknesses and for Different Materials (Re=750, ß=2.5)

The development of isothermal lines within the solid can be observed in Figure 3.34 at different time instants for b/d_n=0.5. It is important to notice that at early stages of the transient heat transfer process, the isothermal lines grow parallel to the inner (bottom) heated surface of the hemispherical plate. As time goes on, the isothermal lines start moving upward toward lower temperature regions until they reach the solid-fluid interface. After that, they start to form

concentric lines near the stagnation point and expand further down into the solid until a steady-state condition is achieved.

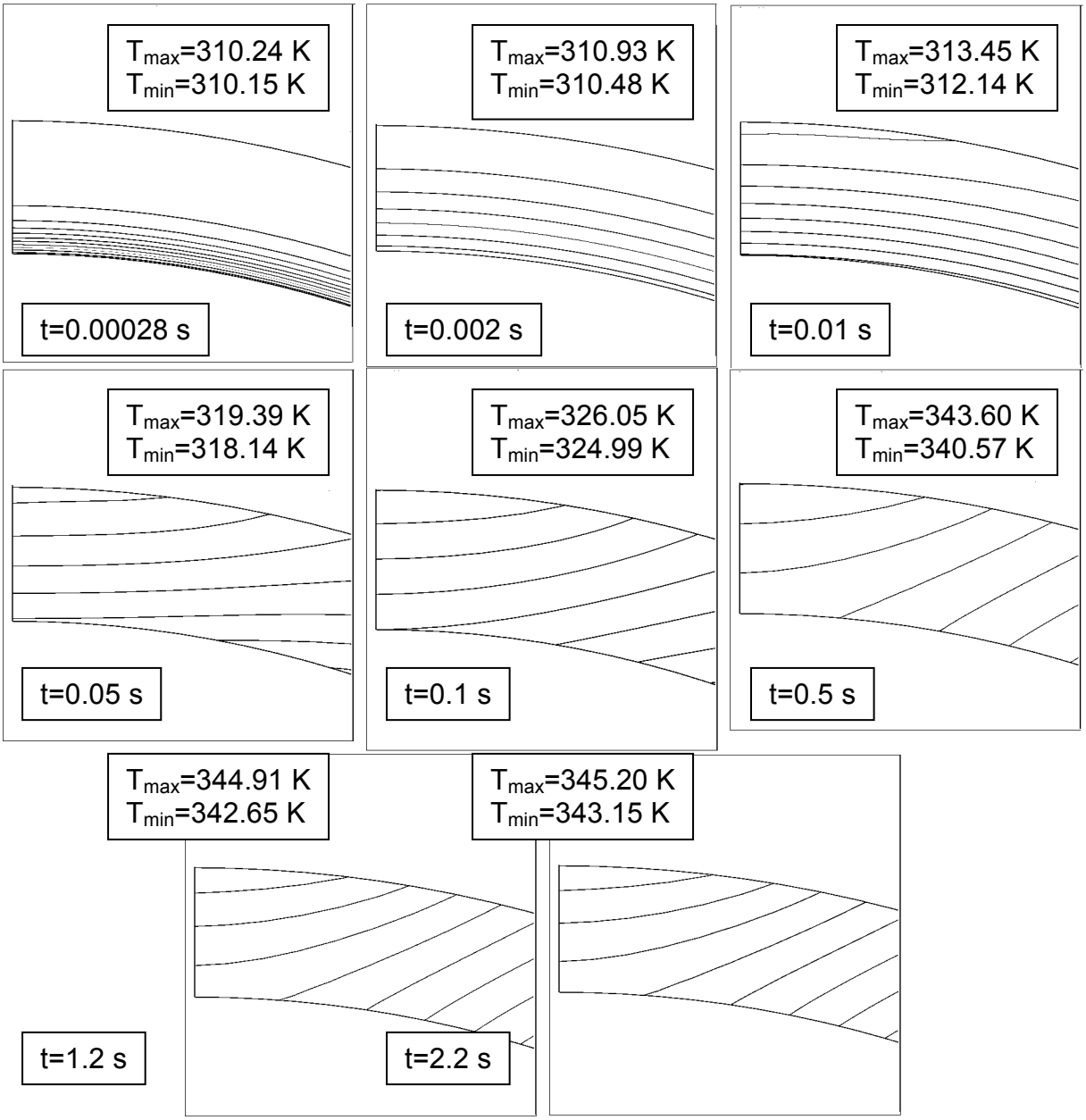

Figure 3.34 Isotherms Countour Lines at Varius Time Instants for Silicon Hemisphere Plate of b/d_n=0.5 (Re=750, ß=2.5, Top Left Corner (z=0, r=0))

Figure 3.35 shows the same phenomenon for b/d_n=1.5. The temperatures inside the solid are much lower as compared to a thinner plate and the time to reach steady-state equilibrium thermal condition increases.

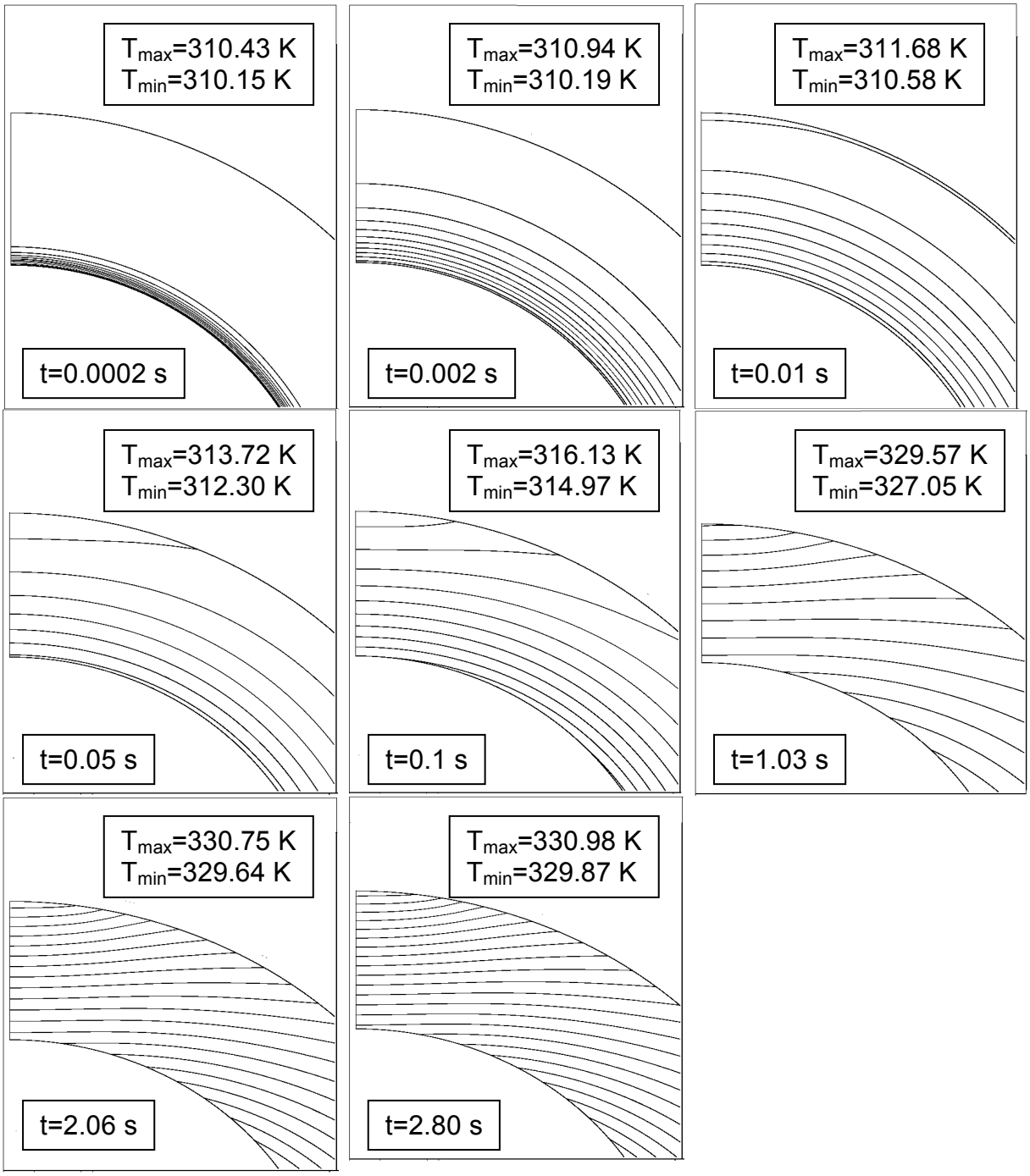

Figure 3.35 Isotherms Countour Lines at Varius Time Instants for Silicon Hemisphere Plate of b/d_n=1.5 (Re=750, ß=2.5, Top Left Corner (z=0, r=0)

Chapter 4 Cylindrical Plate Model Results

4.1 Steady State Heating

A velocity vector distribution is shown in Figure 4.1. It can be observed that the velocity remains almost uniform at the potential core region of the jet. However, the velocity decreases and the fluid jet diameter increases as the fluid gets closer to the surface during the impingement process. The direction of motion of the fluid particles shifts along the angle of curvature, afterwards, the fluid accelerates creating a region of minimum sheet thickness. That is the beginning of the boundary layer zone. It can be noticed that as the fluid moves downstream along the convex surface, the boundary layer thickness increases and the frictional resistance from the wall is eventually transmitted to the entire film thickness where the fully viscous zone develops.

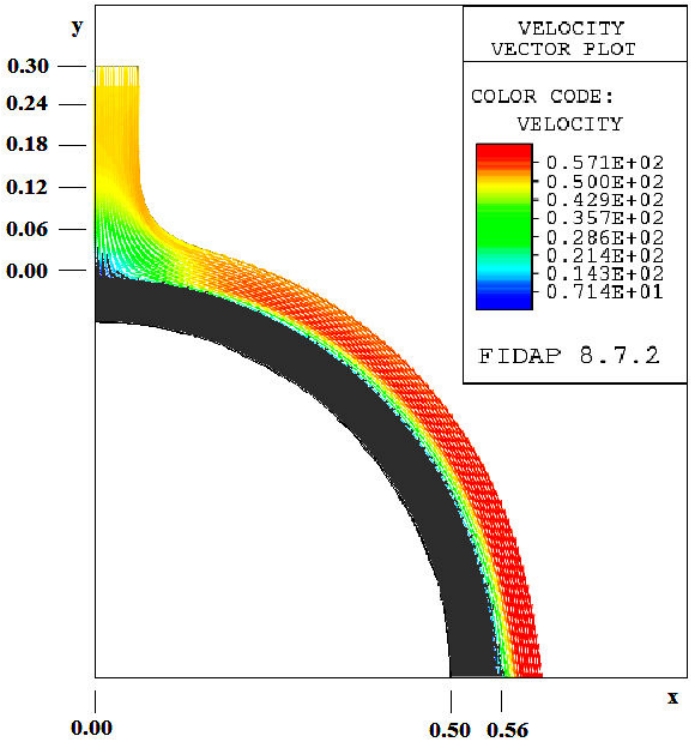

Figure 4.1 Velocity Vector Distribution for a Silicon Curved Plate with Water as the Cooling Fluid (Re = 750, b= 0.60 mm, Q = 5.665×10^{-7} m^3/s, β = 2.5, H_n = 0.3 cm, q = 250 kW/m^2)

Fig. 4.2 shows the free surface height distribution for different Reynolds numbers when the jet strikes the curved plate's surface. It can be seen that the fluid spreads out moving along the outer surface of the curved plate. As the Reynolds number increases, the free surface increases in thickness due to higher flow rate. In addition, a higher Reynolds number causes a higher rebounding velocity of the fluid particles at the impact that also contributes to a higher film thickness, particularly near the impingement region. For the conditions considered in the present investigation, the flow was supercritical and no hydraulic jump was present.

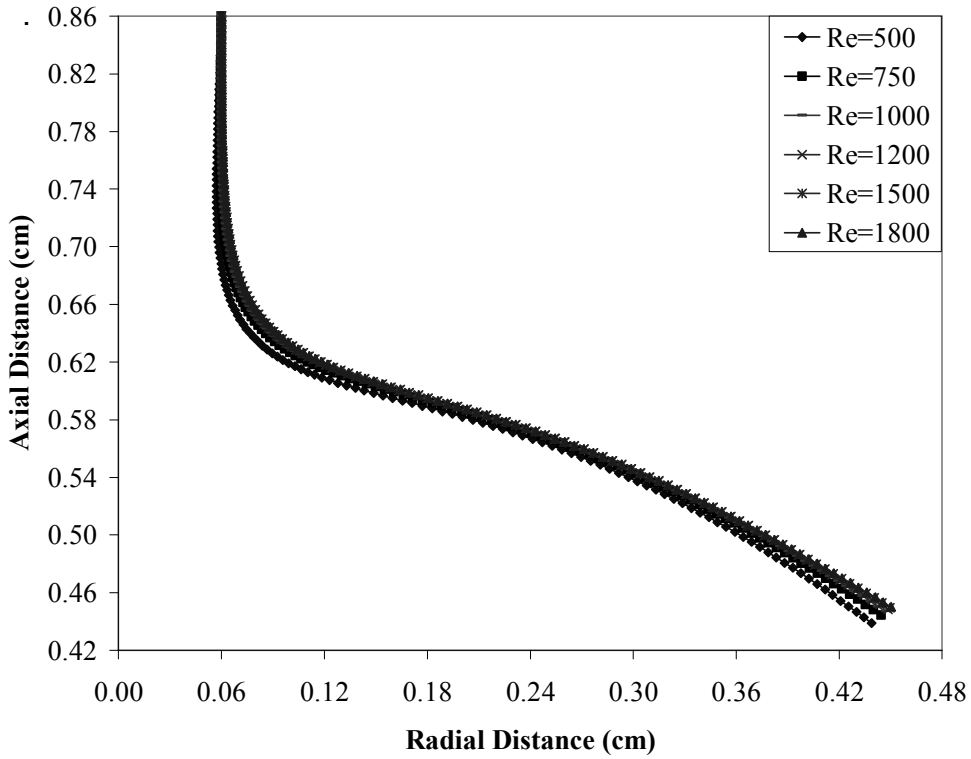

Figure 4.2 Free Surface Height Distribution for Different Reynolds Numbers and Water as the Cooling Fluid (b=0.60 mm, β=2.0, H_n=0.30 cm, q=250 kW/m^2)

Figures 4.3 and 4.4 show dimensionless interface temperature and local Nusselt number distributions as a function of dimensionless distance (s/d_n) along the solid-fluid interface at different Reynolds numbers. The curves in Figure 4.3 reveal that the dimensionless interface temperature decreases with jet velocity or Reynolds number. The dimensionless interface temperature has the lowest value near the stagnation point (underneath the jet opening) where the fluid particles start to move along the disk surface (after the impingement process) and increases along the arc length reaching the highest value at the end of it. This also shows that an increasing Reynolds number contributes to a more effective cooling by the enhancement of convective heat transfer coefficient.

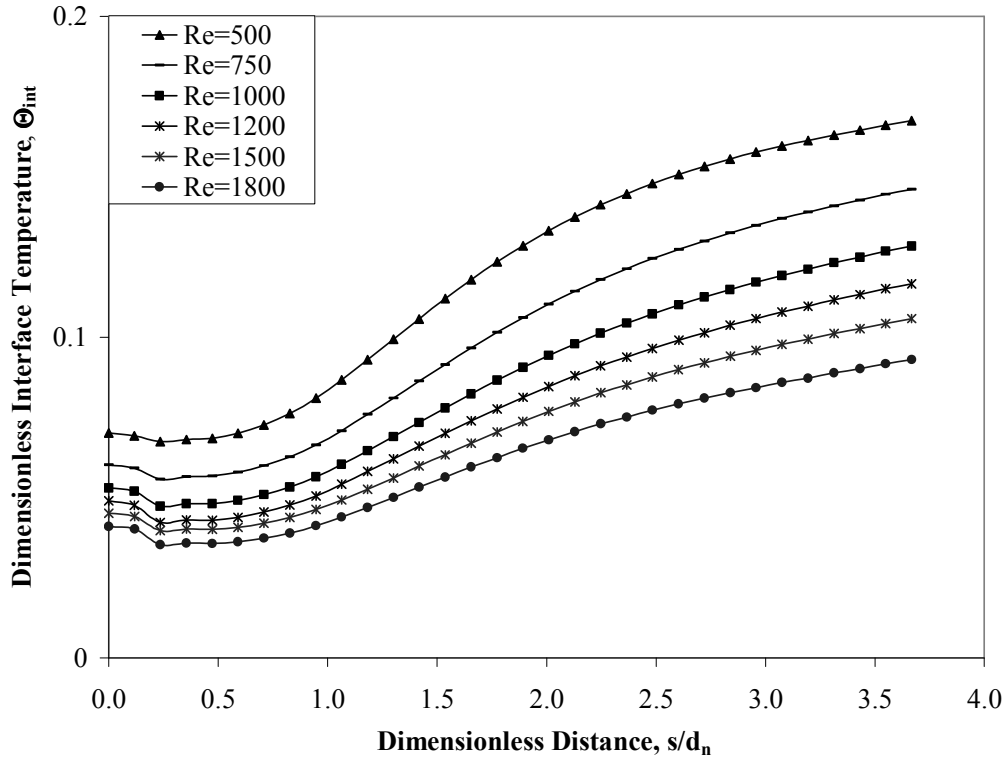

Figure 4.3 Dimensionless Interface Temperature Distribution for a Silicon Curved Plate at Different Reynolds Numbers and Water as the Cooling Fluid (β=2.5, H_n= 0.30 cm, b=0.60 mm, q=250 kW/m^2)

The local Nusselt number shown in Figure 4.4 increases rapidly over a small distance measured from the stagnation point (core region), reaches a maximum around s/d_n = 0.23, and then decreases along s as the boundary layer develops further downstream. The location of the maximum Nusselt number can be associated with the transition of the flow from the vertical impingement to displacement along the disk surface where the boundary layer starts to develop. Figure 4.4 also confirms that an increasing Reynolds number contributes to a more effective cooling by the enhancement of convective heat transfer coefficient. The local Nusselt number increased very significantly all along the plate surface with the increase of Reynolds number.

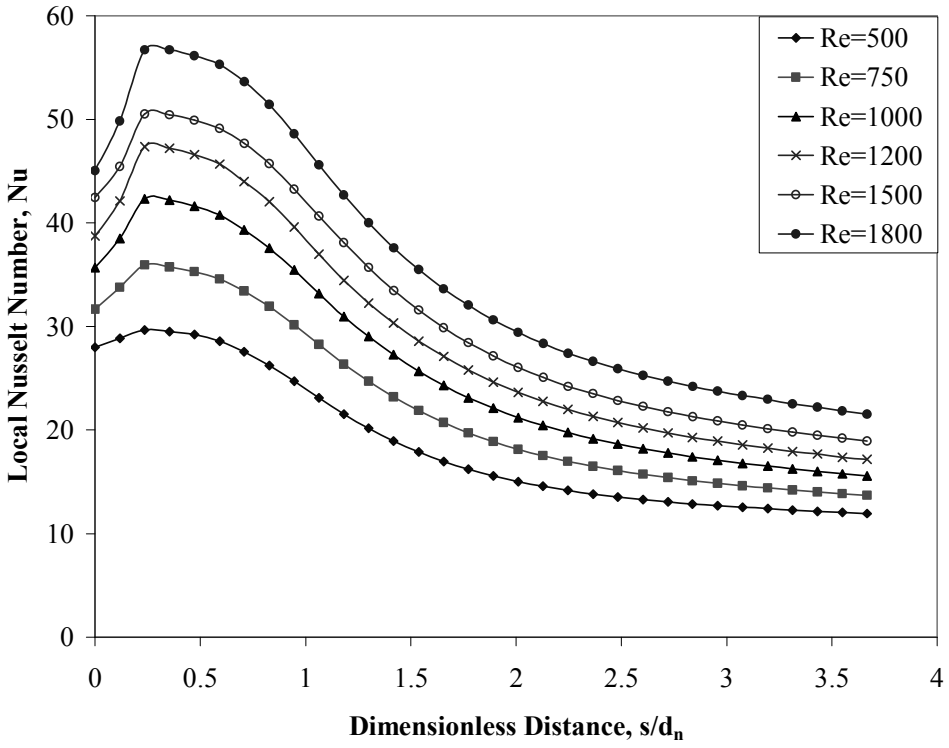

Figure 4.4 Local Nusselt Number Distribution for a Silicon Curved Plate at Different Reynolds Numbers and Water as the Cooling Fluid (β =2.5, H_n=0.30 cm, b=0.60 mm, q=250 kW/m^2)

Figure 4.5 plots the average Nusselt number (Nu_{av}) and maximum temperature in the solid (Θ_{max}) as a function of Reynolds number. It may be noted that average Nusselt number increases with Reynolds number and maximum temperature within the solid decreases with increasing Reynolds number. The maximum temperature happens at the outer edge of the plate adjacent to the inner surface which is heated. As the flow rate (or Reynolds number) increases, the magnitude of fluid velocity near the solid-fluid interface that controls the convective heat transfer rate increases. That results in lowering of the maximum temperature. The control of maximum temperature may be crucial in the thermal management of electronic equipment.

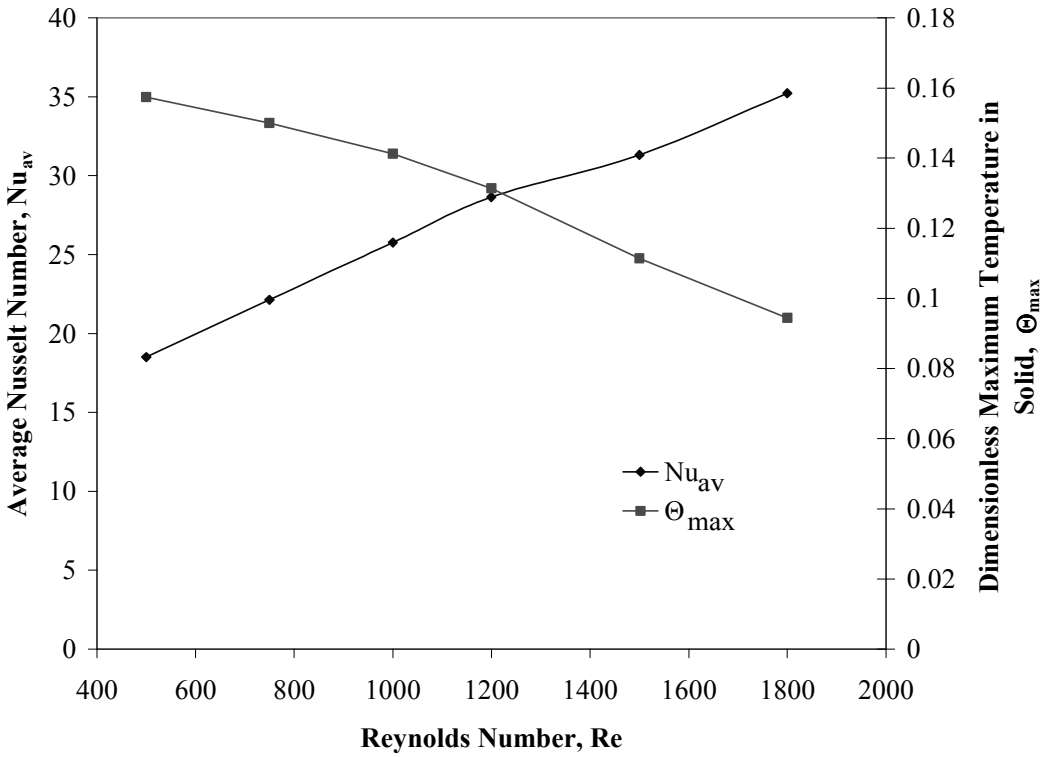

Figure 4.5 Average Nusselt Number and Maximum Temperature Within the Solid for Different Reynolds Numbers for Constant Heat Flux Conditions (q = 250 KW/m^2, β=2.5, H_n = 0.30cm)

The solid-fluid dimensionless interface temperature and local Nusselt number distributions for six different nozzle-to-target spacing for water as the cooling fluid and Reynolds number of 750 are shown in Figures 4.6 and 4.7 respectively. As the curved plate surface gets closer to the nozzle (smaller nozzle-to-target spacing ratio), the temperature at the solid- fluid interface decreases due to higher jet momentum at impingement that causes higher velocity of fluid particles adjacent to the plate enhancing the heat transfer.

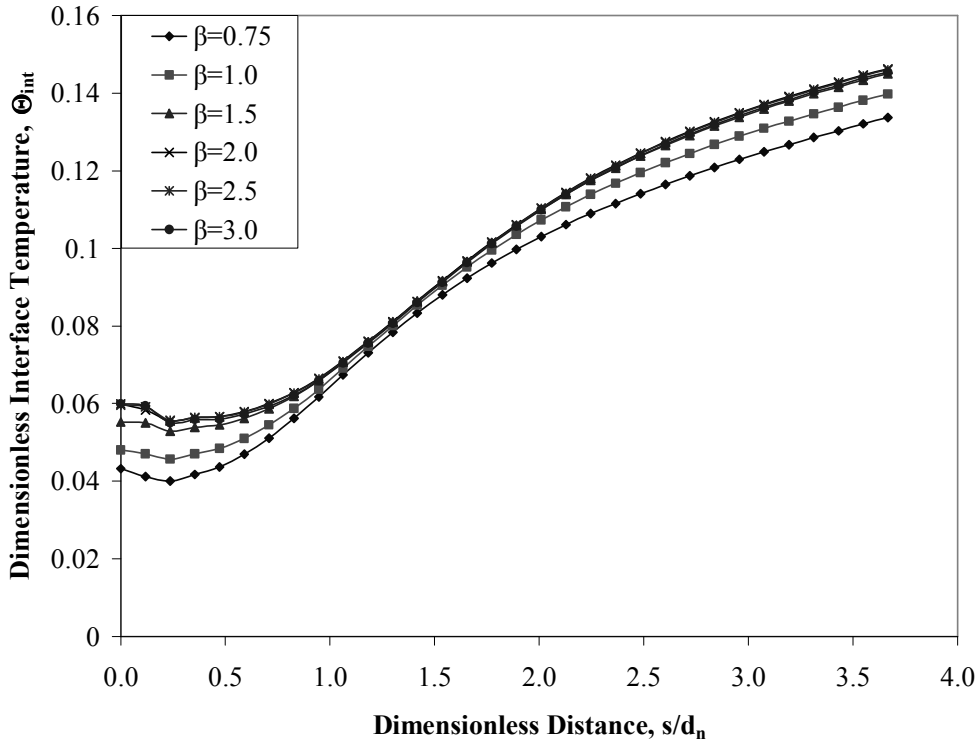

Figure 4.6 Dimensionless Interface Temperature for Silicon Curved Plate for Different Nozzle to Target Spacing Ratio (β) and Water as the Cooling Fluid (Re=750, d_n=1.2mm, b=0.60 mm, q=250 kW/m^2)

Therefore, in Figure 4.7, a higher Nusselt number is seen all along the arc length. It can be noticed that the impingement height affects the Nusselt number more at the stagnation region and the early part of the boundary layer region. At larger arc length the values are in a small range for all impingement heights. This is quite expected since the jet momentum more strongly affects the areas subjected to direct impingement. It can be also noticed that no significant change is seen at heights higher than β=2, where impingement height does not play a strong role in determining the convective heat transfer process.

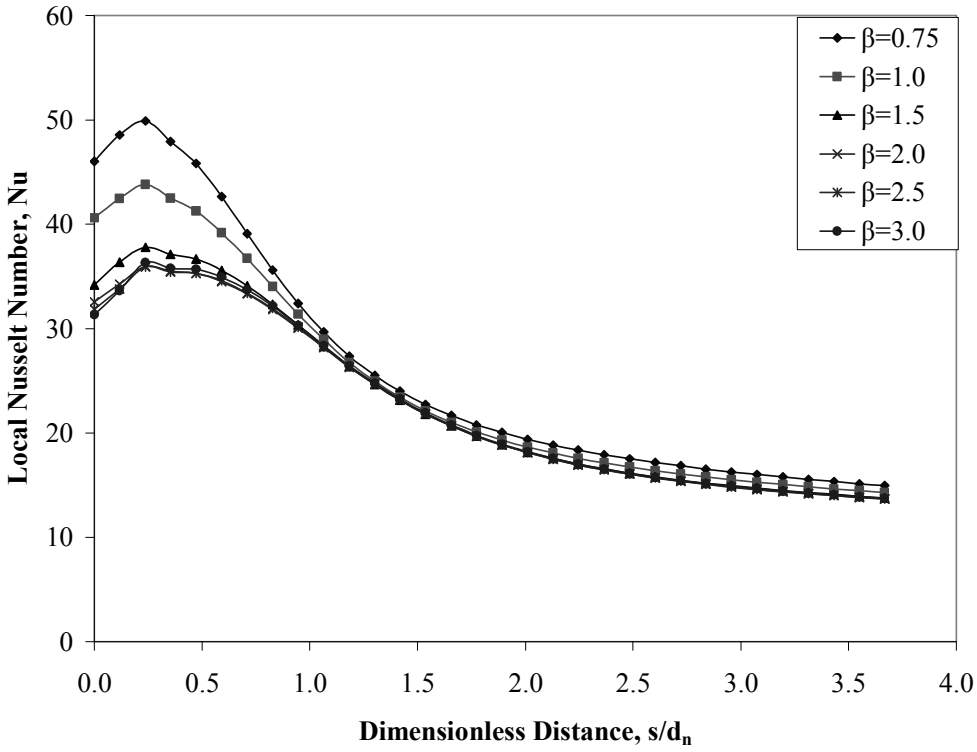

Figure 4.7 Local Nusselt Number Distribution for Silicon Curved Plate for Different Nozzle to Target Spacing Ratio (β) and Water as the Cooling Fluid (Re=750, d_n=1.2mm, b=0.60mm, q=250kW/m^2)

Therefore, in Figure 4.7, a higher Nusselt number is seen all along the arc length. It can be noticed that the impingement height affects the Nusselt number more at the stagnation region and the early part of the boundary layer region. At larger arc length the values are in a small range for all impingement heights. This is quite expected since the jet momentum more strongly affects the areas subjected to direct impingement. It can be also noticed that no significant change is seen at heights higher than β=2, where impingement height does not play a strong role in determining the convective heat transfer process.

The effects of varying the inner radius of curvature of the impingement plate are demonstrated in Figures 4.8-4.10. Figure 4.8 shows the dimensionless

solid-fluid interface temperature of water flowing on the curved plate with different R_i/d_n as a function of dimensionless distance (s/d_n). The corresponding distribution for a flat plate (infinite radius of curvature) is also shown for comparison. In order to keep the same energy input to the plate in these runs, the value of arc length s was kept constant. Therefore, half cylindrical plate (shown in Fig. 1) was possible only for the smaller radius of curvature (R_i/d_n=4.16). For other plates, the arc extended over an angle of ϕ_{max}that is less than $\pi/2$. For flat disk, s was same as its radius. It can be noticed that decreasing the inner plate radius of curvature to nozzle diameter ratio (R_i/d_n) decreases the dimensionless interface temperature.

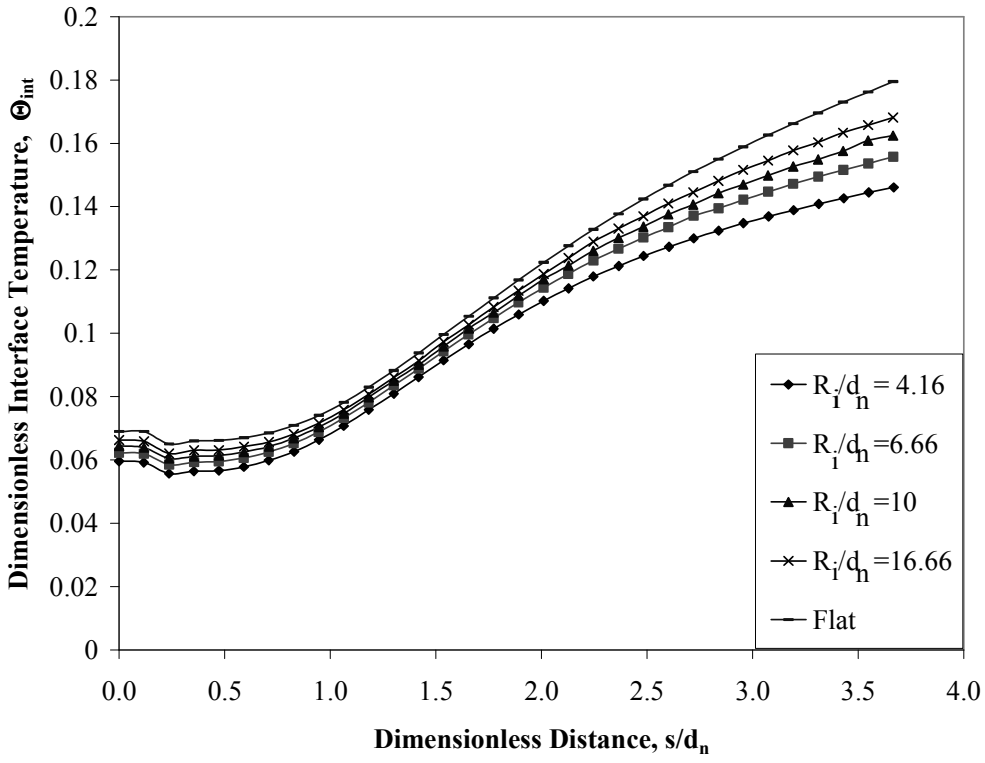

Figure 4.8 Dimensionless Interface Temperature for Silicon Curved Plate for Different Inner Plate Radius of Curvature to Nozzle Diameter Ratio (R_i/d_n) for Water as the Cooling Fluid (β =2.5 , H_n = 0.30 cm Re=750, d_n=1.2mm, b=0.60 mm, q=250 kW/m^2)

This is because the fluid particles are subjected to a larger gravitational force that increases the local fluid velocity near the solid-fluid interface and results in larger rate of convective heat transfer. Figure 4.9 plots the local Nusselt number distribution for different inner plate radius of curvature to nozzle diameter ratio (R_i/d_n) including a flat plate as a function of dimensionless distance (s/d_n). A higher Nusselt number is encountered when R_i/d_n diminishes increasing the cooling capacity of the fluid. For all cases, the maximum local Nusselt number is encountered at $s/d_n \approx 0.23$ and after that it decays monotonically. The trend in Figure 4.9 agrees with the results reported by Martin [39].

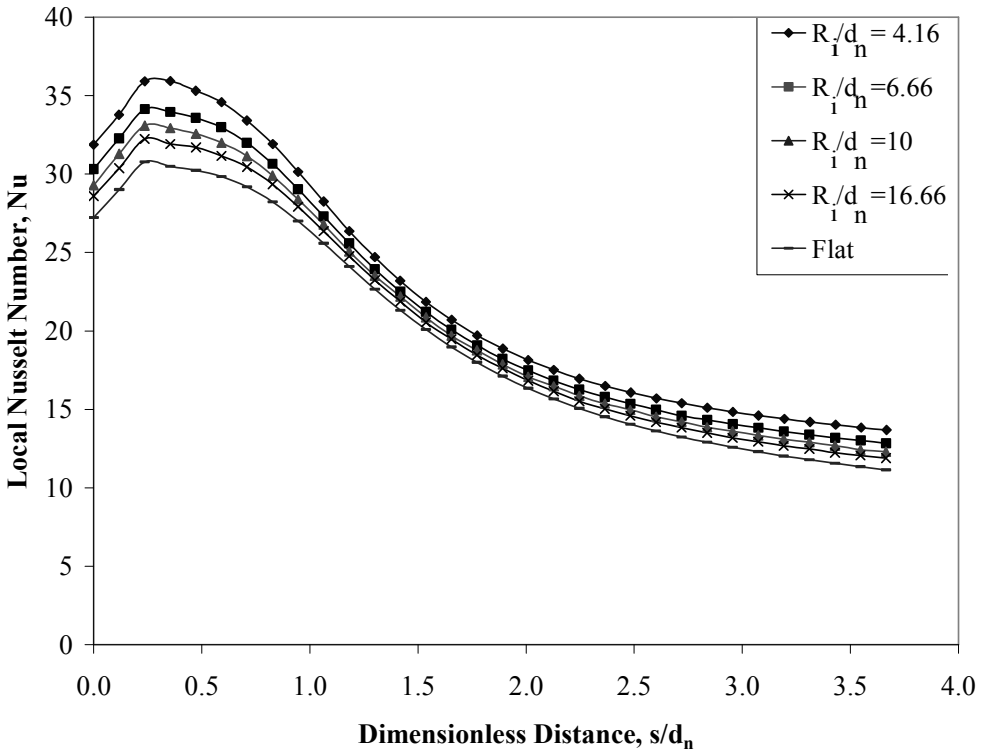

Figure 4.9 Local Nusselt Number Distribution for Silicon Curved Plate for Different Inner Plate Radius of Curvature to Nozzle Diameter Ratio (R_i/d_n) for Water as the Cooling Fluid (β =2.5 , H_n = 0.30 cm Re=750, d_n=1.2mm, b=0.60 mm, q=250 kW/m^2)

Figure 4.10 plots the average Nusselt number (Nu_{av}) and the maximum temperature within the solid (θ_{max}) as a function of the inner plate radius of curvature to nozzle diameter ratio (R_i/d_n). As expected, the average Nusselt number decreases with increasing inner radius of curvature and maximum temperature increases.

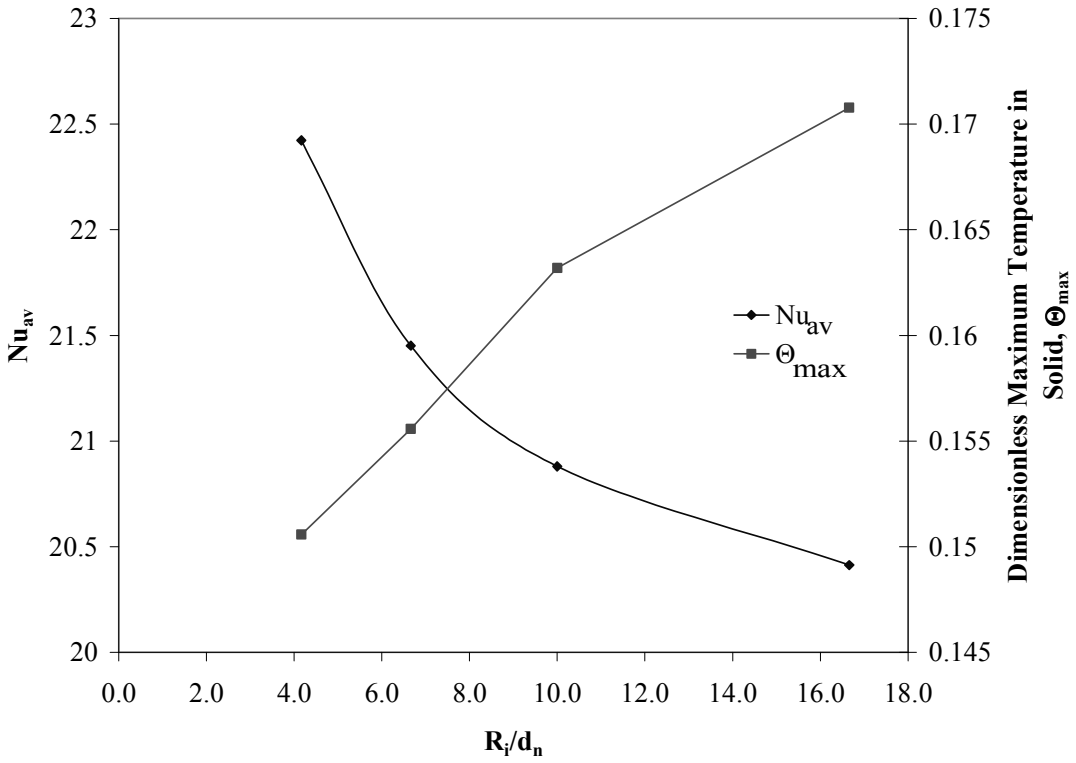

Figure 4.10 Average Nusselt Number and Maximum Temperature in the Solid Variations (Θ_{max}) for Silicon Curved plate for Different Inner Plate Radius of Curvature to Nozzle Diameter Ratio (R_i/d_n) for Water as the Cooling Fluid (β =2.5 , H_n = 0.30 cm Re=750, d_n=1.2mm, b=0.60 mm, q=250 kW/m^2)

Figure 4.11 presents the local heat transfer coefficient and Nusselt number distributions for different nozzle diameters (d_n) for a constant flow rate using water as the working fluid. When flow rate (or Reynolds number) is kept constant, a reduction in nozzle slot opening requires a proportional increase of jet

inlet velocity. A higher jet velocity essentially contributes to a higher fluid velocity near the solid-fluid interface and higher value of convective heat transfer coefficient. However, since the Nusselt number used the slot width as the length scale, increasing (d_n) results in a higher local Nusselt number along the solid-fluid interface.

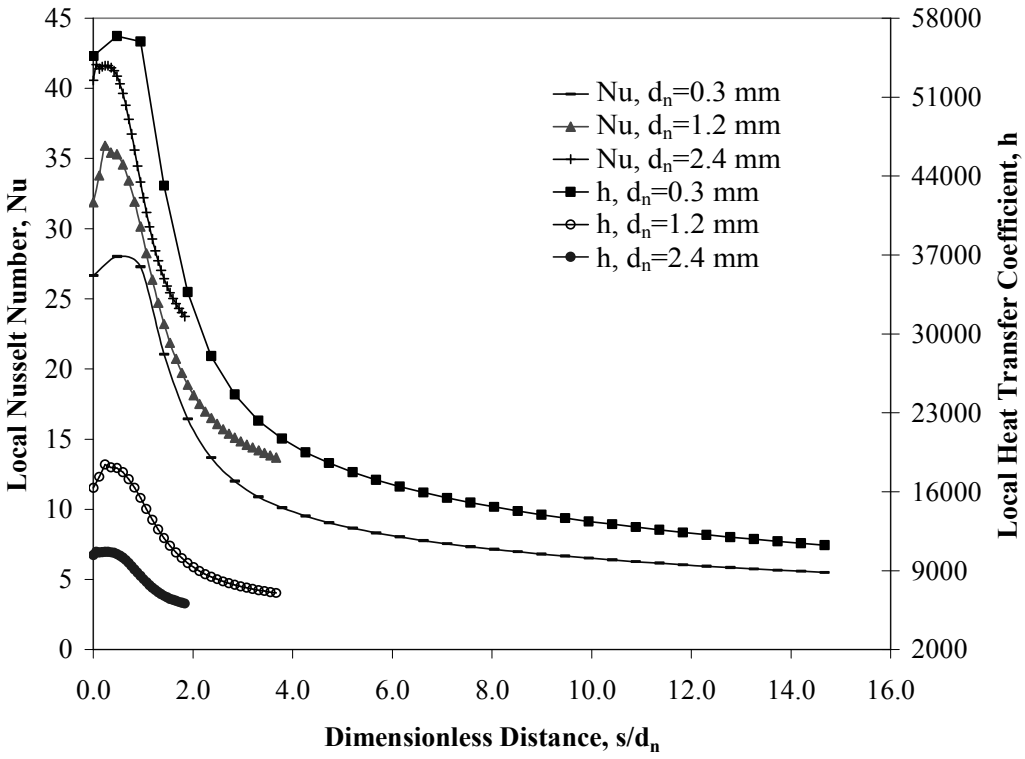

Figure 4.11 Heat Transfer Coefficient and Nusselt Number Distributions for Different Nozzle Slot Widths (Q=0.0006 m^3/s, β =2.5 , H_n = 0.30 cm β=2.5, Re=750, q=250 kW/m^2)

Figures 4.12 and 4.13 display the effects of varying plate thickness to nozzle diameter ratio (b/d_n) for a silicon plate using water as the cooling fluid. As the thickness increases, the temperature at the solid-fluid interface decreases and becomes more uniform due to a better distribution of heat within the solid by

conduction. It may be also noticed that the temperature is lower at the stagnation region and it increases as s/d_n increases all the way to the end of the plate. It can be also noted that a thinner plate provides a lower Nusselt number at the stagnation region but increases to provide higher maximum value and maintains a higher value as the fluid moves downstream along the curved plate. Thus, a thinner plate contributes to a more effective cooling by convection as opposed to a thicker plate.

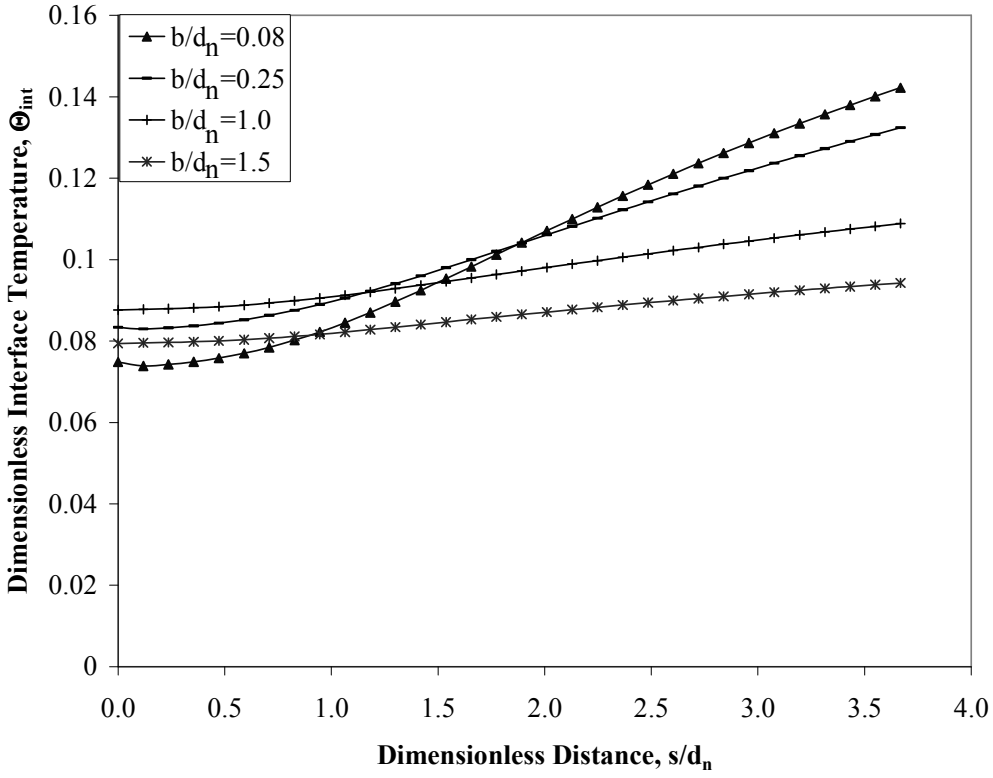

Figure 4.12 Dimensionless Interface Temperature for Different Plate Thicknesses (β =2.5, Re=750, d_n=1.2mm, q=250 kW/m^2)

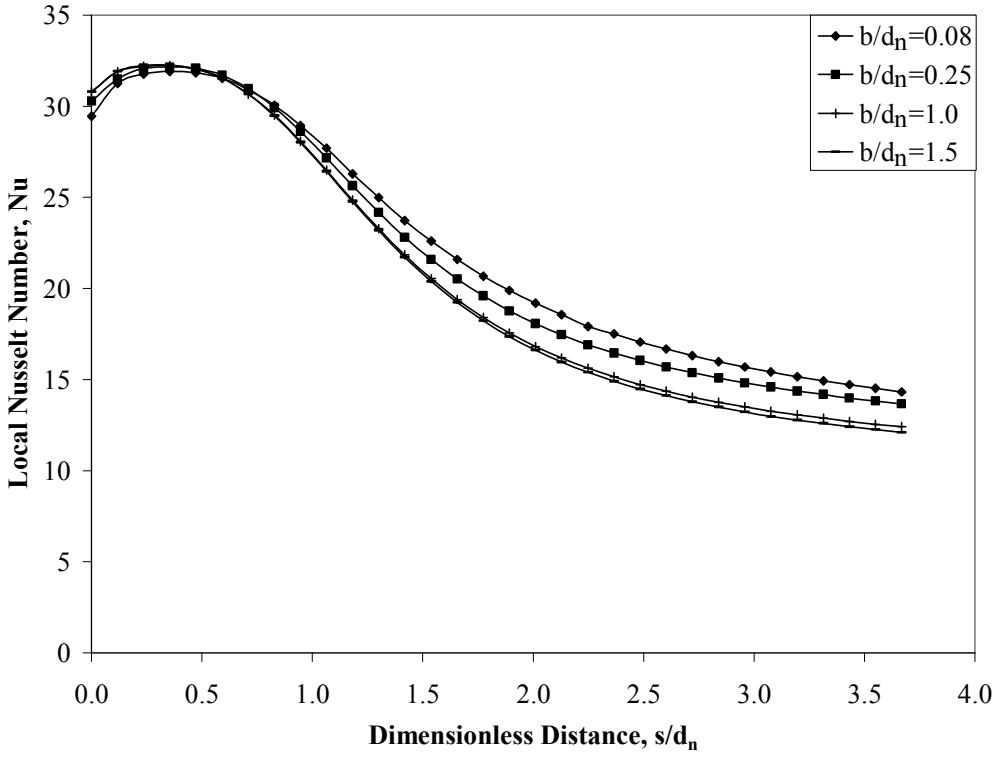

Figure 4.13 Local Nusselt Number Distribution for Different Plate Thicknesses (β =2.5, Re=750, H_n = 0.30 cm, q=250 kW/m^2)

Figure 4.14 presents the average Nusselt number (Nu_{av}) and maximum temperature (Θ_{max}) encountered within the solid as a function of (b/d_n). The maximum temperature within the solid occurs at the inner surface of the curved plate at its outlet end (maximum s or ϕ). It can be noticed that both average Nusselt number and maximum temperature within the solid diminish with increase of plate thickness. A lower average Nusselt number is a result of integrated local values seen in Figure 4.14, where a thicker plate provided a lower Nusselt number over a major portion of s/d_n. A lower maximum temperature for a thicker plate is a result of lower total heat input when plate

thickness was higher, as the heat flux at the inner surface of the plate and outer radius of the plate were kept constants in these simulations.

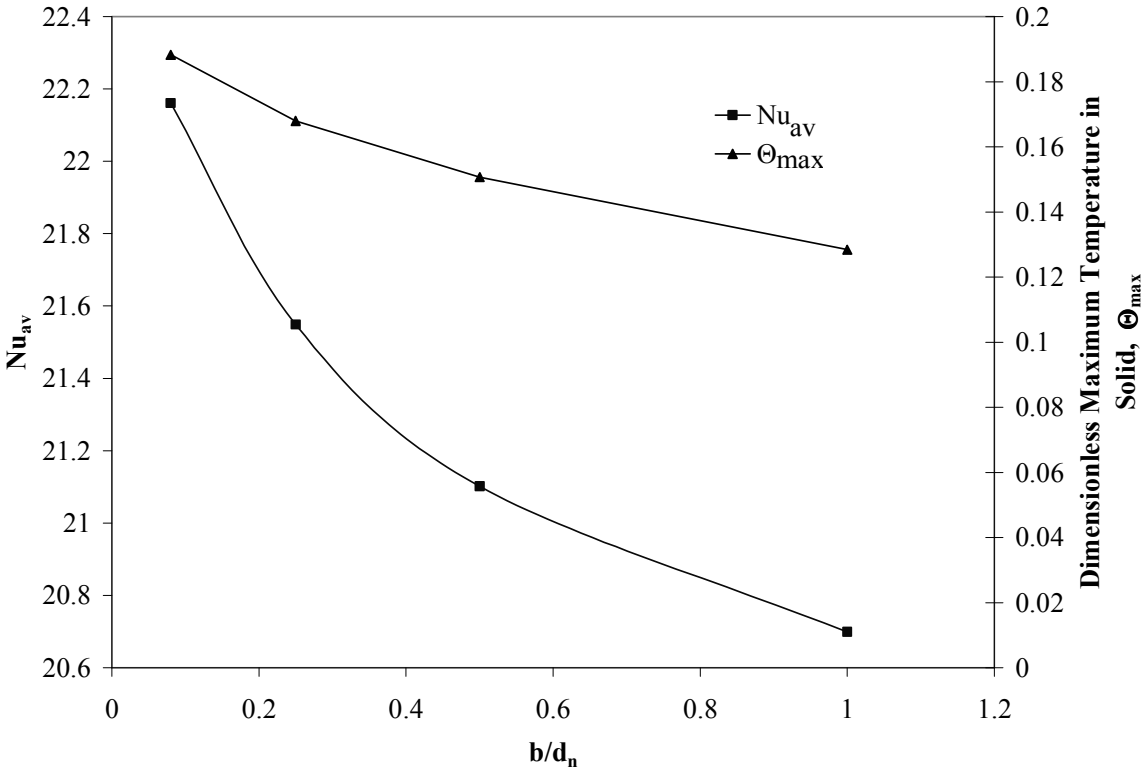

Figure 4.14 Average Nusselt Number and Maximum Temperature in the Solid Variations with Plate Thickness (β =2.5, Re=750)

Figure 4.15 compares the dimensionless solid-fluid interface temperature for the present working fluid (water) with two other cooling fluids flouroinert (FC-77) and oil (MIL-7808). Water (T_J=310.15 K) presents the highest dimensionless interface temperature when compared to FC-77 (T_J=310.15 K) and MIL-7808 (T_J=375 K). This trend is well correlated with Prandtl number. A higher Prandtl number results in lower dimensionless temperature at the solid-fluid interface. In addition, due to lower thickness or smaller growth rate of thermal boundary layer at higher Prandtl number, a low temperature is maintained over a larger portion

of the plate resulting in better cooling performance. Figure 4.16 displays the local heat transfer coefficient and local Nusselt number for these three fluids. A higher Nusselt number distribution is encountered when MIL-7808 is used as the working fluid in comparison with FC-77 (q=50 kW/m^2) and water.

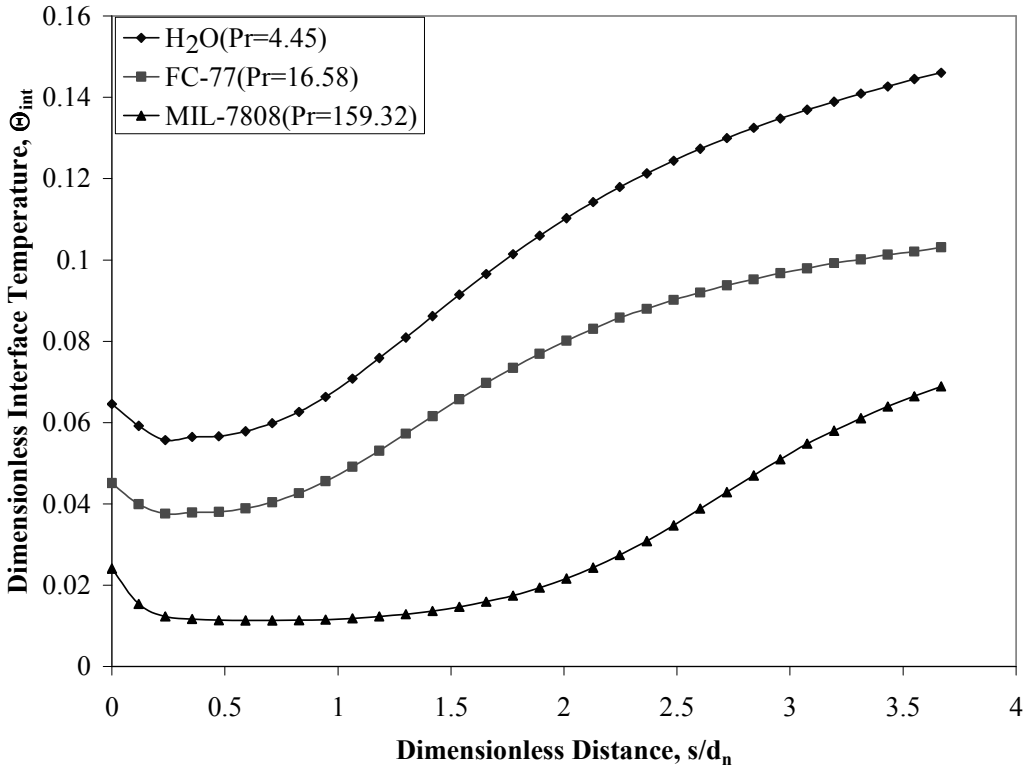

Figure 4.15 Dimensionless Interface Temperature for Different Cooling Fluids (β=2.5, Re=750)

As expected, a higher Nusselt number is obtained for a higher Prandtl number fluid. However, when dimensional heat transfer coefficient is considered, the Prandtl number alone cannot correlate the trend. The highest heat transfer coefficient is still provided by MIL-7808 at the impingement region. However, the curves for MIL-7808 and water cross each other and at large values of s, the

highest heat transfer coefficient is obtained for water. FC-77 (k_f =0.06299 W/m K) gives much lower heat transfer coefficient compared to water or MIL-7808 because of its lowest thermal conductivity. These results were obtained for a constant Reynolds number of 750.

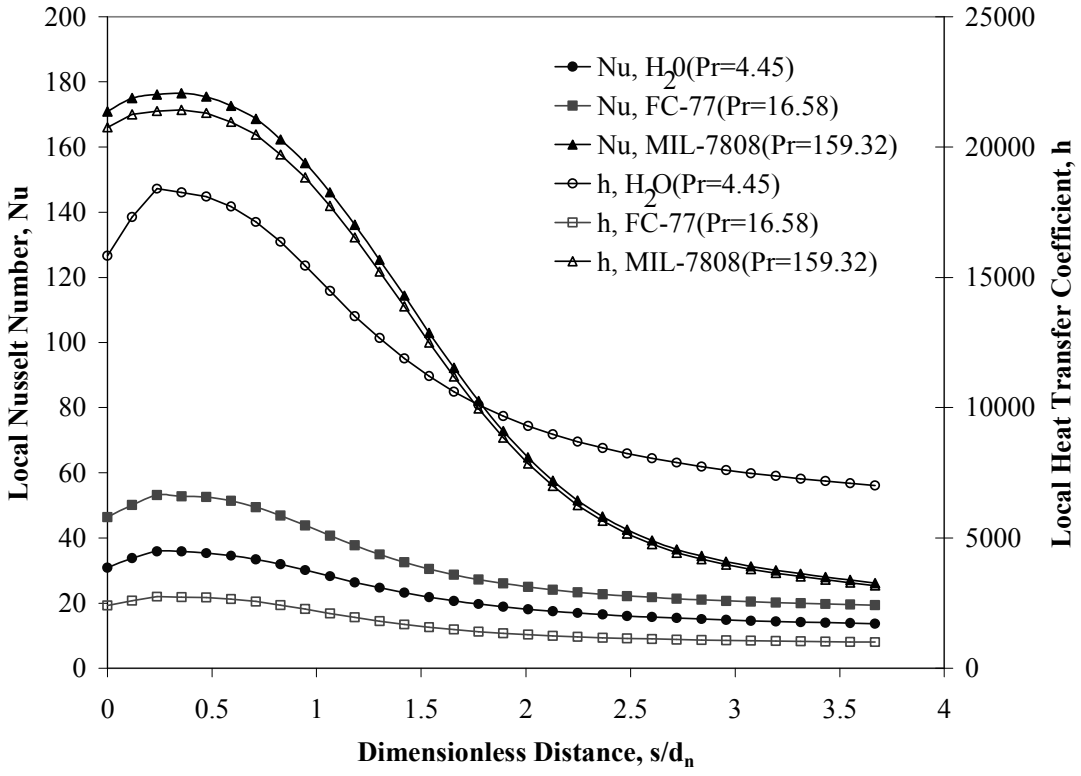

Figure 4.16 Heat Transfer Coefficient and Nusselt Number Distributions for Different Cooling Fluids (Re=750, β=2.5)

One of the papers used for the validation of this numerical study was the experimental work carried out by Bartoli and Faggiani [21] where water was used for the cooling of a stainless steel hollow cylinder by jet impingement. The numerical simulation attempted to duplicate the exact conditions of this experiment. A steady state mixing length turbulence model was employed for

this simulation. The parameters used and their corresponding values according to Bartoli and Faggiani [21] were the following: Re=3500–20,000, T_J=293.15–323.15 K, Pr=3.57–6.99, q=50 kW/m^2, ϕ=0°-90°, β=5.5, and b=0.5 mm. Figure 4.17 compared the results obtained in the numerical simulation with the correlation proposed by Bartoli and Faggiani [21] for Nu/Pr$^{0.4}$. The difference is 3.60% at Re= 3,500 and 1.88% at Re= 15,000.

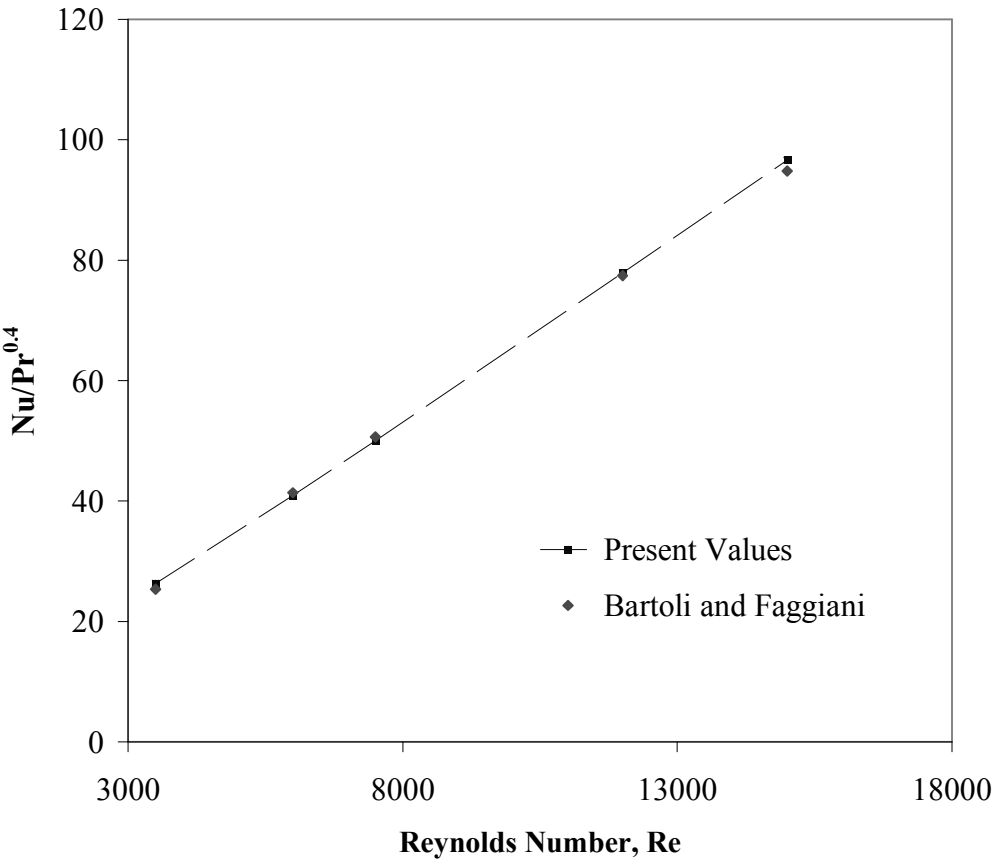

Figure 4.17 Local Nusselt Number Compared with Bartoli and Faggiani [21] at Different Reynolds Numbers (ϕ=90°, d_n=2.0 mm, b=0.50 mm, q=50 kW/m^2)

Numerical simulations were also carried out to compare with the results obtained by Gori and Bossi [29] on the cooling of a hollow stainless steel circular cylinder by a turbulent flow of air from a slot nozzle. The numerical model tried to mimic the experimental set up that the authors used to obtain the desired outcome for a constant heat flux condition. In addition, a correlation suggested by Whitaker [40] for uniform fluid flow was also used for comparison.

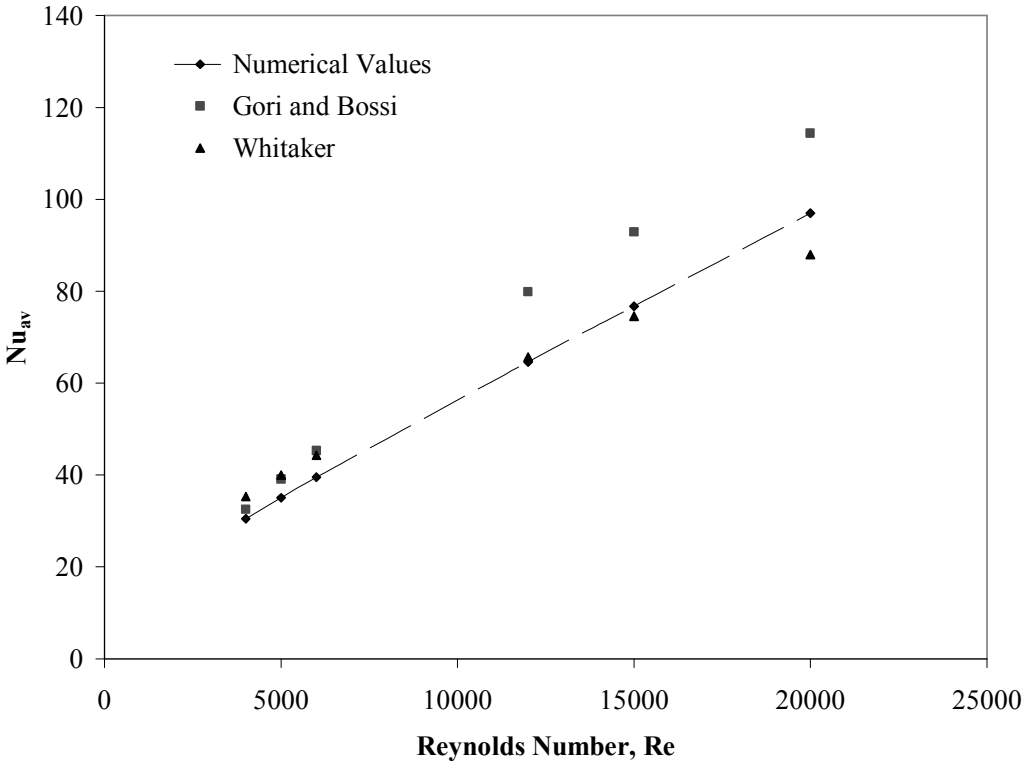

Figure 4.18 Average Nusselt Number Compared with Gori and Bossi [29] and Whitaker [40] for Different Reynolds Numbers (d_n=2.5 mm, b = 0.2 mm, q=2.35 kW/m^2)

Figure 4.18 illustrates the numerical results obtained in the simulation compared to the experimental data obtained by Gori and Bossi [29] along with

the correlation proposed by Whitaker [40]. The values used during the simulation included a Reynolds numbers range of 4000-20,000, a fluid inlet (jet) temperature (T_J) of 293.15–296.15 K, the fluid Prandtl number (Pr) of 0.711–0.712, a constant heat flux (q) of 2.35 kW/m^2, an azimuthal angle (ϕ) of 0°-90°, a fixed dimensionless nozzle to target spacing ratio (β) of 8.0, and a fixed thickness (b) of 0.2 mm as specified by the authors.

The difference of the numerical simulation and the experimental results obtained by Gori and Bossi [29] was between 6.80%-23.77% with an average difference of 15.92%. The correlation proposed by Whitaker compared within a range of 1.76%-15.82% with an average difference of 9.31%. Considering the uncertainly of experimental data and the discretization and round-off errors inherent in numerical simulation, both of these comparisons may be considered to be quite satisfactory.

4.2 Transient Heating

The local heat flux variation along the solid-fluid interface for different time intervals is shown in Figure 4.19. Since an initial isothermal condition was assumed at the beginning of the process, the interfacial heat flux is zero at t=0 s. As expected, the heat flux at the solid-fluid interfaces increases with time. A much larger heat flux is seen at the stagnation region since the cold fluid at the jet strikes that region and keeps the minimum temperature at that location. This behavior occurs due to the constant renewal of cold fluid to dissipate the heat. The heat dissipated is utilized to rise the temperature of the solid as well as the

fluid and reduces thermal storage within the solid due to convective heat transfer. Another maximum heat flux is encountered around s/d_n=0.5, and then it decreases downstream. This can be explained as the transition of the fluid from the vertical impingement to a thin film flow along the curved surface where the boundary layer starts to develop. This crest can be associated with the start of the thermal boundary layer in the thin film structure. Figure 4.19 also presents $q_{av,int}\, r_o^2/q_w r_i^2$ which is the ratio of the energy transmitted to the fluid to the energy input at the bottom face of the plate. The interfacial heat flux reaches within 1% of the steady-state equilibrium condition at F_o= 0.103.

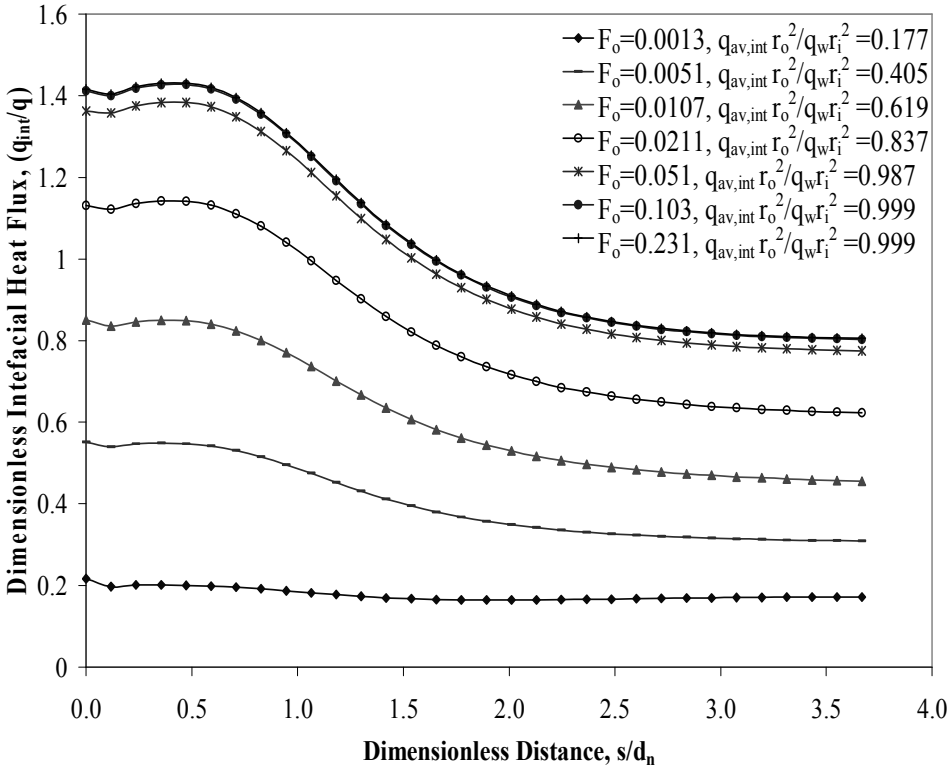

Figure 4.19 Dimensionless Local Heat flux Variation at the Solid-Fluid Interface for Silicon Plate at Different Time Instants (Re=750, b/d_n=0.5, ß=2.5)

Figure 4.20 shows the dimensionless interface temperature for different time instants. As can be observed at the very beginning of the heat transfer process, the solid-fluid interface keeps a uniform temperature compared to that when approaching steady-state equilibrium condition. This pattern is due to the thermal storage in the fluid necessary to develop the thermal boundary layer since an isothermal condition was present at the beginning of the problem. As time goes on, the thickness of the thermal boundary layer increases and therefore the temperature rises. Figure 4.20 also illustrates the difference of maximum-to-minimum temperature at the interface being the maximum situated at the outer edge of the plate and the minimum at the stagnation point of the plate due to the constant renewal of cold fluid from the nozzle. Thus, such temperature difference increases with time as more heat flows throughout the solid and transmitted to the fluid. The range of temperature encountered at the solid-fluid interface increases with time and reaches a constant value at the steady state. Figure 4.21 plots the local Nusselt number variation along the solid-fluid interface at different time instants. The local Nusselt number is controlled by local temperature and heat flux at the solid-fluid interface. This means that all heat reaching the solid-fluid interface via conduction through the solid is more efficiently convected out as the local fluid temperature is low everywhere at the interface.

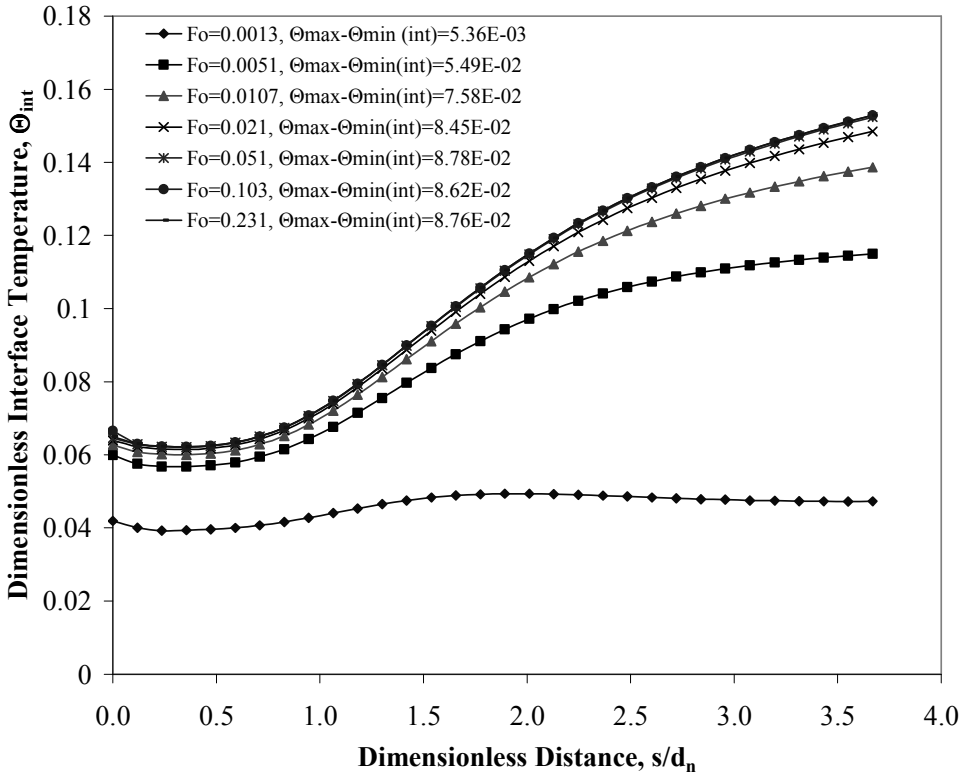

Figure 4.20 Dimensionless Interface Temperature Variation for Silicon Plate at Different Time Instants (Re=750, b/d_n=0.5, ß=2.5)

The local Nusselt number decreases with time until it reaches the steady-state equilibrium distribution. Figure 4.22 also provides the integrated average Nusselt number for the entire cylindrical shaped plate surface. As expected, the average Nusselt number is large at the early part of the transient and monotonically decreases with time all the way to the steady state condition. At this point, equilibrium conditions with the surroondings have been achieved between the plate and the fluid and the temperature of the plate along with the fluid becomes uniform. That is, $T_f=T_s$.

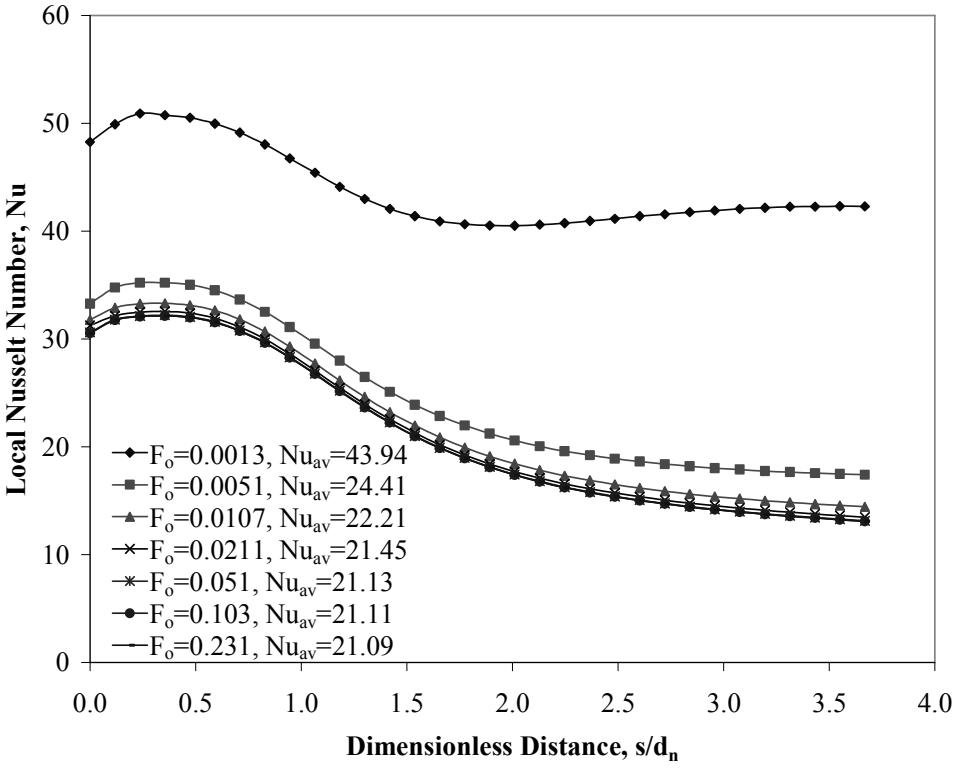

Figure 4.21 Local Nusselt Number Distribution for Silicon Plate at Different Time Instants (Re=750, b/d_n=0.5, ß=2.5)

Figure 4.22 shows results for dimensionless maximum temperature at the interface, maximum temperature in the solid, and maximum-to-minimum difference temperature at the interface for two different Reynolds numbers. The maximum temperature within the solid was found at the outlet plane next to the heated surface ($z=-r_o$, $r=r_i$). As expected, the temperature begins to rise with time as the solid plate begins to store heat starting after the specified initial condition (T_J=310 K) showing a rapid response at the earlier part of the heating process until its thermal storage capacity reduces up to its limit (steady-state).

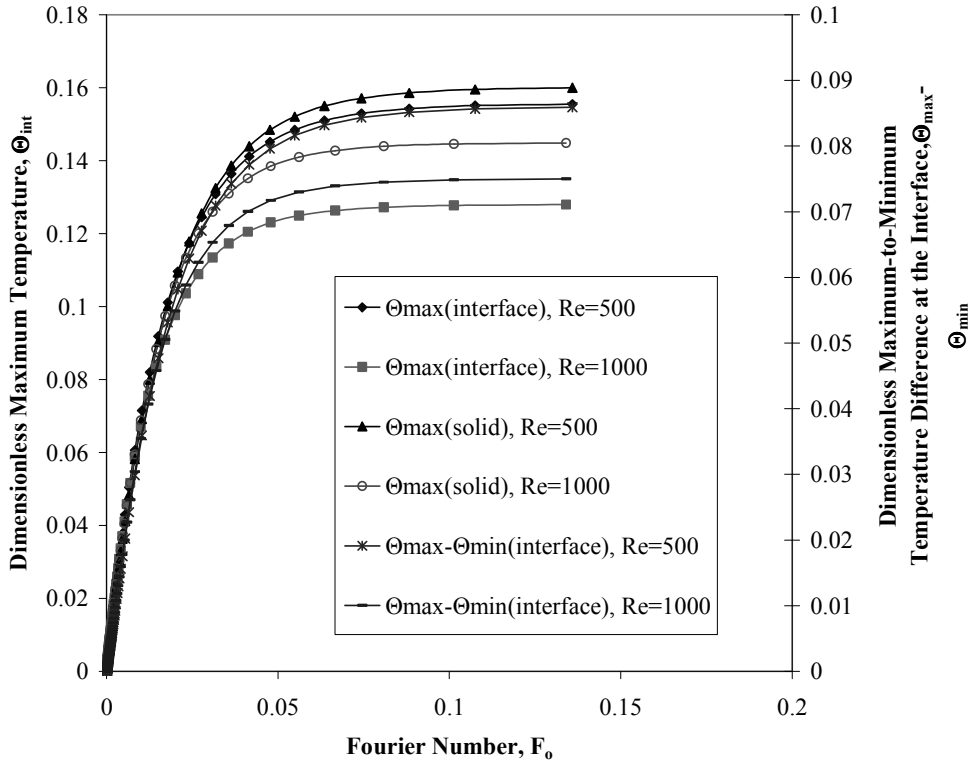

Figure 4.22 Distribution of Dimensionless Maximum Temperature at the Solid-Fluid Interface, within the Solid, and Maximum-to-Minimum Temperature Difference with Time for Two Reynolds Numbers (Silicon Plate, b/d_n=0.5, ß=2.5)

It is significant to point out that the time necessary to reach steady-state depends on the Reynolds number. Figure 4.22 also proves that a higher Reynolds number increases convective heat transfer and therefore lowers the plate's temperature. Figure 4.23 plots the average Nusselt number variation along the solid-fluid interface for two different Reynolds numbers over the entire transient start-up of the heat transfer process. As expected, the average Nusselt number becomes larger as the Reynolds number increases due to higher velocity of the fluid particles moving along the plate's outer surface, hence, increasing the rate of heat transfer.

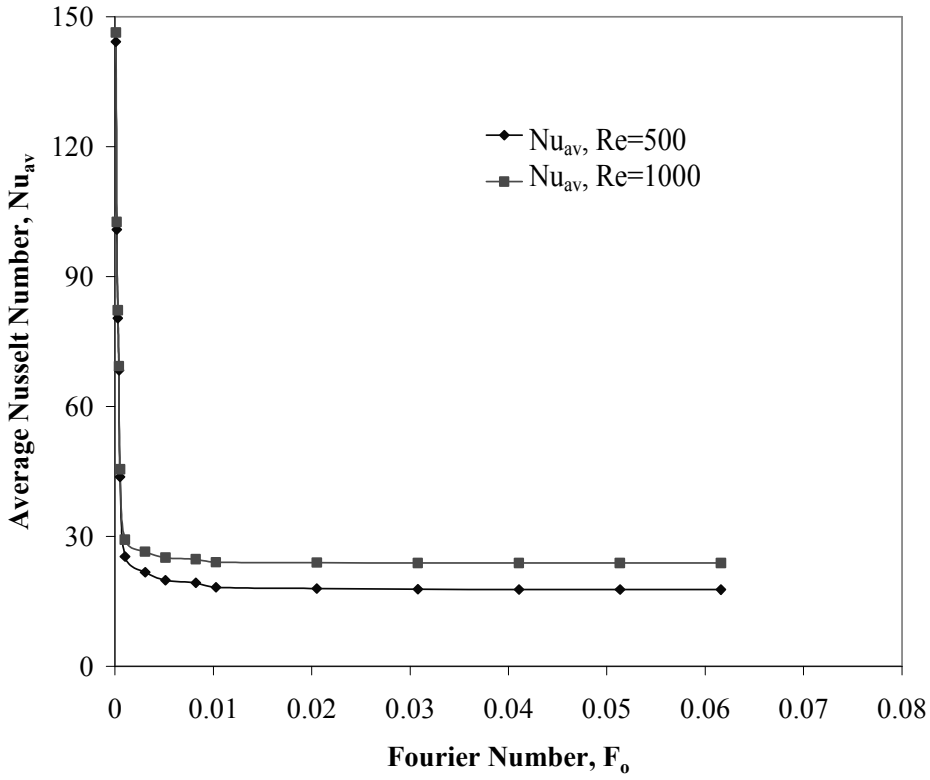

Figure 4.23 Variation of Average Nusselt Number with Time For Silicon Plate at Two Different Reynolds Numbers (b/d_n=0.5, ß=2.5)

The time required to reach steady-state for different Reynolds numbers is presented in Figure 4.24. Fo_{ss} was defined as the Fourier number at which the solid-fluid interface temperature everywhere on the solid plate reached within 0.001% of the steady equilibrium distribution. The time to reach thermal equilibrium condition decreases as the Reynolds number increases in value. This is due to more fluid flow rate available to carry away the heat and faster development of thermal boundary layer that is smaller in thickness.

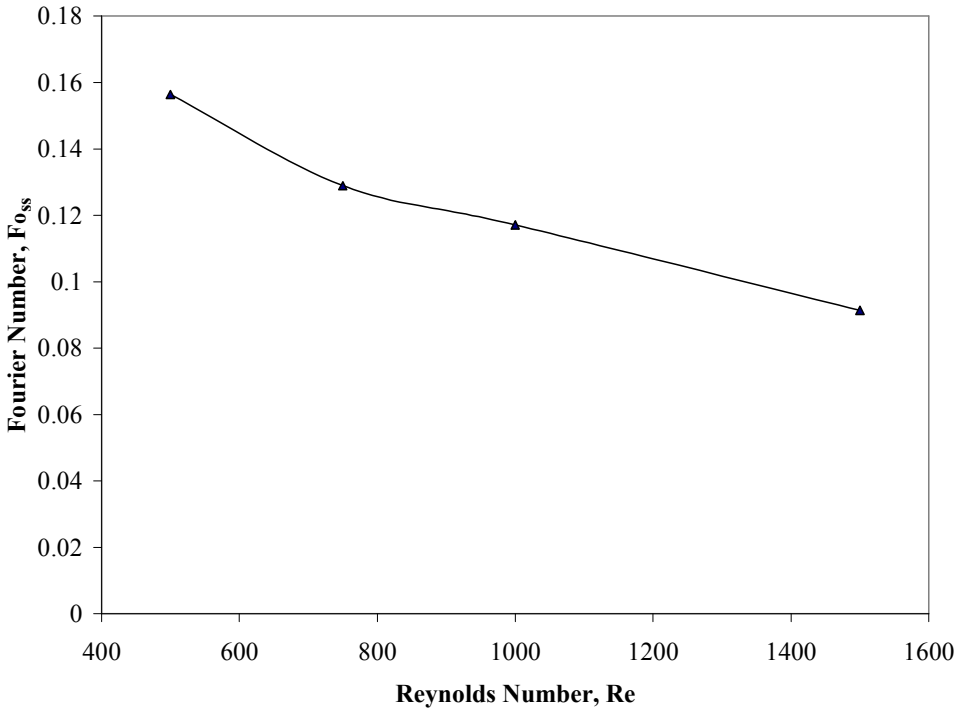

Figure 4.24 Time Required to Reach Steady-State for Silicon Plate at Different Reynolds Numbers (b/d_n=0.5, ß=2.5)

The effects of varying the thickness in the cylindrical plate on maximum temperature at the interface, maximum temperature within the solid, and maximum-to-minimum temperature difference at the interface can be seen on Figure 4.25. The plate thickness significantly affects the temperature distribution. It may be note that as the thickness of the solid plate increases, the time needed to achieve steady-state conditions increases. This is due to more storage capacity of heat within the solid. Similarly, the temperature at the solid-fluid interface remains lower due to higher thermal resistance of the solid to the path of heat flow.

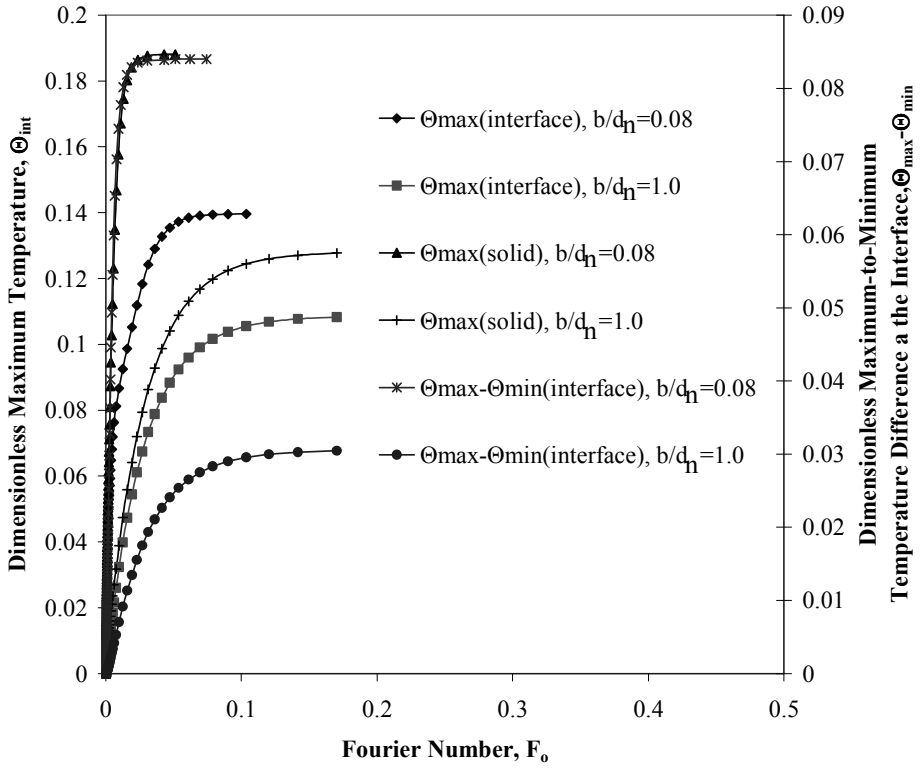

Figure 4.25 Distribution of Dimensionless Maximum Temperature at the Solid-Fluid Interface, within the Solid, and Maximum-to-Minimum Temperature Difference with Time for Different Plate Thicknesses (Silicon Plate Re=750, ß=2.5)

Figure 4.26 shows the average Nusselt number variation as a function of time for three distinct plate thicknesses using Constantan as the solid material. The average Nusselt number is higher for higher plate thickness. The maximum temperature at the solid-fluid interface, maximum temperature within the solid, and maximum to minimum temperature difference (as a measure for temperature non-uniformity) for different solid materials is presented in Figure 4.27.

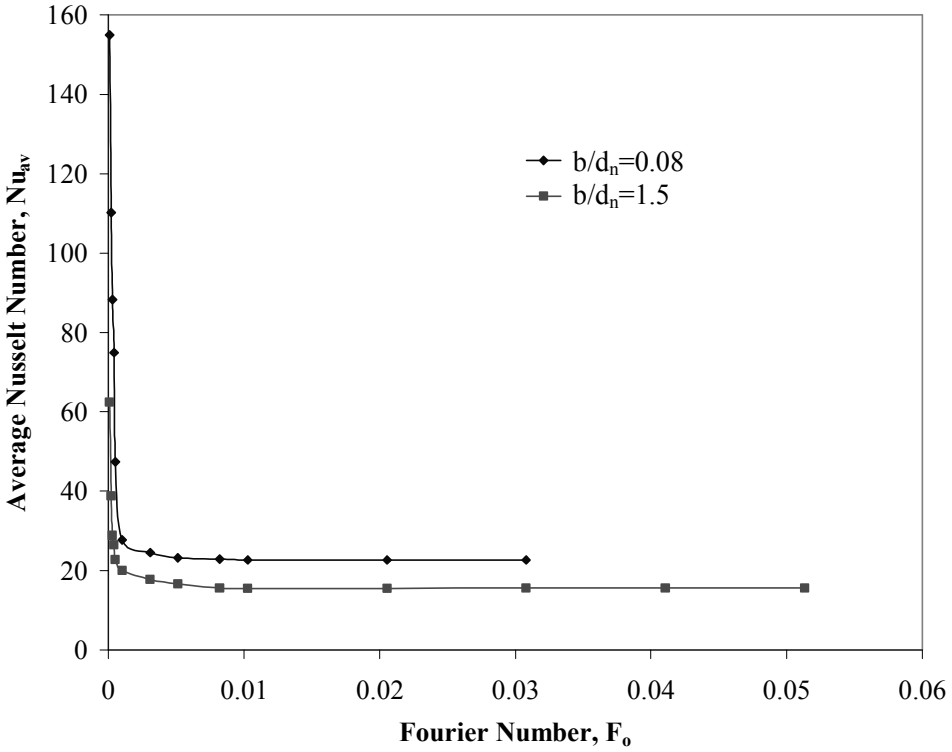

Figure 4.26 Variation of Average Nusselt Number with Time for Constantan Plate at Three Different Thicknesses (Re=750, ß=2.5)

As expected, the temperature changes occur faster at the beginning of the heating process for all materials and the slope gradually decays when the steady-state approaches. It can be observed that materials with a very low thermal conductivity such as Constantan maintains a higher temperature at the plate's outer surface and within the solid as the thermal conductivity controls how effective the heat flows and distributes throughout the material. The thermal diffusivity of the material also contributes to the transient behavior of the solid. As noticed, Silicon and Copper reach the steady-state faster than Constantan due to their higher thermal diffusivity, which controls the rate of heat being transferred through the solid material.

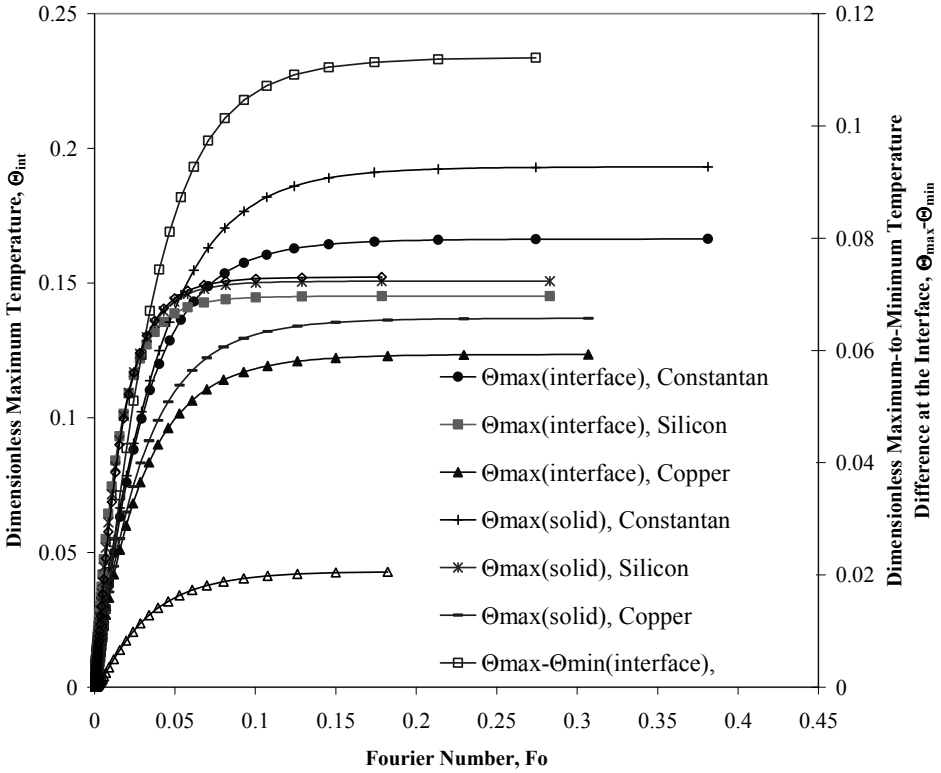

Figure 4.27 Distribution of Dimensionless Maximum Temperature at the Solid-Fluid interface, within the Solid, and Maximum-to-Minimum Temperature Difference with Time for Different Materials (Silicon Plate, Re=750, ß=2.5)

Figure 4.28 plots the distribution of average Nusselt Number with time for the three materials used in this study. Constantan shows a higher average heat transfer coefficient compared to Silicon or Copper over the entire transient process. A significant difference is seen at the earlier part of the transient and the curves come close together as the steady-state approaches. It will be also important to know how the materials responded in reaching thermal equilibrium based on their thickness.

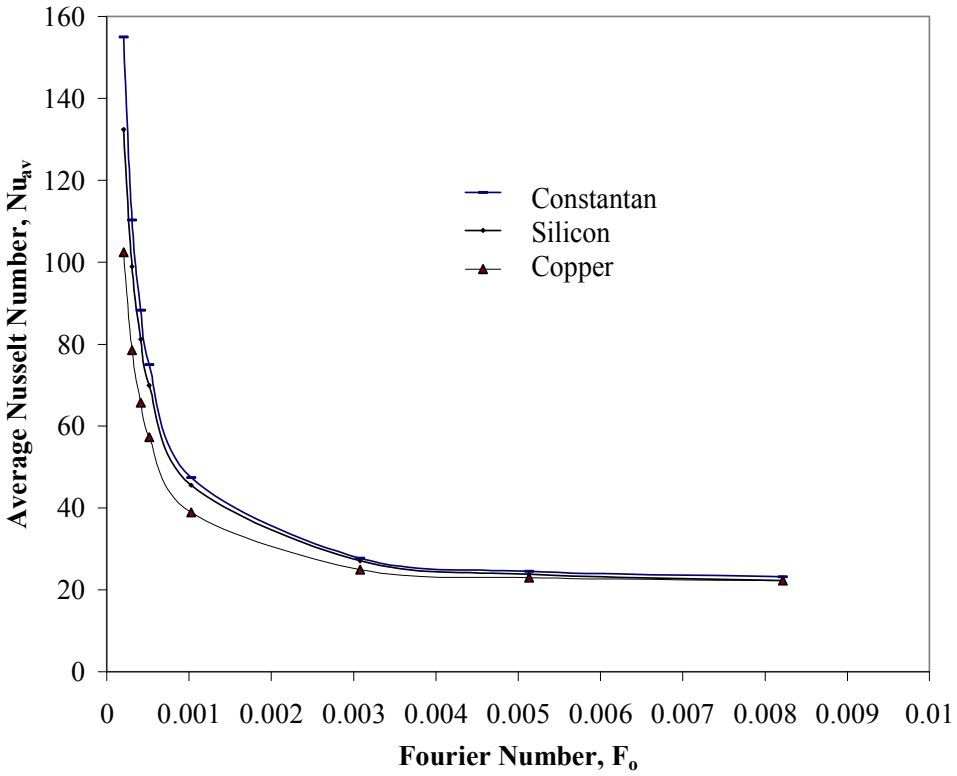

Figure 4.28 Variation of Average Nusselt Number with Time for Different Materials (Re=750, b/d_n,=0.5, ß=2.5)

Figure 4.29 presents Fo_{ss} for these materials for different plate thicknesses. As the thickness increases in value, the time to reach steady-state also increases. Constantan takes longer in reaching steady-state due to its lower thermal diffusivity compared to Copper and Silicon. Also, the property of the solid plays more significant role in determining the duration of the transient heat transfer process when the thickness is increased.

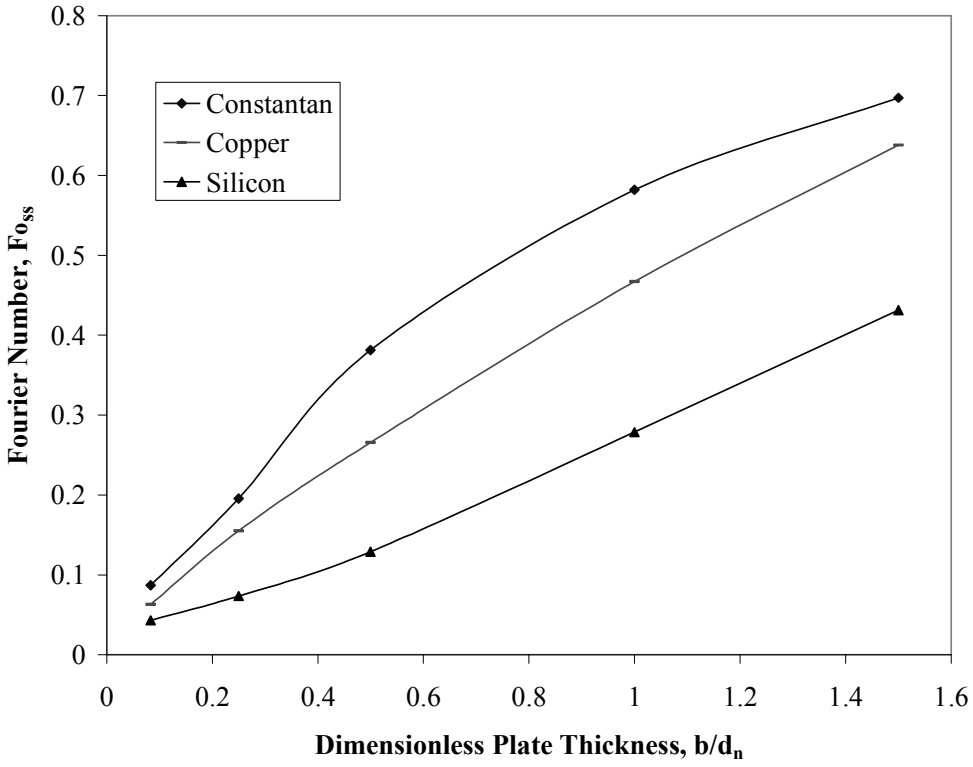

Figure 4.29 Time Needed to Reach Steady-State for Different Cylindrical Plate Thicknesses and for Different Materials (Re=750, ß=2.5)

Chapter 5 Discussion and Conclusion

Local and average Nusselt number and heat transfer coefficient distributions showed a strong dependence on the impingement velocity or Reynolds number. As the velocity increases, the boundary layer or film thickness decreases and Nusselt number increases over the entire solid-fluid interface. A lower thermal conductivity material showed higher local maximum Nusselt number as well as higher average Nusselt number among all studied materials. On the other hand, materials with higher thermal conductivity maintained a more uniform temperature distribution throughout the solid-fluid interface and facilitated a higher heat transfer rate, lowering the maximum temperature inside the hemisphere and at its interface. Also, increasing the thickness of the hemispherical plate proved to decrease the solid-fluid interface temperature due to the resistance of the material to heat flow. The Nusselt number, however, did not change much with thickness variation. The impingement height affected the dimensionless interface temperature as well as the Nusselt number. A higher jet impingement height provided a lower dimensionless interface temperature over the entire hemisphere and a higher Nusselt number at the stagnation region.

Temperature and heat flux at the solid-fluid interface rise with time whereas the average heat transfer coefficient decreases with time. A larger heat

flux is seen near the stagnation region because of the larger temperature difference between the water jet and the plate. The maximum dimensionless interface temperature was encountered at the outer edge of the cylindrical plate while the minimum was encountered at the stagnation region. Local Nusselt number is high near the stagnation region where convective heat transfer rate is more effective and then it decays monotonically along the remaining portion of the plate. The Reynolds number was found to be an essential parameter in controlling the transient process since the time required to reach steady state diminished as the Reynolds number increased. Also, the maximum temperature at the solid-fluid interface as well as the temperature inside the solid decreased as the Reynolds number increased while the maximum to minimum temperature difference a the interface decreased as the Reynolds number decreased. Increasing the plate thickness decreased the capacity of the plate of being effectively cooled (lower average Nusselt number) and decreased dimensionless maximum temperature at the interface and within the solid. The time required to reach steady-state became larger as the thickness of the plate increased. Materials with a higher thermal conductivity maintained a lower dimensionless solid-fluid interface temperature as well as dimensionless maximum temperature and reached steady-state faster. Nevertheless, Constantan demonstrated to have a higher average Nusselt number in comparison to Copper and Silicon. The isothermal lines within the solid demonstrated the transition from a conduction only at the very early part of the transient to conduction-convection equilibrium heat transfer as the steady state was arrived.

References

[1] Rahman M.M., Dontaraju P., and Ponnappan R., 2002, "Confined jet impingement thermal management using liquid ammonia as the working fluid," In: Proceedings of ASME IMECE2002, November 17-22, New Orleans, Louisiana 33033.

[2] Stevens J., and Webb B.W., 1989, "Local heat transfer coefficients under an axisymmetric, single-phase liquid jet," Heat Transfer in Electronics, *111*, pp. 113–119.

[3] Garimella S.V., and Rice R.A., 1995, "Confined and submerged liquid jet impingement heat transfer," Journal of Heat Transfer, *117*, pp. 871-877.

[4] Gomi T., and Webb B.W., 1997, "Local characteristics of impingement heat transfer with oblique round free-surface jets of large prandtl number liquid," International Journal of Heat and Mass Transfer, *40* (10), pp. 2249-2259.

[5] Lee D.H., Chung Y.S., and Kim D.S., 1997, "Turbulent flow and heat transfer measurements on a curved surface with a fully developed round impinging jet," International Journal of Heat and Fluid Flow, *18*, pp. 160-169.

[6] Kornblum Y., Goldstein R.J., 1997, "Jet impingement on semicylindirical concave and convex surfaces: part II - heat transfer," International Symposium on Physics of Heat Transfer in Boiling and Condensation, pp. 597-602.

[7] Lee D.H., Chung Y.S., and Kim M.G., 1999, "Turbulent heat transfer from a convex hemispherical surface to a round impinging jet," International Journal of Heat and Mass Transfer, *42*, pp. 1147-1156.

[8] Tong A.Y., 2003, "A numerical study on the hydrodynamics and heat transfer of a circular liquid jet impinging onto a substrate," Numerical Heat Transfer, 44, pp. 1-19.

[9] Cornaro C., Fleischer A.S., and Goldstein R.J., 1999, "Flow visualization of a round jet impinging on cylindrical surfaces," Experimental Thermal and Fluid Science, *20*, pp. 66-78.

[10] Cornaro C., Fleischer A.S., Rounds M., and Goldstein R.J., 2001,"Jet impingement cooling of a convex semi-cylindrical surface," Journal of Thermal Science, *40*, pp. 890-898.

[11] Fleischer A.S., Kramer K., and Goldstein R.J., 2001, "Dynamics of the vortex structure of a jet impinging on a convex surface," Experimental Thermal and Fluid Science, *24*, pp. 169-175.

[12] Baonga J. B., Louahlia-Gualous H., and Imbert M., 2006, "Experimental study of the hydrodynamic and heat transfer of free liquid jet impinging a flat circular heated disk," Applied Thermal Engineering, *26*, pp. 1125-1138.

[13] Inada S., Miyasaka Y., and Izumi R., 1981, "A study on the laminar-flow heat transfer between a two-dimensional water jet and a flat surface with constant heat flux," In: Bulletin of the JSME—1982 JSME 24.

[14] Carper H.J., Jr., 1989, "Impingement cooling by liquid jet," In: Heat Transfer Division—1989 ASME HTD 117.

[15] Liu X., and Lienhard V., 1989, "Liquid jet impingement heat transfer on a uniform flux surface," In: Heat Transfer Phenomena in Radiation, Combustion and Fires—1989 ASME HTD 106.

[16] Wadsworth D.C., and Mudawar I., 1989, "Cooling of a multichip electronic module by means of confined two-dimensional jets of dielectric liquid," Heat Transfer in Electronics, *111*, pp. 79-87.

[17] Gau C., and Chung C.M., 1991, "Surface curvature effect on slot-air-jet impingement cooling flow and heat transfer process," Journal of Heat Transfer, *113*, pp. 858-864.

[18] Stevens J., and Webb B.W., 1992, "Measurements of the free surface flow structure under an impinging, free liquid jet," Journal of Heat Transfer, *114*, pp. 79-84.

[19] Teuscher K.L., Ramadhyani S., and Incropera F.P., 1993, "Jet impingement cooling of an array of discrete heat sources with extended surfaces," ASME HTD, *263*, pp. 1-10.

[20] Ma C.F., Zhuang Y., Lee S.C., and Gomi T., 1997, "Impingement heat transfer and recovery effect with submerged jets of large Prandtl number liquid—II. Initially laminar confined slot jets," International Journal of Heat and Mass Transfer, 40, pp. 1491-1500.

[21] Bartoli C., and Faggiani S., 1998, “Local nusselt number at a cylinder cooled by a slot jet of water,” Heat and Technology, 16 (2), pp.33-37.

[22] McDaniel C.S., and Webb B.W., 2000, “Slot jet impingement heat transfer from circular cylinders,” International Journal of Heat and Mass Transfer, 43, pp. 1975-1985.

[23] Gori F., and Bossi L., 2000, “On the cooling effect of an air jet along the surface of a cylinder,” International Communications in Heat and Mass Transfer, *27*, pp. 667-676.

[24] Kayansayan N., and Küçüka S., 2001, “Impingement cooling of a semi-cylindrical concave channel by confined slot-air-jet,” Experimental Thermal and Fluid Science, *25*, pp. 383-396.

[25] Shi Y.L., Ray M.B., and Mujumdar A.S., 2003, “Effects of prandtl number on impinging jet heat transfer under a semi-confined laminar slot jet,” International Communications Heat Mass Transfer, *30* (4), pp. 455-464.

[26] Olsson E.E.M., Ahrné L.M., and Trägårdh A.C., 2004, “Heat transfer from a slot air jet impinging on a circular cylinder,” Journal of Food Engineering, 63, pp. 393-401.

[27] Chan T. L., Leung C.W., Jambunathan K., Ashforth-Frost S., Zhou Y., and Liu M.H., 2002, “Heat transfer characteristics of a slot jet impinging on a semi-circular convex surface,” International Journal of Heat and Mass Transfer, *45*, pp. 993-1006.

[28] Chan T.L., Zhou Y., Liu M.H., and C.W. Leung, 2003, “Mean flow and turbulence measurements of the impingement wall jet on a semi-circular convex surface,” Experiments in Fluids, *34*, pp. 140–149.

[29] Gori F., and Bossi L., 2003, “Optimal slot height in the jet cooling of a circular cylinder,” Applied Thermal Engineering, *23*, pp. 859-870.

[30] Rahimi M., Owen I., and Mistry J., 2003, “Heat transfer between an under-expanded jet and a cylindrical surface,” International Journal of Heat and Mass Transfer, *46*, pp. 3135-3142.

[31] Yang Y.T., and Hwang C.H., 2004, “Numerical simulations on the hydrodynamics of a turbulent slot jet impinging on a semicylindrical convex surface, Numerical Heat Transfer, *46*, pp. 995-1008.

[32] Chen Y.C., Ma C.F., Qin, M., and Li, Y.X., 2005, “Theoretical study on impingement heat transfer with single-phase free-surface slot jets,” International Journal of Heat and Mass Transfer, 48, pp. 3381-3386.

[33] Zuckerman N., and Lior N., 2005, “Jet impingement heat transfer on a circular cylinder by radial slot jets,” In: Proceedings of ASME IMECE2005, November 5-11, Orlando, Florida USA 79565.

[34] White F. M., 2003, “Fluid mechanics 5th ed.,” McGraw-Hill, New York.

[35] Stevens J., and Webb B.W., 1992, “Measurements of the free surface flow structure under an impinging, free liquid jet,” Journal of Heat Transfer, 114, pp. 79-84.

[36] Liu X., Lienhard J.H., and Lombara J.S., 1993, “Convective heat transfer by impingement of circular liquid jets,” Journal of Heat Transfer, 13, pp. 571–582.

[37] Scholtz M.T., and Trass O., 1970, “Mass transfer in a nonuniform impinging jet,” *AIChE Journal*, pp. 82-96.

[38] Nakoryakov V.E., Pokusaev B.G., and Troyan E.N., 1978, “Impingement of an axisymmetric liquid jet on a barrier, International Journal of Heat and Mass Transfer, 9, pp. 1175-1184.

[39] Martin H., 1977, “Heat and mass transfer between impinging gas jets and solid surfaces,” Advances in Heat Transfer, 13, pp. 1-60.

[40] Whitaker S., 1972, “Forced convection heat transfer correlations for flow in pipes, past flat plates, single cylinders, single spheres, and flow in packed beds and tube bundles,” AIChE Journal, 18, pp. 361-371.

Bibliography

White F. M., 2003, “Fluid mechanics 5th ed.,” McGraw-Hill, New York.

Bejan A., 1995, “Convection heat transfer 2nd ed.,” John Wiley & Sons, New York.

Özisik M.N., 1993, “Heat conduction 2nd ed.,” John Wiley & Sons, New York.

Appendices

Appendix A: CFD Code for Axisymetric Model (FIDAP)

```
/ File opened for write Mon Oct  2 16:06:01 2006.
/ File opened for write Thu Jun 15 16:15:56 2006.
TITLE(  )
FREE SURFACE JET ON CYLINDER
FI-GEN( ELEM = 1, POIN = 1, CURV = 1, SURF = 1, NODE = 0, MEDG = 1,
MLOO = 1,
MFAC = 1, BEDG = 1, SPAV = 1, MSHE = 1, MSOL = 1, COOR = 1, TOLE =
0.0001 )
WINDOW(CHANGE= 1, MATRIX )
    1.000000    0.000000    0.000000    0.000000
    0.000000    1.000000    0.000000    0.000000
    0.000000    0.000000    1.000000    0.000000
    0.000000    0.000000    0.000000    1.000000
   -10.00000    10.00000    -7.50000     7.50000    -7.50000
7.50000
//POINTS
POINT( ADD, COOR )
    0,     0
  0.3,     0
 0.36,     0
 0.86,     0
 0.86,   0.5
 0.86,  0.56
 0.86,  0.59
0.273,  0.06
    0,  0.06
    0,  0.59
//LINES
POINT( SELE, ID )
    4,     5
    3
CURVE( ADD, ARC, CENT )
POINT( SELE, ID )
    4
    6
    2
CURVE( ADD, ARC, CENT )
POINT( SELE, ID )
    4
    7,     8
CURVE( ADD, ARC, CENT )
POINT( SELE, ID )
    8,     9
    1,     3
CURVE( ADD, LINE )
POINT( SELE, ID )
    5,     7
CURVE( ADD, LINE )
//CREATE SURFACE
POINT( SELE, ID )
   10
    7
```

Appendix A: (Continued)

```
    1
    4
SURFACE( ADD, POIN, ROWW = 2, NOAD )
//MESH EDGES
CURVE( SELE, ID )
    1,     3
MEDGE( ADD, SUCC, INTE = 62, RATI = 0, 2RAT = 0, PCEN = 0 )
CURVE( SELE, ID = 4 )
MEDGE( ADD, SUCC, INTE = 70, RATI = 0, 2RAT = 0, PCEN = 0 )
CURVE( SELE, ID = 5 )
MEDGE( ADD, SUCC, INTE = 20, RATI = 0, 2RAT = 0, PCEN = 0 )
CURVE( SELE, ID = 6 )
MEDGE( ADD, SUCC, INTE = 70, RATI = 0, 2RAT = 0, PCEN = 0 )
CURVE( SELE, ID )
    7,     8
MEDGE( ADD, SUCC, INTE = 20, RATI = 0, 2RAT = 0, PCEN = 0 )
CURVE( SELE, ID = 9 )
MEDGE( ADD, SUCC, INTE = 20, RATI = 0, 2RAT = 0, PCEN = 0 )
//MESH LOOPS
/LOOP 1
CURVE( SELE, ID )
    5
    4
    3
    9
    2
    6
MLOOP( ADD, MAP, VISI, NOSH, EDG1 = 1, EDG2 = 2, EDG3 = 1, EDG4 = 2 )
/LOOP 2
CURVE( SELE, ID )
    7
    2
    8
    1
MLOOP( ADD, MAP, VISI, NOSH, EDG1 = 1, EDG2 = 1, EDG3 = 1, EDG4 = 1 )
//MESH FACES
/FACE 1
SURFACE( SELE, ID = 1 )
MLOOP( SELE, ID = 1 )
MFACE( ADD )
/FACE 2
SURFACE( SELE, ID = 1 )
MLOOP( SELE, ID = 2 )
MFACE( ADD )
//MESH FACE ENTITIES
ELEMENT( SETD, QUAD, NODE = 4 )
MFACE( SELE, ID = 1 )
MFACE( MESH, MAP, ENTI = "fluid" )
MFACE( SELE, ID = 2 )
MFACE( MESH, MAP, ENTI = "solid" )
//MESH EDGE ENTITIES
ELEMENT( SETD, EDGE, NODE = 2 )
MEDGE( SELE, ID = 1 )
```

Appendix A: (Continued)

```
MEDGE( MESH, MAP, ENTI = "bottom" )
MEDGE( SELE, ID = 2 )
MEDGE( MESH, MAP, ENTI = "interface" )
MEDGE( SELE, ID )
    3,     4
MEDGE( MESH, MAP, ENTI = "free" )
MEDGE( SELE, ID = 5 )
MEDGE( MESH, MAP, ENTI = "f-inlet" )
MEDGE( SELE, ID )
    6,     7
MEDGE( MESH, MAP, ENTI = "syme" )
MEDGE( SELE, ID = 8 )
MEDGE( MESH, MAP, ENTI = "s-wall" )
MEDGE( SELE, ID = 9 )
MEDGE( MESH, MAP, ENTI = "f-out" )
END(  )
FIPREP(  )
//Fluid and solid properties
/B=2.5, D=0.12
/FLUID
DENSITY( ADD, SET = "water", CONS = 0.996 )
CONDUCTIVITY( ADD, SET = "water", CONS = 0.0014699 )
VISCOSITY( ADD, SET = "water", CONS = 0.00798 )
SPECIFICHEAT( ADD, SET = "water", CONS = 0.998137 )
SURFACETENSION( ADD, SET = "water", CONS = 73 )
/
/SOLID
DENSITY( ADD, SET = "silicon", CONS = 2.33 )
CONDUCTIVITY( ADD, SET = "silicon", CONS = 0.334608 )
SPECIFICHEAT( ADD, SET = "silicon", CONS = 0.17006 )
/
/ENTITIES
ENTITY( ADD, NAME = "fluid", FLUI, PROP = "water" )
ENTITY( ADD, NAME = "solid", SOLI, PROP = "silicon" )
ENTITY( ADD, NAME = "bottom", PLOT )
ENTITY( ADD, NAME = "syme", PLOT )
ENTITY( ADD, NAME = "s-wall", PLOT )
ENTITY( ADD, NAME = "f-inlet", PLOT )
ENTITY( ADD, NAME = "f-out", PLOT )
ENTITY( ADD, NAME = "interface", PLOT, ATTA = "solid", NATT = "fluid" )
ENTITY( ADD, NAME = "free", SURF, ATTA = "fluid", DEPT = 21, SPIN,
STRA,
ANG1 = 80, ANG2 = 180 )
/
/SPECIFY BOUNDARY CONDITIONS
BCNODE( ADD, COOR, NODE = 190 )
BCNODE( ADD, SURF, NODE = 190, ZERO )
BCNODE( ADD, VELO, ENTI = "bottom", ZERO )
BCNODE( ADD, UY, ENTI = "f-inlet", ZERO )
BCNODE( ADD, UX, ENTI = "f-inlet", CONS = 33.38353 )
BCNODE( ADD, UY, ENTI = "syme", ZERO )
BCNODE( ADD, VELO, ENTI = "interface", ZERO )
BCNODE( ADD, VELO, ENTI = "s-wall", ZERO )
```

Appendix A: (Continued)

```
BCNODE( ADD, TEMP, ENTI = "f-inlet", CONS = 37 )
BCFLUX( ADD, HEAT, ENTI = "bottom", CONS = 5.971 )
BCNODE( ADD, VELO, ENTI = "solid", ZERO )
/
/PROBLEM DEFINITION
PROBLEM( 2-D, LAMI, NONL, NEWT, MOME, ENER, FREE, TRAN, SING )
BODYFORCE( ADD, CONS, FX = 981, FY = 0, FZ = 0 )
PRESSURE( ADD, MIXE = 1e-11, DISC )
DATAPRINT( ADD, CONT )
EXECUTION( ADD, NEWJ )
PRINTOUT( ADD, NONE )
OPTIONS( ADD, UPWI )
UPWINDING( ADD, STRE )
/
/SOLUTION ALGORITHM
SOLUTION( ADD, N.R. = 50, KINE = 25, VELC = 0.0001, RESC = 0.0001,
SURF = 0.001 )
TIMEINTEGRATION( ADD, BACK, NSTE = 1000, TSTA = 0, DT = 1e-07, VARI,
WIND = 9,
NOFI = 10 )
POSTPROCESS( NBLO = 2 )
    1,   201,     1
  201,  1000,     1
/
/INITIAL CONDITIONS
ICNODE( ADD, UY, ENTI = "fluid", CONS = 18.38353 )
ICNODE( ADD, UX, ENTI = "fluid", CONS = 23.38353 )
ICNODE( ADD, TEMP, ENTI = "fluid", CONS = 37 )
END(  )
CREATE( FISO )
RUN( FISOLV, BACK )
/ File closed at Mon Oct  2 16:06:12 2006.
/ File opened for append Tue Oct  3 12:46:08 2006.
FIPOST(  )
TIMESTEP( STEP = -1 )
TIMESTEP( STEP = 322 )
CONVERGENCE( ALL, SOLU, LOG )
VECTOR( VELO )
WINDOW(CHANGE= 1, MATRIX )
    1.000000    0.000000    0.000000    0.000000
    0.000000    1.000000    0.000000    0.000000
    0.000000    0.000000    1.000000    0.000000
   -0.430000   -0.295000    0.000000    1.000000
    -0.37148    -0.15563    -0.36300    -0.17218     0.00000
0.00000
   45.000000   45.000000   45.000000   45.000000
REDO
WINDOW(CHANGE= 1, MATRIX )
    1.000000    0.000000    0.000000    0.000000
    0.000000    1.000000    0.000000    0.000000
    0.000000    0.000000    1.000000    0.000000
   -0.430000   -0.295000    0.000000    1.000000
```

Appendix A: (Continued)

```
WINDOW(CHANGE= 1, MATRIX )
    1.000000    0.000000    0.000000    0.000000
    0.000000    1.000000    0.000000    0.000000
    0.000000    0.000000    1.000000    0.000000
   -0.430000   -0.295000    0.000000    1.000000
    -0.42935    -0.31361    -0.30826    -0.20659     0.00000
0.00000
   45.000000   45.000000   45.000000   45.000000
REDO
WINDOW(CHANGE= 1, MATRIX )
    1.000000    0.000000    0.000000    0.000000
    0.000000    1.000000    0.000000    0.000000
    0.000000    0.000000    1.000000    0.000000
   -0.430000   -0.295000    0.000000    1.000000
     0.00000     0.00000     0.00000     0.00000     0.00000
0.00000
   45.000000   45.000000   45.000000   45.000000
REDO
WINDOW(CHANGE= 1, MATRIX )
    1.000000    0.000000    0.000000    0.000000
    0.000000    1.000000    0.000000    0.000000
    0.000000    0.000000    1.000000    0.000000
   -0.430000   -0.295000    0.000000    1.000000
    -0.43717    -0.33551    -0.29887    -0.20972     0.00000
0.00000
   45.000000   45.000000   45.000000   45.000000
REDO
WINDOW(CHANGE= 1, MATRIX )
    1.000000    0.000000    0.000000    0.000000
    0.000000    1.000000    0.000000    0.000000
    0.000000    0.000000    1.000000    0.000000
   -0.430000   -0.295000    0.000000    1.000000
     0.00000     0.00000     0.00000     0.00000     0.00000
0.00000
   45.000000   45.000000   45.000000   45.000000
REDO
WINDOW(CHANGE= 1, MATRIX )
    1.000000    0.000000    0.000000    0.000000
    0.000000    1.000000    0.000000    0.000000
    0.000000    0.000000    1.000000    0.000000
   -0.430000   -0.295000    0.000000    1.000000
    -0.29797    -0.04771    -0.36300    -0.14089     0.00000
0.00000
   45.000000   45.000000   45.000000   45.000000
REDO
WINDOW(CHANGE= 1, MATRIX )
    1.000000    0.000000    0.000000    0.000000
    0.000000    1.000000    0.000000    0.000000
    0.000000    0.000000    1.000000    0.000000
   -0.430000   -0.295000    0.000000    1.000000
```

Appendix A: (Continued)

```
WINDOW(CHANGE= 1, MATRIX )
    1.000000    0.000000    0.000000    0.000000
    0.000000    1.000000    0.000000    0.000000
    0.000000    0.000000    1.000000    0.000000
   -0.430000   -0.295000    0.000000    1.000000
     0.11340     0.41840     0.06401     0.33460     0.00000
0.00000
   45.000000   45.000000   45.000000   45.000000
REDO
WINDOW(CHANGE= 1, MATRIX )
    1.000000    0.000000    0.000000    0.000000
    0.000000    1.000000    0.000000    0.000000
    0.000000    0.000000    1.000000    0.000000
   -0.430000   -0.295000    0.000000    1.000000
     0.00000     0.00000     0.00000     0.00000     0.00000
0.00000
   45.000000   45.000000   45.000000   45.000000
REDO
WINDOW(CHANGE= 1, MATRIX )
    1.000000    0.000000    0.000000    0.000000
    0.000000    1.000000    0.000000    0.000000
    0.000000    0.000000    1.000000    0.000000
   -0.430000   -0.295000    0.000000    1.000000
     0.31204     0.52320     0.16255     0.35024     0.00000
0.00000
   45.000000   45.000000   45.000000   45.000000
REDO
WINDOW(CHANGE= 1, MATRIX )
    1.000000    0.000000    0.000000    0.000000
    0.000000    1.000000    0.000000    0.000000
    0.000000    0.000000    1.000000    0.000000
   -0.430000   -0.295000    0.000000    1.000000
     0.00000     0.00000     0.00000     0.00000     0.00000
0.00000
   45.000000   45.000000   45.000000   45.000000
REDO
CONTOUR( TEMP, AUTO )
WINDOW(CHANGE= 1, MATRIX )
    1.000000    0.000000    0.000000    0.000000
    0.000000    1.000000    0.000000    0.000000
    0.000000    0.000000    1.000000    0.000000
   -0.430000   -0.295000    0.000000    1.000000
     0.00000     0.00000     0.00000     0.00000     0.00000
0.00000
   45.000000   45.000000   45.000000   45.000000
REDO
CONTOUR( TEMP, AUTO = 200 )
MESH( NNUM )
WINDOW(CHANGE= 1, MATRIX )
    1.000000    0.000000    0.000000    0.000000
    0.000000    1.000000    0.000000    0.000000
    0.000000    0.000000    1.000000    0.000000
   -0.430000   -0.295000    0.000000    1.000000
```

Appendix A: (Continued)

```
    -0.19004     0.00547    -0.35049    -0.17687     0.00000
0.00000
   45.000000   45.000000   45.000000   45.000000
REDO
WINDOW(CHANGE= 1, MATRIX )
    1.000000    0.000000    0.000000    0.000000
    0.000000    1.000000    0.000000    0.000000
    0.000000    0.000000    1.000000    0.000000
   -0.430000   -0.295000    0.000000    1.000000
    -0.13912    -0.09816    -0.30546    -0.26914     0.00000
0.00000
   45.000000   45.000000   45.000000   45.000000
REDO
WINDOW(CHANGE= 1, MATRIX )
    1.000000    0.000000    0.000000    0.000000
    0.000000    1.000000    0.000000    0.000000
    0.000000    0.000000    1.000000    0.000000
   -0.430000   -0.295000    0.000000    1.000000
     0.00000     0.00000     0.00000     0.00000     0.00000
0.00000
   45.000000   45.000000   45.000000   45.000000
REDO
CONTOUR( TEMP, AUTO = 200 )
LINE( TEMP, ENTI = "interface" )
PRINT( TEMP, ENTI = "interface", SCRE )
PRINT( TEMP, NODE, NOD1 = 2913, NOD2 = 4053, NGEN = 19, SCRE )
PRINT( TEMP, NODE, NOD1 = 349, SCRE )
PRINT( TEMP, NODE, NOD1 = 386, SCRE )
END(  )
END(  )
/ File closed at Tue Oct  3 12:52:48 2006.
/ File opened for append Wed Oct  4 19:38:28 2006.
FIPOST(  )
TIMESTEP( STEP = -1 )
TIMESTEP( STEP = 322 )
VECTOR( VELO )
GROUP( ENTI = "fluid" )
VECTOR( VELO )
WINDOW(CHANGE= 1, MATRIX )
    1.000000    0.000000    0.000000    0.000000
    0.000000    1.000000    0.000000    0.000000
    0.000000    0.000000    1.000000    0.000000
   -0.430000   -0.295000    0.000000    1.000000
     0.29640     0.52477     0.15316     0.35650     0.00000
0.00000
   45.000000   45.000000   45.000000   45.000000
REDO
WINDOW(CHANGE= 1, MATRIX )
    1.000000    0.000000    0.000000    0.000000
    0.000000    1.000000    0.000000    0.000000
    0.000000    0.000000    1.000000    0.000000
```

Appendix A: (Continued)

```
   45.000000   45.000000   45.000000   45.000000
REDO
CONTOUR( STRE, AUTO )
WINDOW(CHANGE= 1, MATRIX )
    1.000000    0.000000    0.000000    0.000000
    0.000000    1.000000    0.000000    0.000000
    0.000000    0.000000    1.000000    0.000000
   -0.430000   -0.295000    0.000000    1.000000
     0.27138     0.47315     0.17819     0.35650     0.00000
0.00000
   45.000000   45.000000   45.000000   45.000000
REDO
WINDOW(CHANGE= 1, MATRIX )
    1.000000    0.000000    0.000000    0.000000
    0.000000    1.000000    0.000000    0.000000
    0.000000    0.000000    1.000000    0.000000
   -0.430000   -0.295000    0.000000    1.000000
     0.00000     0.00000     0.00000     0.00000     0.00000
0.00000
   45.000000   45.000000   45.000000   45.000000
REDO
CONTOUR( TEMP, AUTO )
WINDOW(CHANGE= 1, MATRIX )
    1.000000    0.000000    0.000000    0.000000
    0.000000    1.000000    0.000000    0.000000
    0.000000    0.000000    1.000000    0.000000
   -0.430000   -0.295000    0.000000    1.000000
     0.23227     0.48723     0.12344     0.34868     0.00000
0.00000
   45.000000   45.000000   45.000000   45.000000
REDO
WINDOW(CHANGE= 1, MATRIX )
    1.000000    0.000000    0.000000    0.000000
    0.000000    1.000000    0.000000    0.000000
    0.000000    0.000000    1.000000    0.000000
   -0.430000   -0.295000    0.000000    1.000000
     0.00000     0.00000     0.00000     0.00000     0.00000
0.00000
   45.000000   45.000000   45.000000   45.000000
REDO
VECTOR( VELO )
DEVICE( POST, FILE = "500" )
VECTOR( VELO )
CONTOUR( STRE, AUTO )
CONTOUR( TEMP, AUTO )
END(  )
END(  )
/ File closed at Wed Oct  4 19:48:27 2006.
```

Appendix B: CFD Code for 2-D Model

```
/ File opened for write Fri Sep 22 20:31:22 2006.
// File opened for write Wed Mar  1 02:13:54 2006.
TITLE(  )
FREE SURFACE JET IMPINGMENT
FI-GEN( ELEM = 1, POIN = 1, CURV = 1, SURF = 1, NODE = 0, MEDG = 1,
MLOO = 1,
MFAC = 1, BEDG = 1, SPAV = 1, MSHE = 1, MSOL = 1, COOR = 1, TOLE = 1e-
05 )
WINDOW(CHANGE= 1, MATRIX )
    1.000000    0.000000    0.000000    0.000000
    0.000000    1.000000    0.000000    0.000000
    0.000000    0.000000    1.000000    0.000000
    0.000000    0.000000    0.000000    1.000000
   -10.00000    10.00000    -7.50000     7.50000    -7.50000
7.50000
WINDOW( CHAN = 1, MATR )
    1,      0,      0,      0
    0,      1,      0,      0
    0,      0,      1,      0
    0,      0,      0,      1
  -10,     10,   -7.5,    7.5,   -7.5
  7.5
//POINTS
POINT( ADD, COOR, X = 0, Y = 0 )
POINT( ADD, COOR, X = -0.06, Y = 0 )
POINT( ADD, COOR, X = -0.3, Y = 0 )
POINT( ADD, COOR, X = -0.3, Y = 0.06 )
POINT( ADD, COOR, X = -0.16, Y = 0.2 )
POINT( ADD, COOR, X = -0.1, Y = 0.31 )
POINT( ADD, COOR, X = 0.03, Y = 0.47 )
POINT( ADD, COOR, X = 0.27, Y = 0.62 )
POINT( ADD, COOR, X = 0.5, Y = 0.66 )
POINT( ADD, COOR, X = 0.5, Y = 0.56 )
POINT( ADD, COOR, X = 0.5, Y = 0.5 )
POINT( ADD, COOR, X = 0.319, Y = 0.466 )
POINT( ADD, COOR, X = 0.1516, Y = 0.359 )
POINT( ADD, COOR, X = 0.0565, Y = 0.231 )
POINT( ADD, COOR, X = 0.021, Y = 0.1425 )
POINT( ADD, COOR, X = 0.0036, Y = 0.06 )
POINT( ADD, COOR, X = -0.06, Y = 0 )
POINT( ADD, COOR, X = -0.0596, Y = 0.0672 )
POINT( ADD, COOR, X = -0.041, Y = 0.16 )
POINT( ADD, COOR, X = 0.0033, Y = 0.2587 )
POINT( ADD, COOR, X = 0.112, Y = 0.399 )
POINT( ADD, COOR, X = 0.299, Y = 0.52 )
POINT( ADD, COOR, X = -0.3, Y = 0.66 )
POINT( ADD, COOR, X = 0.5, Y = 0 )
//LINES (1,2,3,4)
POINT( SELE, ID = 1 )
POINT( SELE, ID = 2 )
CURVE( ADD, LINE )
```

Appendix B: (Continued)

```
POINT( SELE, ID = 3 )
POINT( SELE, ID = 4 )
CURVE( ADD, LINE )
POINT( SELE, ID = 4 )
POINT( SELE, ID = 5 )
POINT( SELE, ID = 6 )
CURVE( ADD, ARC )
//LINES (5,6)
CURVE( SELE, ID = 4 )
POINT( SELE, ID = 5 )
CURVE( SPLI )
//LINES (7,8,9)
POINT( SELE, ID = 6 )
POINT( SELE, ID = 7 )
POINT( SELE, ID = 8 )
CURVE( ADD, ARC )
CURVE( SELE, ID = 7 )
POINT( SELE, ID = 7 )
CURVE( SPLI )
CURVE( SELE, ID = 9 )
CURVE( DELE )
POINT( SELE, ID = 7 )
POINT( SELE, ID = 8 )
POINT( SELE, ID = 9 )
CURVE( ADD, ARC )
//LINES (10,11,12,13)
POINT( SELE, ID = 9 )
POINT( SELE, ID = 10 )
CURVE( ADD, LINE )
POINT( SELE, ID = 10 )
POINT( SELE, ID = 11 )
CURVE( ADD, LINE )
POINT( SELE, ID )
   11
   12
   13
CURVE( ADD, ARC )
POINT( SELE, ID )
   13
   14
   15
CURVE( ADD, ARC )
CURVE( SELE, ID = 13 )
POINT( SELE, ID = 14 )
CURVE( SPLI )
//LINES (14,15,16,17,18)
POINT( SELE, ID )
   15
   16
    1
CURVE( ADD, ARC )
```

Appendix B: (Continued)

```
//LINES (19,20,21,22)
POINT( SELE, ID )
    2
   18
   19
CURVE( ADD, ARC )
CURVE( SELE, ID = 19 )
POINT( SELE, ID = 18 )
CURVE( SPLI )
POINT( SELE, ID )
   19
   20
   21
CURVE( ADD, ARC )
//LINES (23,24,25,26)
CURVE( SELE, ID = 22 )
POINT( SELE, ID = 20 )
CURVE( SPLI )
POINT( SELE, ID )
   21
   22
   10
CURVE( ADD, ARC )
POINT( SELE, ID )
   20
    6
CURVE( ADD, LINE )
/SURFACES
POINT( SELE, ID = 24 )
POINT( SELE, ID = 3 )
POINT( SELE, ID = 9 )
POINT( SELE, ID = 23 )
SURFACE( ADD, POIN, ROWW = 2, NOAD )
//MESH EDGES
CURVE( SELE, ID = 1 )
MEDGE( ADD, SUCC, INTE = 10, RATI = 0, 2RAT = 0, PCEN = 0 )
CURVE( SELE, ID = 2 )
MEDGE( ADD, SUCC, INTE = 30, RATI = 0, 2RAT = 0, PCEN = 0 )
CURVE( SELE, ID = 3 )
MEDGE( ADD, SUCC, INTE = 15, RATI = 0, 2RAT = 0, PCEN = 0 )
CURVE( SELE, ID = 5 )
MEDGE( ADD, SUCC, INTE = 22, RATI = 0, 2RAT = 0, PCEN = 0 )
CURVE( SELE, ID = 6 )
MEDGE( ADD, SUCC, INTE = 16, RATI = 0, 2RAT = 0, PCEN = 0 )
CURVE( SELE, ID = 8 )
MEDGE( ADD, SUCC, INTE = 22, RATI = 0, 2RAT = 0, PCEN = 0 )
CURVE( SELE, ID = 9 )
MEDGE( ADD, SUCC, INTE = 44, RATI = 0, 2RAT = 0, PCEN = 0 )
CURVE( SELE, ID = 10 )
MEDGE( ADD, SUCC, INTE = 30, RATI = 0, 2RAT = 0, PCEN = 0 )
CURVE( SELE, ID = 11 )
```

Appendix B: (Continued)

```
CURVE( SELE, ID = 14 )
MEDGE( ADD, SUCC, INTE = 22, RATI = 0, 2RAT = 0, PCEN = 0 )
CURVE( SELE, ID = 15 )
MEDGE( ADD, SUCC, INTE = 16, RATI = 0, 2RAT = 0, PCEN = 0 )
CURVE( SELE, ID = 17 )
MEDGE( ADD, SUCC, INTE = 22, RATI = 0, 2RAT = 0, PCEN = 0 )
CURVE( SELE, ID = 18 )
MEDGE( ADD, SUCC, INTE = 15, RATI = 0, 2RAT = 0, PCEN = 0 )
CURVE( SELE, ID = 20 )
MEDGE( ADD, SUCC, INTE = 15, RATI = 0, 2RAT = 0, PCEN = 0 )
CURVE( SELE, ID = 21 )
MEDGE( ADD, SUCC, INTE = 22, RATI = 0, 2RAT = 0, PCEN = 0 )
CURVE( SELE, ID = 23 )
MEDGE( ADD, SUCC, INTE = 16, RATI = 0, 2RAT = 0, PCEN = 0 )
CURVE( SELE, ID = 24 )
MEDGE( ADD, SUCC, INTE = 22, RATI = 0, 2RAT = 0, PCEN = 0 )
CURVE( SELE, ID = 25 )
MEDGE( ADD, SUCC, INTE = 44, RATI = 0, 2RAT = 0, PCEN = 0 )
CURVE( SELE, ID = 26 )
MEDGE( ADD, SUCC, INTE = 30, RATI = 0, 2RAT = 0, PCEN = 0 )
//MESH LOOPS
//LOOP 1
CURVE( SELE, ID = 2 )
CURVE( SELE, ID = 3 )
CURVE( SELE, ID = 5 )
CURVE( SELE, ID = 6 )
CURVE( SELE, ID = 26 )
CURVE( SELE, ID = 23 )
CURVE( SELE, ID = 21 )
CURVE( SELE, ID = 20 )
MLOOP( ADD, MAP, VISI, NOSH, EDG1 = 1, EDG2 = 3, EDG3 = 1, EDG4 = 3 )
//LOOP 2
CURVE( SELE, ID = 26 )
CURVE( SELE, ID = 8 )
CURVE( SELE, ID = 9 )
CURVE( SELE, ID = 10 )
CURVE( SELE, ID = 25 )
CURVE( SELE, ID = 24 )
MLOOP( ADD, MAP, VISI, NOSH, EDG1 = 1, EDG2 = 2, EDG3 = 1, EDG4 = 2 )
//LOOP 3
CURVE( SELE, ID = 1 )
CURVE( SELE, ID = 20 )
CURVE( SELE, ID = 21 )
CURVE( SELE, ID = 23 )
CURVE( SELE, ID = 24 )
CURVE( SELE, ID = 25 )
CURVE( SELE, ID = 11 )
CURVE( SELE, ID = 12 )
CURVE( SELE, ID = 14 )
CURVE( SELE, ID = 15 )
CURVE( SELE, ID = 17 )CURVE( SELE, ID = 18 )
```

Appendix B: (Continued)

```
SURFACE( SELE, ID = 1 )
MLOOP( SELE, ID = 1 )
MFACE( ADD )
SURFACE( SELE, ID = 1 )
MLOOP( SELE, ID = 2 )
MFACE( ADD )
SURFACE( SELE, ID = 1 )
MLOOP( SELE, ID = 3 )
MFACE( ADD )
// MESHING
MFACE( SELE, ID = 3 )
ELEMENT( SETD, QUAD, NODE = 4 )
MFACE( MESH, MAP, NOSM, ENTI = "silicon" )
MFACE( SELE, ID = 1 )
MFACE( SELE, ID = 2 )
ELEMENT( SETD, QUAD, NODE = 4 )
MFACE( MESH, MAP, ENTI = "water" )
//MESH MAP ELEMENT ID
ELEMENT( SETD, EDGE, NODE = 2 )
MEDGE( SELE, ID )
    1
    9
MEDGE( MESH, MAP, ENTI = "sides" )
MEDGE( SELE, ID = 2 )
MEDGE( MESH, MAP, ENTI = "axis" )
MEDGE( SELE, ID = 3 )
MEDGE( MESH, MAP, ENTI = "inlet" )
MEDGE( SELE, ID )
    4
    5
    6
    7
MEDGE( MESH, MAP, ENTI = "surface" )
MEDGE( SELE, ID = 8 )
MEDGE( MESH, MAP, ENTI = "outlet" )
MEDGE( SELE, ID )
   10
   11
   12
   13
   14
MEDGE( MESH, MAP, ENTI = "bottom" )
MEDGE( SELE, ID )
   15
   16
   17
   18
   19
MEDGE( MESH, MAP, ENTI = "interface" )
END(  )
FIPREP(  )
//Fluid and solid properties
DENSITY( ADD, SET = "water", CONS = 0.996 )
```

Appendix B: (Continued)

```
CONDUCTIVITY( ADD, SET = "water", CONS = 0.0014699 )
VISCOSITY( ADD, SET = "water", CONS = 0.00798 )
SPECIFICHEAT( ADD, SET = "water", CONS = 0.998137 )
SURFACETENSION( ADD, SET = "water", CONS = 73 )
DENSITY( ADD, SET = "silicon", CONS = 2.33 )
CONDUCTIVITY( ADD, SET = "silicon", CONS = 0.334608 )
SPECIFICHEAT( ADD, SET = "silicon", CONS = 0.17006 )
ENTITY( ADD, NAME = "water", FLUI, PROP = "water" )
ENTITY( ADD, NAME = "inlet", PLOT )
ENTITY( ADD, NAME = "outlet", PLOT )
ENTITY( ADD, NAME = "surface", SURF, DEPT = 31, SPIN, STRA, ANG1 = 45,
ANG2 = 300 )
ENTITY( ADD, NAME = "bottom", PLOT )
ENTITY( ADD, NAME = "axis", PLOT )
ENTITY( ADD, NAME = "silicon", SOLI, PROP = "silicon" )
ENTITY( ADD, NAME = "sides", PLOT )
ENTITY( ADD, NAME = "interface", PLOT, ATTA = "silicon", NATT = "water"
)
BODYFORCE( ADD, CONS, FX = 981, FY = 0, FZ = 0 )
PRESSURE( ADD, MIXE = 1e-11, DISC )
DATAPRINT( ADD, CONT )
EXECUTION( ADD, NEWJ )
PRINTOUT( ADD, NONE, BOUN )
OPTIONS( ADD, UPWI )
UPWINDING( ADD, STRE )
RELAXATION(  )
  0.5,   0.5,   0.5,     0,  0.05,   0.1
BCNODE( ADD, COOR, NODE = 42 )
BCNODE( ADD, SURF, NODE = 42, ZERO )
BCNODE( ADD, VELO, ENTI = "bottom", ZERO )
BCNODE( ADD, URC, ENTI = "inlet", ZERO )
BCNODE( ADD, UZC, ENTI = "inlet", CONS = 50.0753 )
BCNODE( ADD, URC, ENTI = "axis", ZERO )
BCNODE( ADD, VELO, ENTI = "interface", ZERO )
BCNODE( ADD, VELO, ENTI = "sides", ZERO )
BCNODE( ADD, UT, NODE = 42, ZERO )
BCNODE( ADD, TEMP, ENTI = "inlet", CONS = 37 )
BCFLUX( ADD, HEAT, ENTI = "bottom", CONS = 5.971 )
BCNODE( ADD, VELO, ENTI = "silicon", ZERO )
PROBLEM( ADD, CYLI, INCO, TRAN, LAMI, NONL, NEWT, MOME, ENER, FREE,
SING )
SOLUTION( ADD, N.R. = 50, KINE = 25, VELC = 0.0001, RESC = 0.0001,
SURF = 0.001 )
TIMEINTEGRATION( ADD, BACK, NSTE = 1000, TSTA = 0, DT = 1e-05, VARI,
WIND = 9,
NOFI = 12 )
POSTPROCESS( NBLO = 2 )
    1,   301,    10
  301,  1000,     1
CLIPPING( ADD, MINI )
1e-20, 1e-20, 1e-20, 1e-11,    37,     0
ICNODE( ADD, URC, ENTI = "water", CONS = 20 )
```

Appendix B: (Continued)

```
CREATE( FISO )
RUN( FISOLV, IDEN = "t06", BACK, AT = "", TIME = "NOW", COMP )
/ File closed at Fri Sep 22 20:31:32 2006.
```